

Optimized Receive Frontend Hardware for Magnetic Particle Imaging, Characterization Tools, and Biosensors

Quincy Huynh



Electrical Engineering and Computer Sciences
University of California, Berkeley

Technical Report No. UCB/EECS-2023-281

<http://www2.eecs.berkeley.edu/Pubs/TechRpts/2023/EECS-2023-281.html>

December 15, 2023

Copyright © 2023, by the author(s).
All rights reserved.

Permission to make digital or hard copies of all or part of this work for personal or classroom use is granted without fee provided that copies are not made or distributed for profit or commercial advantage and that copies bear this notice and the full citation on the first page. To copy otherwise, to republish, to post on servers or to redistribute to lists, requires prior specific permission.

Optimized Receive Frontend Hardware for Magnetic Particle Imaging,
Characterization Tools, and Biosensors

by

Quincy Le Huynh

A dissertation submitted in partial satisfaction of the

requirements for the degree of

Doctor of Philosophy

in

Electrical Engineering and Computer Sciences

in the

Graduate Division

of the

University of California, Berkeley

Committee in charge:

Professor Steven Conolly, Chair

Professor Ali Niknejad

Professor Michael Lustig

Doctor Greig Scott

Fall 2023

Optimized Receive Frontend Hardware for Magnetic Particle Imaging,
Characterization Tools, and Biosensors

Copyright 2023
by
Quincy Le Huynh

Abstract

Optimized Receive Frontend Hardware for Magnetic Particle Imaging,
Characterization Tools, and Biosensors

by

Quincy Le Huynh

Doctor of Philosophy in Electrical Engineering and Computer Sciences

University of California, Berkeley

Professor Steven Conolly, Chair

Magnetic Particle Imaging (MPI) is an emerging medical imaging modality that detects the strong magnetization of superparamagnetic iron oxide nanoparticle tracers. MPI has proven applications in angiography, stroke, stem cell tracking, white blood cell tracking, lung perfusion, traumatic brain injury, and gastrointestinal bleed imaging among many other highly critical medical imaging applications. However, MPI receive frontend hardware suffers from direct feedthrough interference as a result of simultaneous transmit and receive and is currently not optimized for higher resolution tracers that require a ten-fold wider bandwidth. In this dissertation I will discuss my PhD work that introduces methods to optimize for signal-to-noise ratio and suppress feedthrough interference for inductive sensors used in MPI, specifically for benchtop magnetic particle sensing systems.

The first part will discuss design methodologies for the preamplifier and receive coil. The preamplifier can be designed for another ten-fold lower noise over a five-fold wider bandwidth despite the challenge of broadband noise matching for inductive sensors. The receive coil can be designed for a ten-fold higher sensitivity per volume and lower inductance with microcoils.

The second part will discuss methods to suppress feedthrough interference with passive and active cancellation. Passive cancellation is done using gradiometric coils designed with linear programming to achieve better mechanical shimming tolerance, cancelling feedthrough by three orders of magnitude. Active cancellation using an adaptive feedforward scheme reduces feedthrough by another two orders of magnitude.

To my mom and dad, who grew up in a time of war but worked relentlessly to provide their sons with a peaceful life.

Contents

Contents	ii
List of Figures	vi
List of Tables	xiii
1 Introduction to Magnetic Particle Imaging	1
1.1 Overview	1
1.2 MPI Advantages	1
1.3 MPI Imaging Theory	3
1.3.1 MPI Detects the Rotating Magnetization of SPIOs	3
1.3.2 Magnetic Saturation Localizes SPIOs	3
1.4 New Particle Tracers Improve Imaging Performance	5
1.5 Relaxation Effects for Biosensing	6
1.6 Motivation for Benchtop Particle Characterization Tools	10
1.7 Current Challenges in MPI/AWR	11
1.8 Dissertation Outline	12
I Receive Coil and Preamplifier Optimization Improve Sensitivity and Bandwidth	13
2 Noise and Sensitivity of Magnetic Particle Imaging	14
2.1 Overview	14
2.2 Electrical Model of Solenoid Inductive Sensor	14
2.2.1 Solenoid Coil Inductor Model	14
2.2.1.1 Coil Inductance	15
2.2.1.2 Winding Resistance	15
2.2.1.3 Stray Capacitance	16
2.3 MPI Signal at the Receiver	16
2.4 Noise in MPI Systems	18
2.4.1 Body Noise	19

2.4.2	Thermal Noise	19
2.4.3	Preamplifier Two Port Noise	19
2.4.4	Noise Performance Metrics	21
2.4.5	Optimal Noise Figure	22
2.4.6	Signal-to-Noise Ratio in MPI	23
2.5	Optimal Noise Matching	24
2.5.1	Bandwidth Considerations	24
2.5.2	Preventing In-Band Coil Resonance	24
2.5.3	Transformer Matching	24
2.5.4	LC Matching Networks	26
2.5.5	Parallel LNA Devices	27
3	Optimal Preamplifier Design Methodology	30
3.1	Introduction	30
3.2	Theory	31
3.2.1	Motivation	31
3.2.2	Noise Model of MPI	31
3.3	Design Methodology	33
3.3.1	Optimal Number of Devices	33
3.3.2	Preventing In-Band Coil Resonance	35
3.3.3	Optimization Goal	36
3.3.4	Unit Amplifier Selection	37
3.3.4.1	Discrete JFETS	37
3.3.4.2	JFET OpAmps	37
3.3.4.3	BJT OpAmps	37
3.3.4.4	Selecting an Appropriate Device	38
3.4	Methods	38
3.4.1	Circuit Board Design and Construction	43
3.5	Results	46
3.5.1	Experimental Noise Data	46
3.5.2	Experimental SPIO Data	49
3.5.3	Experimental SFMIO Data	50
3.6	Conclusion	51
4	Optimal Microcoil Receiver Design	52
4.1	Introduction	52
4.2	Theory and Methods	53
4.2.1	Modelling the Coil Signal	53
4.2.2	Modelling the Coil Noise	55
4.2.3	Final Signal-to-Noise Ratio Model	56
4.2.4	SNR Model Sensitivity Analysis	56
4.2.4.1	Coil Noise Dominance	57

4.2.4.2	Preamplifier Voltage Noise Dominance	57
4.2.4.3	Preamplifier Current Noise Dominance due to Coil Inductance	57
4.3	Results	57
4.4	Conclusion	64
II Active and Passive Direct Feedthrough Suppression Improves Dynamic Range		65
5	Direct Feedthrough Interference in MPI	66
5.1	Overview	66
5.2	Cause of Direct Feedthrough Interference	66
5.2.1	Transmit to Receive Inductive Coupling	67
5.2.2	Feedthrough Contaminates Signal	67
5.3	Direct Feedthrough Inteference Suppression Methods	68
5.3.1	Gradiometric Cancellation Coils	69
6	Optimal Gradiometer Design with LP	71
6.1	Introduction	71
6.2	Theory and Methods	73
6.2.1	Problem Formulation	73
6.2.2	L_1 - Norm Optimization	75
6.2.3	Formulation as an Integer Programming Minimum Sum Set Cover Problem	75
6.2.4	Final Form of the Optimization Problem	76
6.2.5	Solution Quality of LP Solution vs. ILP Solution	76
6.3	Results and Discussion	76
6.4	Discussion and Conclusion	82
7	Active Feedthrough Interference Cancellation	83
7.1	Introduction	83
7.2	Theory	84
7.2.1	Motivation	84
7.2.2	Common Mode Rejection in Instrumentation Amplifiers	86
7.2.3	Feedthrough Cancellation with Instrumentation Amplifier	87
7.2.4	Non-idealities in Cancellation	87
7.3	Methods	89
7.3.1	Design of the Cancellation Circuit	89
7.3.2	Phase Error Detection and Correction	90
7.3.2.1	Phase Error Detection Procedure	91
7.3.2.2	Phase Error Correction Procedure	91
7.3.3	Labelling Cells with Iron Oxide Nanoparticles	92

7.3.3.1	Labelling Procedure	92
7.3.3.2	Labelling Validation	92
7.4	Results	93
7.4.1	Evaluation with Commercial Nanoparticles	94
7.4.2	Evaluation with Labelled Cells	96
7.5	Conclusion	96
7.6	Derivations	97
7.6.1	Effective Cancellation due to Non-idealities Derivation	97
7.6.1.1	Finite Common Mode Rejection	97
7.6.1.2	Quantization Error of the Cancellation Signal	97
7.6.1.3	Phase Error of the Cancellation Signal	98
7.6.1.4	Combining all non-idealities.	99
7.6.2	Phase Error Detection and Correction Derivation	99
7.6.2.1	Phase Error Detection Procedure	99
7.6.2.2	Phase Error Correction Procedure	100
8	Future Direction	101
8.1	Towards a Portable Particle Relaxometer for Non-Imaging Applications	101
8.2	Transmit/Receive Coils	101
8.3	Receive Frontend	102
8.3.1	Data Acquisition Module	102
8.4	Excitation Field Source	102
8.4.1	Power Amplifier Driving Coil	102
8.4.2	Mechanically Rotated Permanent Magnets	103
9	Conclusion	104
	Bibliography	105

List of Figures

1.1	Applications of preclinical MPI include (a) cancer imaging [2], (b) lung perfusion and ventilation imaging [3], and (c) gastrointestinal hemorrhaging imaging [4]. Images were co-registered with CT for anatomical reference. Images were reproduced with permission from [2]–[4].	2
1.2	The net magnetization of an ensemble of SPIOs align with an externally applied field. At point A, the particles are magnetized in the positive direction. At point B, the particles all have random orientations but the net magnetization is zero. At point C, the particles are magnetized in the negative direction. Transitioning from point A to C and vice versa creates a detectable voltage signal due to the change in magnetization.	3
1.3	Magnetic saturation localizes SPIO signal in space. In this example particle B is the only particle whose magnetization changes while particles A and C are “locked” in their saturated state. Utilizing a selective field gradient to localize a particle allows us to grid these signals back to a point in x-space.	4
1.4	(Right) Newer SFMIO particle tracers show higher resolution and sensitivity per mass of iron compared to (Middle) conventional SPIOs.	5
1.5	(Right) SFMIO particle tracers in an <i>in vitro</i> 2D scan taken with our group’s 7 T/m Field Free Line projection scanner experimentally show higher resolution and sensitivity compared to (Left) conventional SPIOs.	6
1.6	(a) Newer SFMIO nanoparticle tracers exhibit sharper magnetic transitions and lend to higher resolutions compared to conventional SPIOs, as shown in the point spread functions. (b) Under sinusoidal excitation, the SFMIO signal spectra is richer in harmonics, requiring a 10-fold wider receive bandwidth. Images were reproduced with permission from [5].	6
1.7	(Left) Relaxation delays the rotation of SPIOs. Because the applied field is traversed sinusoidally, we measure a delay in alternating directions (see two red curves on the left). This is not seen when the particle’s has zero relaxation times (the “adabiotic model” in blue). (Right) Relaxation broadens the point spread function due to the time delay in the particle’s rotational alignment to the applied field. Only the positive MH direction is shown for clarity, in red.	7

1.8	(Top) Brownian relaxation occurs when the particle's core and shell both align with the applied field. (Bottom) Néel relaxation occurs when only the core aligns with the applied field.	8
1.9	Brownian relaxation can be used to sense changes in viscosity, temperature, or binding effects for contrast.	8
1.10	(Top) Unbound particle only has its core and shell vs. Bound particle that is attached to a ligand (Bottom) With Brownian relaxation, bound particles are hindered and experience a longer relaxation time. This increased relaxation time can be mapped to space as a wider blur and can be used as a contrast mechanism.	9
1.11	Relaxation time is a non-linear function of applied field strength and frequency [8]. In this particular example, Brownian relaxation dominates at lower field strengths while Néel relaxation dominates at higher field strengths.	9
1.12	VSMs have excellent drive field amplitude dynamic range, but very low drive frequency capabilities. ACS has high drive frequency bandwidth, but very low field amplitude range. SQUIDs have excellent drive field range and moderately adequate drive frequency range, but is incredibly expensive due to the need for cryogenic cooling. The major disadvantages to each method make them unsuitable to use as particle characterization platforms for MPI.	10
1.13	The ideal particle relaxometer would have the ability to fully saturate the magnetization of particles, have high excitation bandwidth, and be relatively affordable as a research tool. All these attributes would make this kind of platform invaluable to MPI as a particle analysis platform.	11
1.14	The ideal particle relaxometer would have the ability to fully saturate the magnetization of particles, have high excitation bandwidth, and be relatively affordable as a research tool. All these attributes would make this kind of platform invaluable to MPI as a particle analysis platform.	11
2.1	Circuit model of receive coil includes the inductance L_{coil} , equivalent series resistance R_{coil} , and stray capacitance C_{stray}	15
2.2	Cross section of typical solenoid receiver coil used in MPI where ℓ is the length of the coil, r is the radius of the coil, w_c is the coil gauge, I is the current, and \mathbf{B} is the magnetic field generated by the current-carrying wire.	17
2.3	The Two Port Noise Model for a Resistive Sensor includes input referred voltage noise e_n and input referred current noise i_n modelled outside the amplifier, which is now considered "noiseless." This model simplified noise factor calculations for analysis and optimal noise matching.	20
2.4	The Two-Port Noise Model now includes the coil inductance and stray capacitance. This presents a challenge when noise matching because the current noise contribution increases with frequency due to the frequency dependent impedance of the coil.	23
2.5	Transformers transform the impedance of the primary to the secondary and is one method in noise matching and impedance matching.	25

2.6	LC matching networks can transform impedances for high-Q applications	26
2.7	Multi-section LC networks can be used to match impedances for specific quality factors.	27
2.8	Using N parallel amplifiers provide \sqrt{N} improvement in voltage noise and a concomitant increase in current noise. This means the effective noise power, p_n , remains constant. A summing amplifier in the second stage sums the N signals. We can use the number of parallel amps, N , as a free design parameter to optimize noise figure.	28
3.1	Circuit model of receive coil includes the inductance L_{coil} , equivalent series resistance R_{coil} , and stray capacitance C_{stray} . For the purposes of noise integration and analysis, we only consider the inductance and resistance.	32
3.2	Noise model of receive coil and preamplifier includes the inductance L_{coil} , equivalent series resistance R_{coil} , and stray capacitance C_{stray} . For the purposes of noise integration and analysis, we only consider the inductance and resistance. It now also includes the preamplifier's input referred voltage e_n and current noise i_n . . .	32
3.3	Simulations show that the custom preamplifier designed with $N=5$ LMH6629 parallel opamps achieves 10-fold improved SNR compared to the SR560 commercial preamp. Note also how important it is to optimize the correct number, N , of parallel amps for bandwidth. While $N = 8$ preamps shows reduced low frequency noise density, it also shows a rapid noise density increase above 5 MHz for $N = 8$. Our optimization procedure balances these effects by minimizing the total integrated noise.	40
3.4	Simulations show that the optimized custom preamplifier with $N = 5$ parallel unit amplifiers achieves more than a ten-fold SNR boost (20 dB noise figure improvement) across the desired receive bandwidth.	41
3.5	SPICE Simulations show that the integrated root-mean-square (RMS) noise for the optimized custom preamplifier has 4x lower noise over 5x larger bandwidth. Note that the minimum integrated RMS noise is very shallow as a function of the number of parallel unit amplifiers. Note that this doesn't match the 10-fold boost from Figure 3.4 since the integrated bandwidth for the custom preamp is 5x that of the SR560, resulting in 2.5x increased integrated noise.	42
3.6	Layout of Preamplifier PCB. In Figs. 3.6b and 3.6b, the ground planes were removed from the inverting input nodes of the amplifiers to reduce parasitic capacitance and prevent instability. In Figure 3.6d, 0.1 μ F and 0.01 μ F decoupling capacitors were placed close to the supply pins of the amplifiers. 10 μ F tantalum capacitors were placed closer to the power inputs of the board.	44
3.7	The optimal design methodology yields a preamplifier circuit that with 5 parallel amplifiers in the first stage. The second stage is an inverting summing amplifier with gain of 10. Capacitors were placed in shunt with the feedback resistors of each stage to set a low-pass filter cut-off frequency at 5 MHz.	45

3.8	Constructed Preamp PCB shows a factor of more than 4 decrease in noise. Input referred integrated noise of the optimized preamplifier was measured to be $0.9 \mu\text{V}$ whereas the SR560 preamplifier measured $5.2 \mu\text{V}$ noise.	47
3.9	Custom optimized preamplifier achieves $e_n = 300 \text{ pV}/\sqrt{\text{Hz}}$, more than a 10-fold improvement over the SR560's $e_n = 3.4 \text{ nV}/\sqrt{\text{Hz}}$ over a wider bandwidth. Data was collected with a spectrum analyzer and the inputs to the amplifier shorted.	48
3.10	20 mT 20 kHz sinusoidal excitation for 0.25 second acquisitions of serial dilution of VivoTrax™ show that the custom preamplifier board achieves roughly 200 ng iron limit of detection whereas the SR560 only achieves 1 μg . This experimentally confirms the 5-fold boost in SNR from optimal noise matching. This experiment also confirms that with just 25 seconds of averaging, our AWR design should detect roughly $200\text{ng}/\sqrt{25\text{s}/0.25\text{s}} = 20 \text{ ng}$ of SPIOs.	49
3.11	Improved bandwidth of the custom optimized preamplifier exposes more of the harmonics in SFMIO signal acquisition. The scan parameters were $f_0 = 20 \text{ kHz}$, 20 mT sinusoidal excitation for 0.25 seconds. Even with shielding, the AWR's receiver unfortunately still acts as a great pickup coil for other EMI sources such as local AM radio stations. Further shielding can be done by placing the receive frontend in a Faraday cage.	50
3.12	PSF of the SFMIO signal acquired by the custom optimized preamplifier is improved by 23 percent over the PSF of the SFMIO signal acquired by the SR560 preamplifier.	51
4.1	An example of a receive solenoid coil is pictured above. Typically receive coils for the AWR are litz wire solenoids to reduce the skin effect.	54
4.2	Decreasing radius shows a 40 dB/decade increase with sensitivity. Note that this regime is only when $r \ll \sqrt[3]{\frac{V}{\pi}}$. Outside this regime, the sensitivity of the coil per volume is weaker.	58
4.3	Decreasing radius shows an increase in coil inductance up until a certain point when the inductance is constant. This regime is when $r \ll \sqrt[3]{\frac{10V}{9\pi}}$. This is due to the long solenoid approximation where $r \ll \ell$ and the coil inductance no longer is strongly dependent on radius	59
4.4	Coil resistance increases linearly with decreasing r	60
4.5	For 100 nL volume the SNR/volume shows a 40 dB/dec slope for $r < 300 \mu\text{m}$ for the coil and preamp model versus 30 dB/dec for the coil only model. This shows that the preamplifier noise is dominant in this model.	61
4.6	For 100 nL volume the SNR/volume shows a 40 dB/dec slope for $r < 1.5 \text{ mm}$ for the coil and preamp model versus 30 dB/dec for the coil only model. This shows that the preamplifier noise is still dominant in this model.	62

4.7	For 100 nL volume the SNR/volume shows a 40 dB/dec slope for $r < 4$ mm but tapers down to 30 dB/dec for the coil and preamp model versus 30 dB/dec for the coil only model. This shows that the preamplifier noise and coil noise have relatively equal contributions in this model.	63
5.1	Excitation of particles requires simultaneous TX/RX	67
5.2	High dynamic range is needed to robustly image tumors in preclinical MPI cancer imaging, where the organs of the RES (liver and spleen) exhibit high particle uptake. Reduced feedthrough interference enables higher contrast-to-noise (CNR) imaging.	68
5.3	A gradiometer can be constructed by winding two coils in anti-series, where one coil is wound in the opposite direction of the other.	69
5.4	(Left) CAD model of the gradiometric cancellation coil shows the cantilever mechanism used to shim the relative distance between the receive coils. (Middle) Constructed gradiometric coil system as part of building the next generation Arbitrary Waveform Relaxometer. (Right) Coils are sensitive in mechanical placement, with nearly 10 dB feedthrough attenuation per 50 μ m near the ideal placement point.	70
5.5	Constructed gradiometer for the next generation AWR achieves 71 dB attenuation of direct feedthrough.	70
6.1	A possible solution for the wiring/current distribution of an optimal transmit coil design. The black filled in grids are windings and the rest is air. Blue and Red are locations of the receive coils relative to the transmit coil in the axial direction z	72
6.2	Illustration of transmit receive profiles with minimized mutual inductance. The standard transmit design (solid red) shows a sharp field profile that is by design orthogonal to the receiver coil in blue, thereby minimizing direct feedthrough interference. However winding imperfections are unavoidable and hence we must incorporate a worm gear to mechanically shim the receive coil at the magnetic center of the transmit coil. To improve prior designs, we hereby propose the dashed red transmit profile, which allows for zero mutual inductance shimming with very gradual mechanical precision. Like a vernier adjustment, this makes it far simpler to shim the coil and also keeps the zero mutual coupling more stable in response to normal building ambient vibrations.	73
6.3	TX/RX Wiring of Intial Gradiometer Coil Pair with no gap between the pair.	77
6.4	TX/RX Wiring of Intial Gradiometer Coil Pair with a gap equal to the radius of the coils between the pair.	78
6.5	TX/RX Wiring Solution given by the Linear Program. The LP provided a solution that adds a few extra winding towards the edges of the coil. Not seen are the partial windings also offered by the solution.	79

6.6	All coil configurations show that the best feedthrough rejection occurs when the coil pair is aligned with each other. The anti-Helmholtz coil pair with the gap equal to the coil radius shows better mechanical tolerance than the no-gap pair but still fails to meet the tolerance constraint. The Linear Program solution meets the 60 dB rejection constraint over 500 μm shimming distance whereas the other coil configurations require fare greater dexterity within 20 μm	80
6.7	The rounded ILP solution no longer meets the original constraints of the relaxed LP while the enhanced solution created by partial windings is only slightly worse than the best case LP solution and still meets the 60 dB over 500 μm shimming distance requirement	81
7.1	Particle Excitation creates direct feedthrough interference. A transmit coil is driven with a current waveform which generates the excitation field. The detected signal is a combination of both the nanoparticle signal and induced voltage from the transmit to receive coil coupling. This feedthrough interference is much larger than the particle signal.	85
7.2	The instrumentation amplifier can cancel signals common to both inputs. If the direct feedthrough can be captured, generated as a cancellation signal, and fed into the other input, then the difference amplifier can output the difference $V_{out}(t) = V_{sig}(t) - V_{canc}(t) = V_{spio}(t) + V_{ft}(t) - V_{ft}(t) = V_{spio}(t)$ allowing us to capture just the particle signal.	86
7.3	Using the data sheet of the AD8429 instrumentation amplifier, we simulated in LTspice the effective CMRR against frequency, CMRR against phase error at different DAC resolutions, and CMRR against DAC sampling rate. Phase error correction was also factored in. Simulation results show that CMRR falls off with frequency, but can be improved with phase correction.	87
7.4	Simulation results suggest that any resolution DAC above 8 bits provides acceptable cancellation, but there are diminishing returns after 12 bits.	88
7.5	Simulation results show that cancellation is highly dependent on DAC sample rate, unless phase correction is applied, in which case there are diminishing returns after 2 MSPS.	89
7.6	Block Diagram of Automated Phase Correction and Cancellation Procedure . . .	91
7.7	Images taken using an Olympus IX81 microscope with 10x (a), 20x (b), and 40x (c) objective lenses show cellular uptake of iron oxide nanoparticle in RAW264.7 Macrophages. Extracellular iron oxide was thoroughly washed to ensure measurement of iron content is due to the intracellular iron.	92

7.8	Constructed active cancellation board achieves ≥ 20 dB cancellation throughout the transmit bandwidth. We validate the simulation results against experimentally collected data. (a) There is good agreement of experimental data with simulated CMRR against frequency, with and without phase correction. (b) There is also excellent agreement of experimental data with simulated CMRR against artificially induced phase error. Artificially induced phase error was achieved by applying the same technique outlined in (7.5) with a set delay time. Full scale inputs were applied as feedthrough.	93
7.9	Constructed active cancellation board achieves 40 dB cancellation on the observed direct feedthrough generated by a custom-wound litz-wire transmit coil and power amplifier (AE7224, AE Techron, Elkhart, IN) from a 20 kHz 20 mT sinusoidal excitation waveform.	94
7.10	Samples of Vivotrax (40 μ L, 5.5 mg/mL stock concentration) were serially diluted up to 2048x and analyzed with the AWR. The resulting limit of detection curve shows a linear dependence of the signal to mass of iron down to 1 μ g for an acquisition time of 0.3 seconds (no averaging).	95
7.11	Point spread functions (PSFs) of diluted samples of Vivotrax (40 μ L of 5.5 mg/mL stock concentration). With active cancellation, we are able to detect 10-fold smaller masses of iron at the same signal level, showcasing an improved dynamic range. At lower amounts of iron, we start to see the thermal noise of the system, achieving thermal noise dominant LOD.	95
7.12	AWR signal of Vivotrax-labelled Raw264.7 macrophages were measured at various cell counts (Fig. 7.12). The system can detect down to 10,000 cells without saturating due to direct feedthrough interference for an acquisition time of 0.3 seconds (no averaging).	96
8.1	Power Amplifier driving transmit coil, which can be modelled as an inductive load with series resistance.	103
8.2	Power Amplifier driving transmit coil in feedback sets the current through the coil to be directly proportional to the input voltage, $I_{tx} = \frac{V_{in}}{R_{set}}$. Care must be taken in compensating the feedback network to prevent unwanted oscillations. . .	103

List of Tables

3.1	AWR Receive Chain Specifications	38
3.2	Low Noise Preamplifier Specifications	39
3.3	Specifications of the LMH6629 Unit OpAmp used in this work compared to the commercial SR560 preamplifier show a much lower voltage noise, larger bandwidth, and lower input capacitance.	39
4.1	For each of the noise dominance regimes, the slope of the SNR curve with respect to r changes. Generally the coil noise should be dominant for best SNR and noise figure.	57
7.1	Instrumentation Amplifier Specifications	90

Acknowledgments

Firstly to my advisor Steve, thank you for providing me with constant mentorship throughout my nearly 10 years at Cal. You've provided me with so many opportunities: letting me join the lab as an undergrad in my sophomore year, getting me into the 5th year MS program, and getting me into Berkeley's PhD program. You helped me become the research engineer I am, through rigorous training on how to deliver a talk, write papers/grants for a wider audience, and always think about bridging the gap between engineering and medicine. These kinds of skills are invaluable and I hope to continue to hone them beyond my PhD. I came into the lab as a pretty okay electrical engineer, but now I come out as a full systems engineer — understanding that knowing the physics, the biology, and everything involved in a system is important, not just the electronics. Thank you for being empathetic when life happens (especially during the terribly sucky time that was COVID) and for doing your darnedest to help me out of the low points of my PhD — when I needed to re-take prelims, when I needed help gaining confidence for my quals, and when I got my first paper rejected. You care about your students, and it absolutely shows.

To Zhi Wei, for being a mentor while I was an undergrad in the lab and for without your amazing work in the lab mine would be impossible. To Xinyi, for helping me settle into my first year as a graduate student. To Bo, Prashant, Yao, Irati, and Ben, for being mentors and providing your vast knowledge and guidance as post-docs when I needed it. To my undergrads Owen, Justin, Dhruv, Arvind, Leo, Nessia and many others, thanks for helping me out on experiments and for being overall cool people! To Jacob, for being an awesome manager of team undergrad particle synthesis team and for being my liaison to Magnetic Insight.

To all the mentors I had during my formative internships and consulting gigs - Frankie, Ryan, Michael, and countless others at Google, Apple, and Mosaic. Thanks for providing the technical and professional guidance I needed to be a better engineer.

To Barry and Caylin (and my favorite dachshund Eli!), for forming the troika and building camaraderie with me in my first year as a PhD student. Barry, it might be the deep timbre of your voice, but you always seemed to carry with you an aura of wisdom, making it easy to go to you for advice. Caylin, your kindness, thoughtfulness, and our coffee breaks together helped me push through the rough days. To Chinmoy, for helping me when I needed it and for being a really kind and really smart dude who can do pretty much anything.

To my friends in the "Council", to the boys in "Da Bois", to the friends I made in Cal VSA, to anyone I've shared fun times with — thank you for just spending time with me. A PhD can be lonely, so any respite from that was appreciated.

To my grandma, may you rest in peace. Con xin lỗi bà nội không thể thấy con tốt nghiệp tiến sĩ, nhưng mà cuối cùng con làm xong rồi. Con là tiến sĩ đầu tiên trong gia đình! Yên nghỉ nhé.

To my aunt Cô Tram, may you rest in peace. Thank you for cutting my hair since I was a little kid and always knowing which style I wanted. But more than that, for always calling me đẹp trai and making me feel good about the way I look after a haircut. The family misses you lots.

To my little brother Andy, I'm really proud of you. Keep working hard the way you are.

To the love of my life, Annie, who has seen me at my lowest during my PhD but has been my rock for which I can hold myself up and push through. Thank you for making me believe in myself. You make me want to be a better man, and I hope I will be able to support you the way you've supported me.

And finally to my mom and dad, who always believed I can accomplish whatever I put my mind to as long as I kept working at it. Mom, 5 and a half years did **not** really go by if I just close my eyes, but I do appreciate the moral support whenever you said that to me. However, I know escaping from Việt Nam after the war and making new lives for yourselves was extremely difficult, so I don't think the struggles during a PhD could even compare to what you two had to go through. Thank you for providing me the once-in-a-lifetime opportunity to pursue the highest possible education I could. Mom, you've always been a voice of comfort throughout my life. Dad, you've always been and still are a hard-ass but with that you've also helped give me the resources I needed to succeed in life.

Con thương mẹ ba nhiều lắm.

Chapter 1

Introduction to Magnetic Particle Imaging

1.1 Overview

Magnetic Particle Imaging (MPI) is an emerging medical imaging modality. MPI detects the strong electronic magnetization of superparamagnetic iron oxide nanoparticles (SPIOs) [1]. There are many proven clinical applications of MPI which include angiography, stroke, stem cell tracking, white blood cell tracking, lung perfusion, traumatic brain injury, and gastrointestinal bleed imaging among many other highly critical medical imaging applications. In this chapter I will go over the basics of MPI and provide the context and motivation for my works.

1.2 MPI Advantages

MPI has several advantages as an imaging modality.

- **Zero Background Signal** — There is no background signal in MPI unlike Magnetic Resonance Imaging (MRI) or X-ray Computed Tomography (CT). MPI is best compared to tracer modalities such as Positron Emission Tomography (PET), Single-photon Emission Computerized Tomography (SPECT), or Scintigraphy.
- **Biosafe Tracers** — Iron oxide nanoparticles are biosafe. An example is ferumoxytol, an FDA approved SPIO commonly used as an MRI contrast agent.
- **Linear and Positive Imaging Contrast** — MPI signal provides positive contrast and is linear with the concentration of nanoparticles.
- **No Depth Attenuation** — Unlike x-ray and ultrasound, there is no depth attenuation. The signal at 30-cm deep is the same as signal 3-mm deep into tissue.

- **Long Half Life Tracers** — SPIOs have a long shelf life and generally do not degrade over time unlike radioactive tracers used in nuclear medicine. This will enable the factory to pre-bind MPI tracers to targeting agents, like antibodies, affibodies, or aptamers. Immediately prior to a patient scan, the pre-bound tracers can be injected directly from the refrigerator. This cuts one hour out of the “hot chemistry” labeling protocol that is pervasive in nuclear medicine. Because Tc-99m and other radioactive nuclear medicine tracers decay quickly, they must be bound to antibodies or other targeting agents just a few minutes prior to the nuclear medicine scan. This is a severe limitation for emergency diagnoses with nuclear medicine and also a significant cost concern that MPI can address.

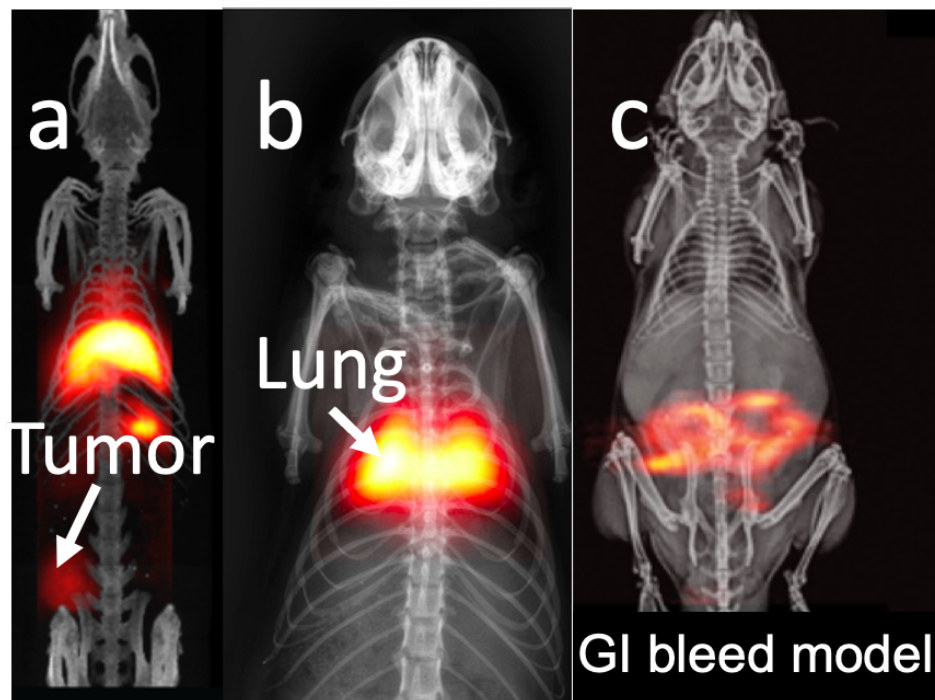


Figure 1.1: Applications of preclinical MPI include (a) cancer imaging [2], (b) lung perfusion and ventilation imaging [3], and (c) gastrointestinal hemorrhaging imaging [4]. Images were co-registered with CT for anatomical reference. Images were reproduced with permission from [2]–[4].

1.3 MPI Imaging Theory

1.3.1 MPI Detects the Rotating Magnetization of SPIOs

SPIOs align strongly with an externally applied magnetic field. As they align, the change in their bulk magnetization creates a change in flux that can be detected by an inductive pickup coil, similar to MRI. For a spatially linear gradient field, the induced signal is the point spread function (PSF). The spatial resolution of MPI depends on the magnetic transition width and strength of the gradient field. For example, a 10 mT transition width is roughly 1.4 mm FWHM spatial resolution with a 7 T/m gradient. We typically see resolutions of 1-2 mm preclinically.

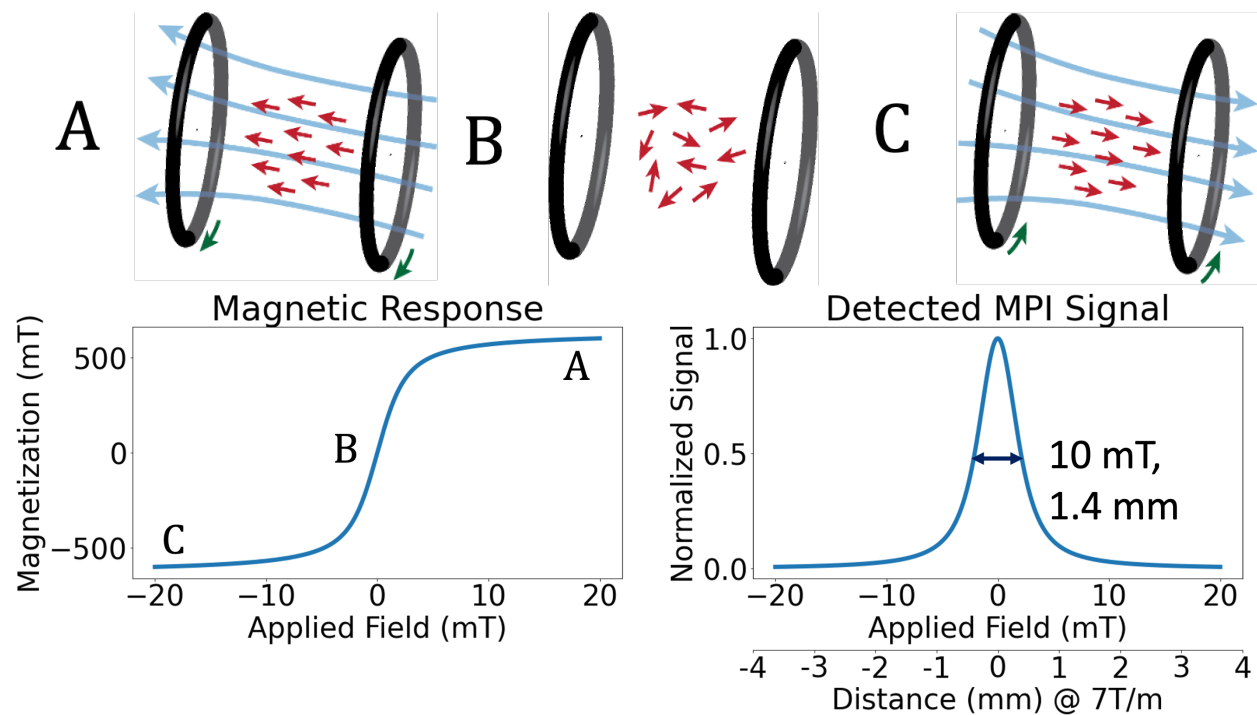


Figure 1.2: The net magnetization of an ensemble of SPIOs align with an externally applied field. At point A, the particles are magnetized in the positive direction. At point B, the particles all have random orientations but the net magnetization is zero. At point C, the particles are magnetized in the negative direction. Transitioning from point A to C and vice versa creates a detectable voltage signal due to the change in magnetization.

1.3.2 Magnetic Saturation Localizes SPIOs

To localize the MPI signal, we exploit the fact that the magnetization curve is nonlinear. By applying a spatial magnetic field gradient, particles that lie outside the field free region

(FFR) are locked in their magnetization states, while particles within the FFR are free to rotate. Particles outside the FFR are locked in a saturated state and do not rotate. This is the principle of magnetic particle imaging: saturation is key to localizing the SPIO signal. If the magnetization were not linear, localization and generating and image would not be possible.

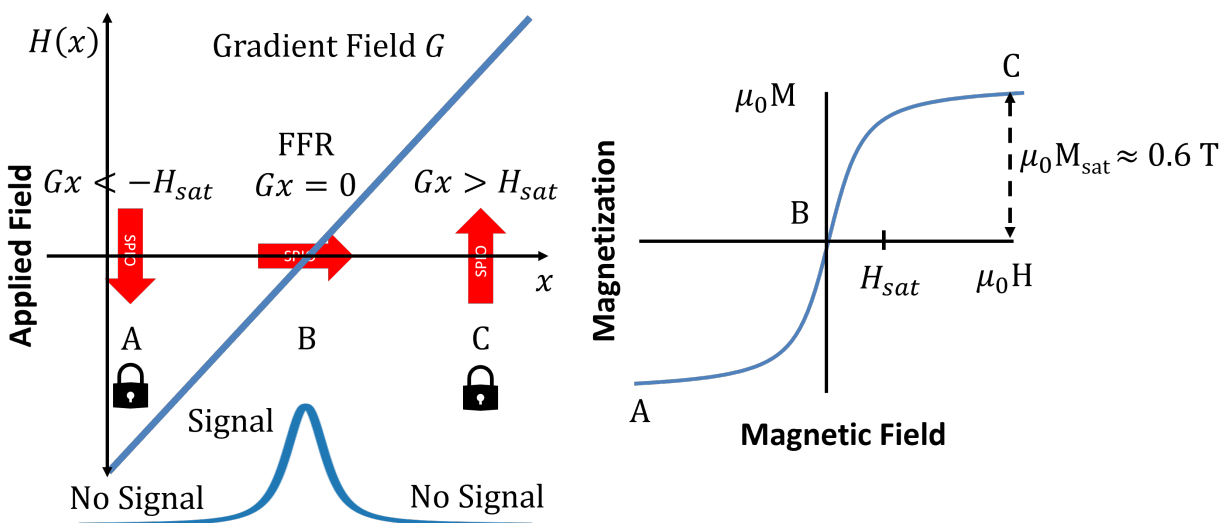


Figure 1.3: Magnetic saturation localizes SPIO signal in space. In this example particle B is the only particle whose magnetization changes while particles A and C are “locked” in their saturated state. Utilizing a selective field gradient to localize a particle allows us to grid these signals back to a point in x-space.

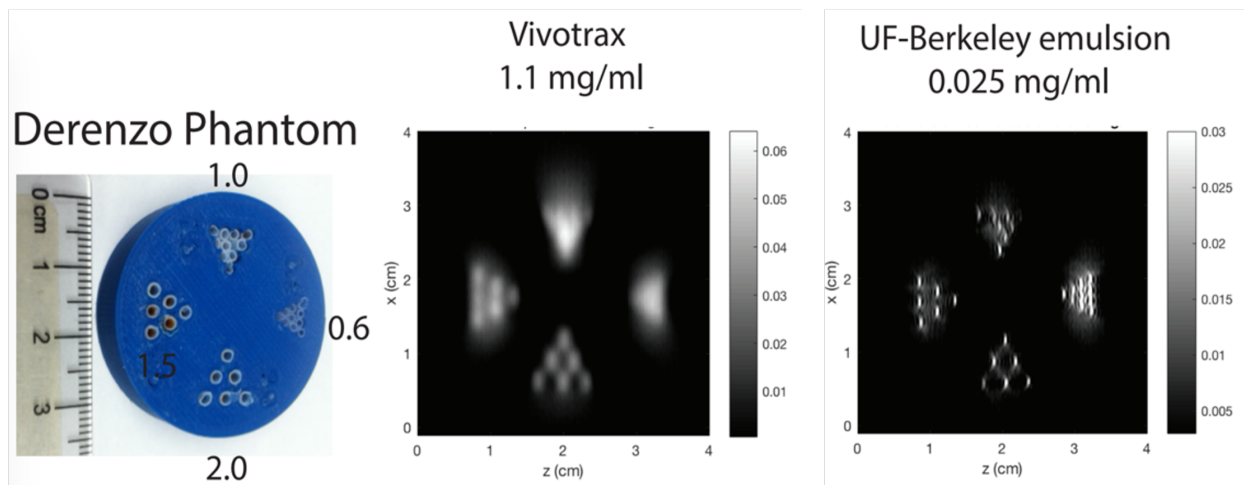


Figure 1.4: (Right) Newer SFMIO particle tracers show higher resolution and sensitivity per mass of iron compared to (Middle) conventional SPIOs.

1.4 New Particle Tracers Improve Imaging Performance

Recent breakthroughs in MPI particle tracer development has produced high resolution and high sensitivity particles called superferromagnetic iron oxide nanoparticles (SFMIOs). These SFMIOs improve preclinical MPI resolution by an order-of-magnitude [5]. A ten-fold improved resolution and signal reduces the field strength requirements of human-sized MPI scanner, where the cost of the magnet scales quadratically with field strength. To better understand how these SPIOs can be optimized for resolution and sensitivity, we require robust characterization and exploration of the optimal excitation waveforms.

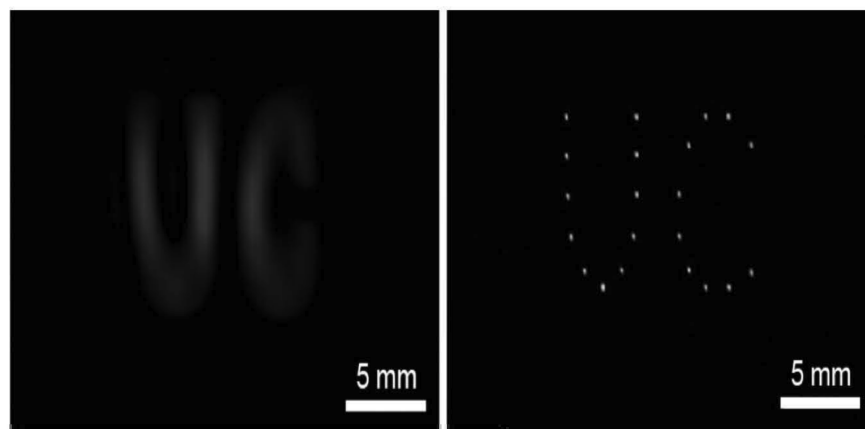


Figure 1.5: (Right) SFMIO particle tracers in an *in vitro* 2D scan taken with our group’s 7 T/m Field Free Line projection scanner experimentally show higher resolution and sensitivity compared to (Left) conventional SPIOs.

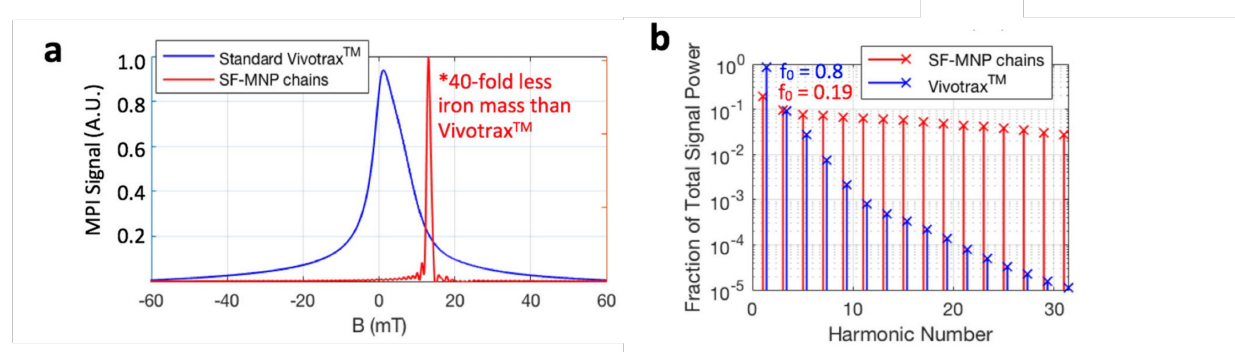


Figure 1.6: (a) Newer SFMIO nanoparticle tracers exhibit sharper magnetic transitions and lead to higher resolutions compared to conventional SPIOs, as shown in the point spread functions. (b) Under sinusoidal excitation, the SFMIO signal spectra is richer in harmonics, requiring a 10-fold wider receive bandwidth. Images were reproduced with permission from [5].

1.5 Relaxation Effects for Biosensing

Particles do not align immediately with the applied external field, exhibiting a relaxation effect that broadens the point spread function and introduces hysteresis in the M-H magnetization curve. There are two mechanisms in which particles relax to align with an applied magnetic field, Brownian and Néel [6], [7]. Brownian relaxation is when both the iron oxide core and the encapsulation shell physically rotates to align with the applied field. Néel relaxation is when the core only magnetically rather than mechanically aligns with the field.

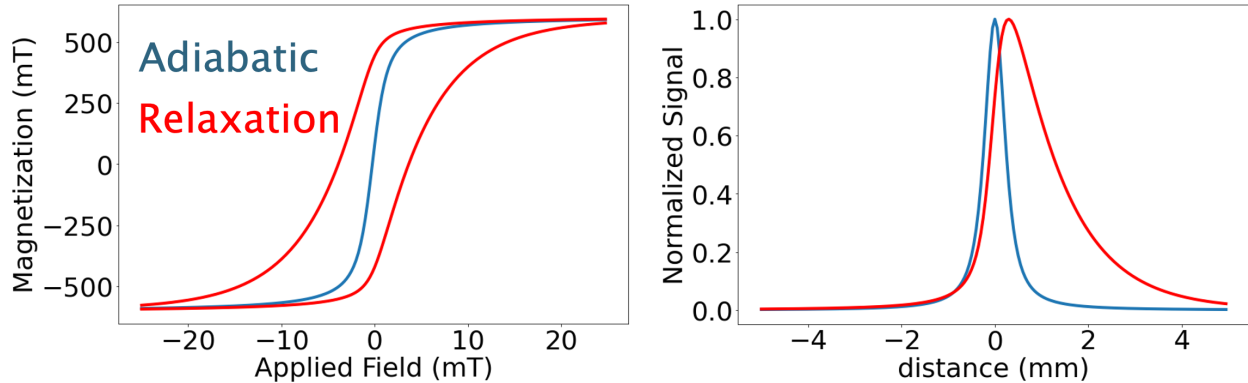


Figure 1.7: (Left) Relaxation delays the rotation of SPIOs. Because the applied field is traversed sinusoidally, we measure a delay in alternating directions (see two red curves on the left). This is not seen when the particle’s has zero relaxation times (the “adiabatic model” in blue). (Right) Relaxation broadens the point spread function due to the time delay in the particle’s rotational alignment to the applied field. Only the positive MH direction is shown for clarity, in red.

These two mechanisms operate in parallel, so the shortest mechanism dominates [8].

$$\tau_{eff} = \frac{\tau_B \tau_N}{\tau_B + \tau_N} \quad (1.1)$$

Brownian relaxation is governed by the following function:

$$\tau_B = \frac{3\eta V_h}{k_B T} \quad (1.2)$$

where η is the viscosity of the carrier liquid, V_h is the hydrodynamic volume, k_B is the Boltzmann constant, and T is temperature in Kelvin. Néel relaxation is not affected by the above parameters. This lends to a lot of interesting applications in biosensing. We can do small molecule sensing such as glucose monitoring since glucose concentration affects viscosity. We can also do thermometry. MPI has already been proven for hyperthermia [9], [10], so doing a simultaneous ablation and sensing would be very useful. With Brownian relaxation, particles can also sense their surrounding environment. The time it takes to align, or the relaxation time, can be affected binding effects. This contrast mechanism can be useful when using MPI as a biosensor. The dominant relaxation mechanism in magnetic nanoparticles can be either Brownian or Néel, and it depends on the core size, shell coating, and excitation parameters such as applied field amplitude and frequency. In order to explore the relaxation spectra and hone in on the desired regime, we must be able to excite the particles at various excitation fields.

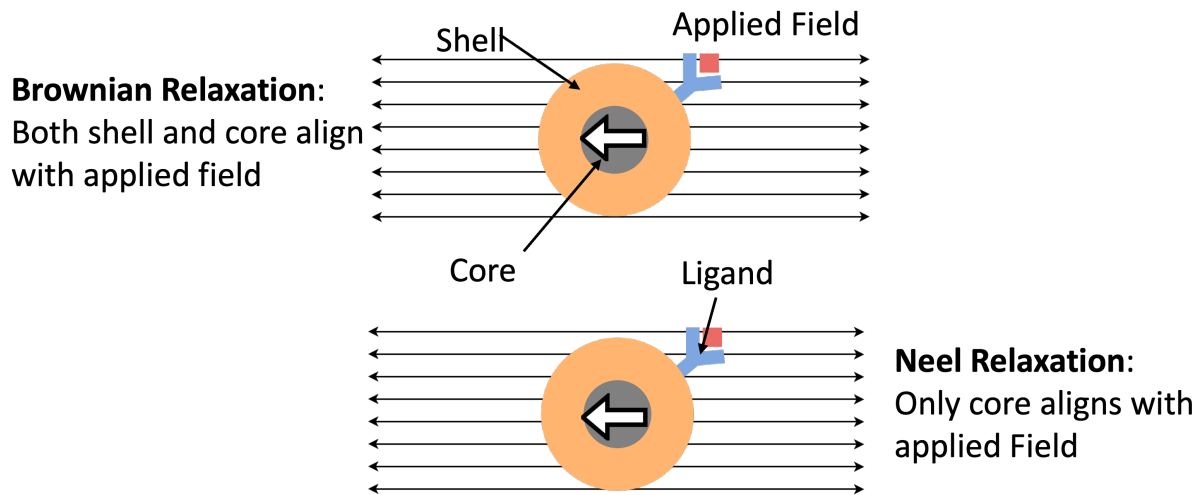


Figure 1.8: (Top) Brownian relaxation occurs when the particle's core and shell both align with the applied field. (Bottom) Néel relaxation occurs when only the core aligns with the applied field.

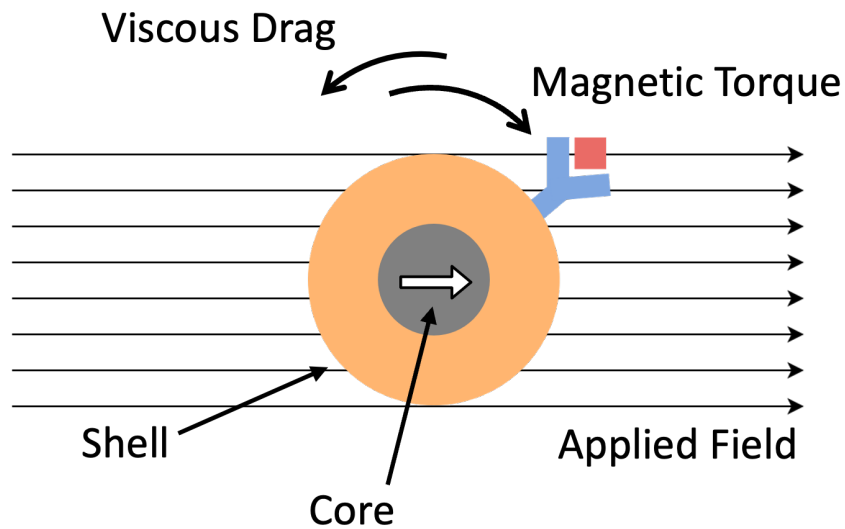


Figure 1.9: Brownian relaxation can be used to sense changes in viscosity, temperature, or binding effects for contrast.

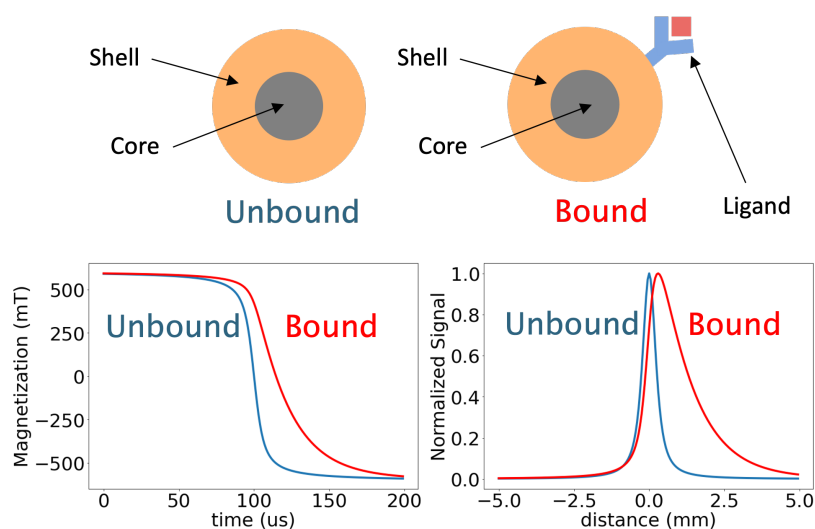


Figure 1.10: (Top) Unbound particle only has its core and shell vs. Bound particle that is attached to a ligand (Bottom) With Brownian relaxation, bound particles are hindered and experience a longer relaxation time. This increased relaxation time can be mapped to space as a wider blur and can be used as a contrast mechanism.

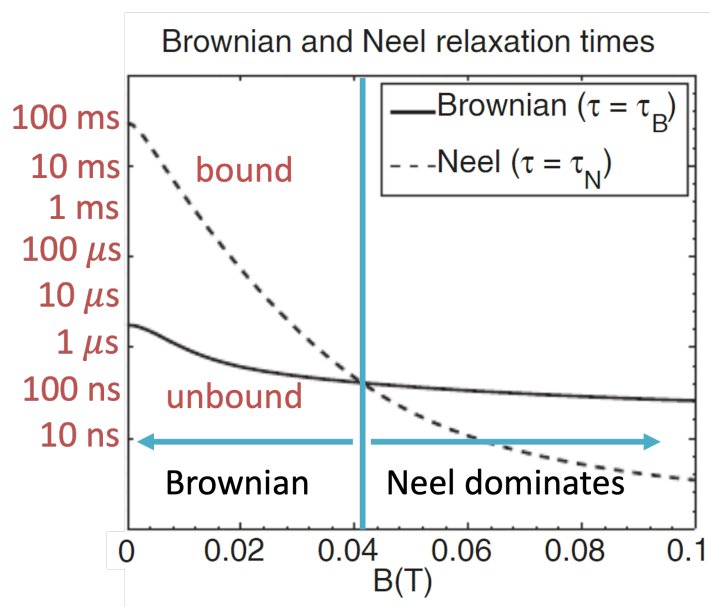


Figure 1.11: Relaxation time is a non-linear function of applied field strength and frequency [8]. In this particular example, Brownian relaxation dominates at lower field strengths while Néel relaxation dominates at higher field strengths.

1.6 Motivation for Benchtop Particle Characterization Tools

It is clear that to explore high resolution SFMIO tracers as well as the potential biosensing capabilities of Brownian-dominant SPIOs, a high throughput particle characterization tool is needed. Particle dynamics are typically explored using existing magnetometry methods such as Vibrating Sample Magnetometry (VSM), Alternating Current Susceptometry (ACS), and Superconducting Quantum Interference Devices (SQUIDs). These instruments are generally very expensive and also do not meet the field amplitude and frequency requirements needed in particle excitation.



Method	Field Range	BW	Cost	MPI?
VSM	Full saturation (up to 3T)	Low (50-100 Hz)	\$\$ (100k USD)	No
ACS	Unsaturated (0.5 mT max)	High (1-500 kHz)	\$ (10k USD)	No
SQUID	Full saturation (up to 7T)	Medium (1-10 kHz)	\$\$\$ (1mil USD)	No

Figure 1.12: VSMs have excellent drive field amplitude dynamic range, but very low drive frequency capabilities. ACS has high drive frequency bandwidth, but very low field amplitude range. SQUIDs have excellent drive field range and moderately adequate drive frequency range, but is incredibly expensive due to the need for cryogenic cooling. The major disadvantages to each method make them unsuitable to use as particle characterization platforms for MPI.

Method	Field Range	BW	Cost	MPI?
Relaxometer	Full Saturation (up to 100 mT)	High (DC-300 kHz)*	\$ (<10k USD)	Of course!

Figure 1.13: The ideal particle relaxometer would have the ability to fully saturate the magnetization of particles, have high excitation bandwidth, and be relatively affordable as a research tool. All these attributes would make this kind of platform invaluable to MPI as a particle analysis platform.

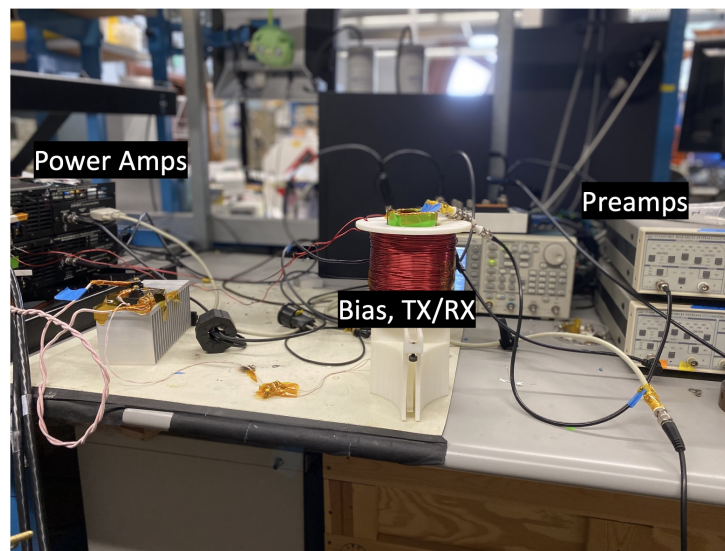


Figure 1.14: The ideal particle relaxometer would have the ability to fully saturate the magnetization of particles, have high excitation bandwidth, and be relatively affordable as a research tool. All these attributes would make this kind of platform invaluable to MPI as a particle analysis platform.

The ideal particle relaxometer would have the specifications shown in Figure 1.13: high field range, broad excitation bandwidth, and relatively low-cost. During my PhD, I worked on building the next generation Arbitrary Waveform Relaxometer (AWR) that can be used for particle characterization and pulse sequence exploration and optimization (Figure 1.14.)

1.7 Current Challenges in MPI/AWR

There are two challenges in MPI, namely improving signal-to-noise ratio and mitigating direct feedthrough interference as a result of the simultaneous transmit/receive. To improve SNR,

I aim to improve system sensitivity by an order of magnitude and improve noise figure to achieve close to coil noise dominance. To improve direct feedthrough interference rejection, I aim to employ a combination of magnetic (passive) and electronic (active) suppression techniques.

1.8 Dissertation Outline

This dissertation consists of two parts. In Part I Chapter 2 I first discuss sensitivity and noise in MPI systems. This provides context and motivation to discuss two different design methodologies to address the challenge in improving signal-to-noise ratio over a wider bandwidth. Chapter 3 discusses the first methodology of optimal broadband low noise preamplifier design to improve signal-to-noise ratio. Chapter 4 discusses the second methodology of receive coil optimization with microcoil design to improve sensitivity for benchtop particle relaxometer applications. In Part II Chapter 5 I provide background on direct feedthrough interference in MPI. This provides context and motivation to discuss methods to address the challenge in suppressing feedthrough to improve dynamic range. Chapter 6 discusses the first method for improved feedthrough rejection with shimming gradiometric coils designed with linear programming techniques. Chapter 7 discusses the second method for improved suppression with an active feedforward cancellation scheme using instrumentation amplifiers that also includes an automated phase correction algorithm.

These improvements serve to provide a framework to design an optimal receive frontend for any applications requiring inductive sensing of magnetic nanoparticles. I further provide a roadmap to design more portable particle sensing systems outside of imaging applications in Chapter 8 as a follow-up to these improvement methods.

Part I

Receive Coil and Preamplifier Optimization Improve Sensitivity and Bandwidth

Chapter 2

Noise and Sensitivity of Magnetic Particle Imaging

2.1 Overview

In this chapter, I discuss the signal and noise model in MPI and MPS systems. The signal model from the particles has been explained in Chapter 1 - here I explain the sensor model that transduces the particle signal into a detectable voltage. In Chapter 4, I discuss methods to optimize the sensor coil to maximize sensitivity per volume. I then explain and discuss noise sources that are present in a typical receive chain for MPI and ways to reduce them via noise matching. In Chapter 3, I discuss methods to optimize noise matching under bandwidth constraints.

2.2 Electrical Model of Solenoid Inductive Sensor

2.2.1 Solenoid Coil Inductor Model

The model of the MPI system consists of an inductively coupled transmit and receive coil with the subject or sample placed inside the coils. For our group's scanners, the coil bore size is 56 mm in diameter, accommodating mice. The AWR receive coil bore size is 6 mm, suitable for a tube with particle samples for characterization.

The transmit coil drives an excitation waveform, altering the magnetization of the magnetic particle tracers. This change induces a voltage picked up by the receive coil. The signal is represented as a voltage source in series with an inductor and coil winding resistance, in parallel with stray capacitance due to the capacitance between turns. The equivalent circuit model is illustrated in Figure 2.1. In the following subsections I discuss each lumped component of the model. The equations for each part of the models are well-defined or empirically determined.

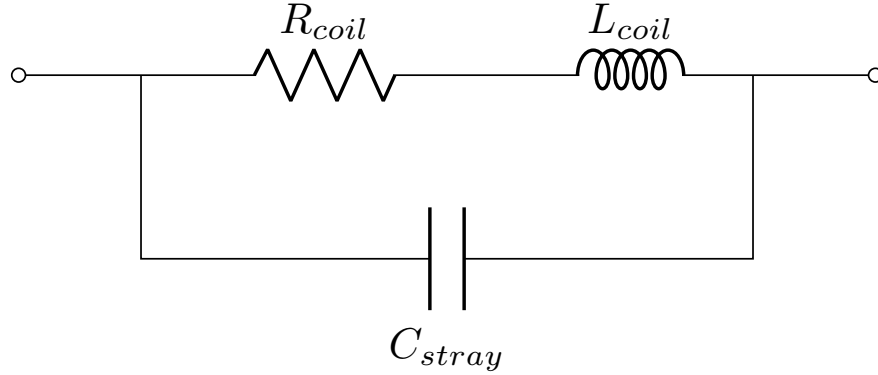


Figure 2.1: Circuit model of receive coil includes the inductance L_{coil} , equivalent series resistance R_{coil} , and stray capacitance C_{stray} .

2.2.1.1 Coil Inductance

The inductance of a single-layer solenoid is an empirically determined function of its geometry [11]:

$$L_{coil} \approx \frac{\mu_r \mu_0 N^2 A}{\ell} \quad (2.1)$$

where μ_r is the relative permeability of the core material (in MPI, the core material is animal tissue, mainly water and in the AWR, the core material are particles suspended in water or organic solvent, so $\mu_r \approx 1$ in these cases), μ_0 is the vacuum permeability of free space, N is the number of turns in the coil, A is the cross-sectional area of a turn, and ℓ is the length of the solenoid.

2.2.1.2 Winding Resistance

The coil winding DC resistance is simply the resistance of a conductor:

$$R_{coil} = \rho \frac{\ell}{A} \quad (2.2)$$

where ρ is the resistivity of the conductor (copper in this case), ℓ is the length of the overall wire if unwound, and A is the cross-section of the wire, determined by the wire gauge. However, as we are working at AC frequencies, the skin effect will decrease the effective cross-sectional area of the wire due to current crowding towards the periphery of the conductor [12]. The skin depth is defined as

$$\delta(f) = \sqrt{\frac{\rho}{\pi f \mu_r \mu_0}}. \quad (2.3)$$

Served litz wire is typically used to wind coils to reduce skin effect which would otherwise increase AC resistance [13]. AC resistance due to skin effect is determined as

$$R_{AC} = \frac{w_c^2}{w_c^2 - (w_c - \delta(f))^2} R_{DC} \quad (2.4)$$

where w_c is the width of the wire.

2.2.1.3 Stray Capacitance

The stray capacitance of a single-layer solenoid comes from the turn-to-turn capacitances, which are the equivalent capacitances between two corresponding points of any pair of adjacent turns [14]. The overall stray capacitance is then:

$$C_{\text{stray}} = \frac{C_t}{N - 1} \quad (2.5)$$

where C_t is the turn-to-turn capacitance, and N is the number of turns. The turn-to-turn capacitance is derived as:

$$C_t = \frac{\pi^2 D \epsilon_0}{\ln(p/2r + \sqrt{(p/2r)^2 - 1})} \quad (2.6)$$

where r is the wire radius, p is the winding pitch (same units as r and D), D is the turn diameter, and ϵ_0 is the permittivity of free space [14]. The stray capacitance is relatively small (on the order of femtoFarads) compared to the input capacitance (C_{in}) of the preamplifier, which is on the order of picoFarads and will dominate our resonant frequency. The resonant frequency of the receive circuit is then:

$$f_{\text{res}} = \frac{1}{2\pi \sqrt{L_{\text{coil}} \cdot (C_{\text{in}} + C_{\text{stray}})}}, \quad (2.7)$$

$$f_{\text{res}} \approx \frac{1}{2\pi \sqrt{L_{\text{coil}} \cdot C_{\text{in}}}}. \quad (2.8)$$

The winding resistance sets the Q factor of the resonance:

$$Q = \frac{\omega_{\text{res}} L_{\text{coil}}}{R_{\text{coil}}} = \frac{1}{\omega_{\text{res}} R_{\text{coil}} (C_{\text{in}} + C_{\text{stray}})}. \quad (2.9)$$

2.3 MPI Signal at the Receiver

The induced electromotive force at the detector coil can be written as a function of the field that is generated by the coil per unit current. This is the principle of reciprocity [15]:

$$\zeta = -\mathbf{B} \cdot \frac{\partial \mathbf{m}}{\partial t} \quad (2.10)$$

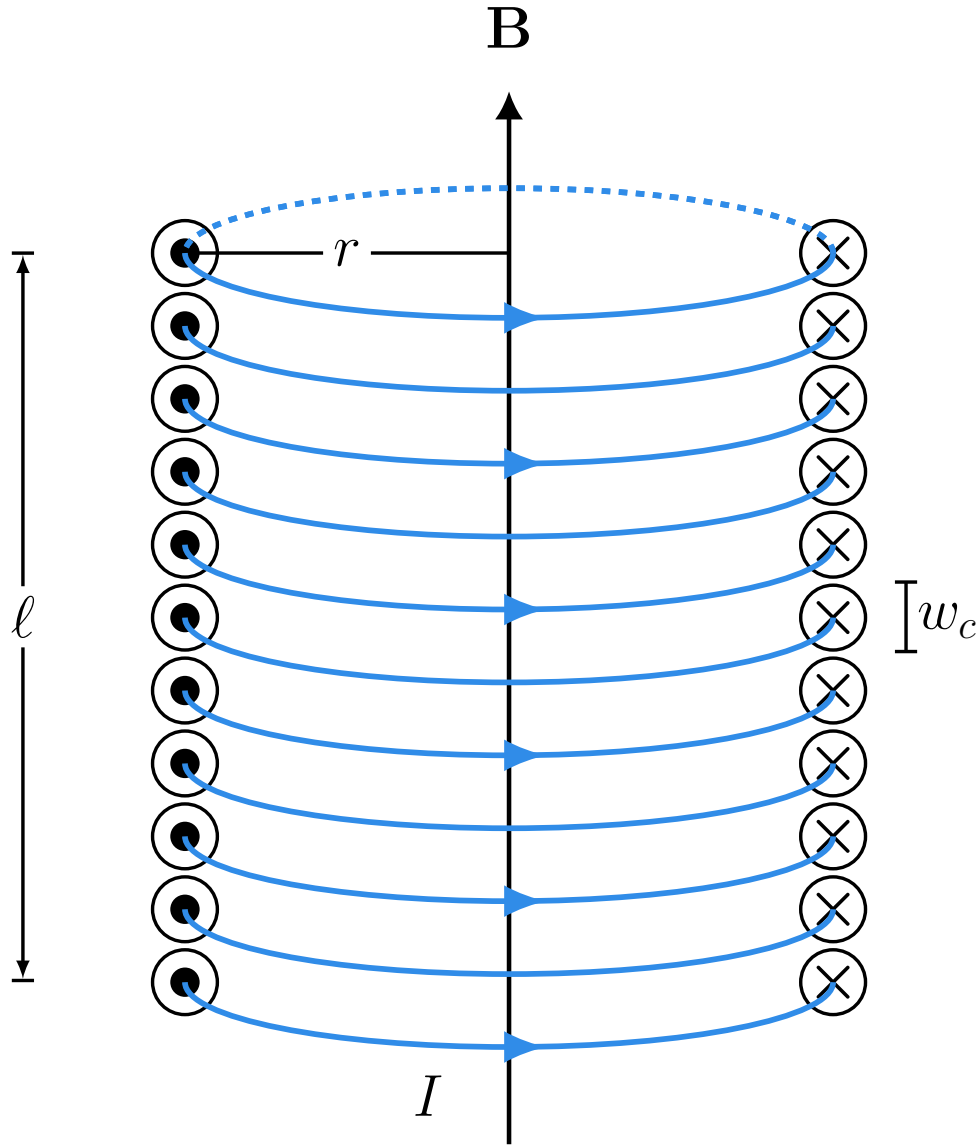


Figure 2.2: Cross section of typical solenoid receiver coil used in MPI where ℓ is the length of the coil, r is the radius of the coil, w_c is the coil gauge, I is the current, and \mathbf{B} is the magnetic field generated by the current-carrying wire.

where \mathbf{B} is the field that is generated by the coil per unit current (units of T/A) and \mathbf{m} is the magnetic moment of the magnetic nanoparticle (units of A·m²). The field generated by the coil scales linearly with the number of turns N by Amperes's Law [16]. The inductance of the coil scales quadratically with N as previously shown and the winding copper resistance scales linearly with N . The copper resistance of the coil adds noise, which we will discuss in the section on noise in MPI.

The field is generated by the current-carrying wire due to the Biot-Savart Law. We can assume the quasi-static (QS) approximation is valid because the received information from the body is typically well under 10 MHz. MRI RF engineers have determined experimentally that the quasi-static approximation is accurate even up to 64 MHz (1.5 T MRI). For high field MRI, wavelengths become proportionately shorter and hence the phase is no longer uniform over the body. For high field MRI, the QS equations can be modified to account for the propagation delays from source location to detector.

$$\mathbf{B}(\mathbf{r}) = \frac{\mu_0}{4\pi} \int_C \frac{I d\boldsymbol{\ell} \times \mathbf{r}'}{|\mathbf{r}'|^3} . \quad (2.11)$$

The axial field of a single circular loop of wire of radius r and current I is then

$$B(z) = \frac{\mu_0 I r^2}{2(r^2 + z^2)^{\frac{3}{2}}} . \quad (2.12)$$

The on-axis field of a solenoid of length ℓ , radius r , number of turns N , and current I can then be derived as

$$B(z) = \frac{\mu_0 I N}{2\ell} \left[\frac{z + \ell/2}{\sqrt{(z + \ell/2)^2 + r^2}} - \frac{z - \ell/2}{\sqrt{(z - \ell/2)^2 + r^2}} \right] \quad (2.13)$$

where the field at the center of the coil is

$$B(z) = \frac{\mu_0 I N}{\sqrt{\ell^2 + 4r^2}} . \quad (2.14)$$

2.4 Noise in MPI Systems

Noise is a stochastic process that degrades the quality of any physical measurement. Noise in MPI can be modeled with a probability density function, such as a Gaussian distribution, and is often characterized by its power spectral density, which is the power of noise at a particular frequency.

There are three sources of noise for an MPI system: thermal noise from the winding resistance of the receive coil, noise from amplifiers in the receive chain, and body noise. A long-standing goal of all MPI ultra-low noise front ends is to ensure coil noise dominance since body noise dominance is not yet achievable. Since MPI operates at generally lower frequencies (DC–1MHz), the receive coil noise and preamplifier noise dominate our signal-to-noise ratio. By designing a preamplifier with excellent noise figure, our goal is to make the noise due to the preamplifier at or sufficiently below the noise level due to the RX coil.

In this section, we will discuss the origins of each source of noise with particular emphasis on the preamplifier noise, which we will show as a two-port noise model and device noise model.

2.4.1 Body Noise

Body noise in Magnetic Resonance Imaging (MRI) is shown to be due to Brownian thermal currents in a 310 Kelvin body, which induce voltage noise in the receiver coil [17]. The noise standard deviation is proportional to the square of the radius of the body, the square root of the length of the body, and the square of the frequency.

$$\sigma_n = \frac{\omega\mu_0 N r_0^2}{2} \sqrt{\frac{kTl}{\rho T}} \quad (2.15)$$

where r_o is the radius of the body (m), l is the length of the body (m), and ω is frequency (radians/sec). [17]. This noise is similar in MPI signals. However, body noise is not yet the dominant noise source in MPI as it currently is in MRI due to the lower frequencies used since coil resistance noise dominance has not yet been achieved.

2.4.2 Thermal Noise

Since body noise dominance cannot be achieved yet, our goal is to make the dominant noise source be the thermal noise due to the RX coil's resistance. Thermal noise, often called Johnson-Nyquist noise, is electronic noise generated by the thermal agitation of the charge carriers (usually the electrons) inside an electrical conductor at equilibrium. Johnson was able to show that the noise added to a system due to a conductor was dependent on the Boltzmann's constant k , bandwidth (Δf), temperature in Kelvin (T) and the conductor's resistance (R) [18].

$$\overline{V^2} = 4kTR\Delta f \quad (2.16)$$

Therefore, as bandwidth, temperature, and resistance go up, the noise variance of this random process will go up. This presents a challenge for coil design winding (resistance) and in broadband MPI (bandwidth). In the future, the temperature issue can be resolved by using super cooling systems to push the coil temperature extremely low.

One assumption we've made is that the coil thermal noise is white and flat for simplicity. However, due to the inductance of the coil L_{coil} , capacitance of the coil C_{stray} , and input capacitance of the amplifier C_{in} , the noise is actually shaped by the transfer function. This is the power spectral density of the noise. Using Parseval's theorem, it is often helpful to integrate over frequency to get the integrated noise variance.

$$\overline{v_{n,tot}^2} = \overline{v_{n,R}^2} \int_{-\infty}^{\infty} |H(f)|^2 df \quad (2.17)$$

2.4.3 Preamplifier Two Port Noise

Regardless of the type of device used to amplify the signal, we can model the preamplifier in the receive chain as a noiseless amplifier with its input referred voltage and current noise.

These noise values are usually given as noise standard deviations (e_n is in units of $\text{nV}/\sqrt{\text{Hz}}$ and i_n is in units of $\text{pA}/\sqrt{\text{Hz}}$) on datasheets for amplifiers. Voltage noise dominates for low source impedance and current noise dominates for high source impedance. It is crucial to know both noise terms for accurately characterizing how much noise the amplifier adds to the signal. It is conventional to refer the noise generated by the amplifier from the output back to the input since the gain of the amplifier can vary. Since the voltage noise and current noise are linear combinations of the noise sources of the devices and conductors inside the amplifier, they are correlated with each other.

$$\overline{e_{n,i}^2} = |Z_{corr}|^2 \overline{i_{n,i}^2} \quad (2.18)$$

However, for simplicity, it is common to treat the input referred voltage and current noise as uncorrelated sources. The variance of uncorrelated random variables is the sum of their individual variances. Even though our source impedance is inductive we will first consider a resistive source for simplicity. Consider the input of a system shown in Figure 2.3 that contains noise from the source and the input referred noise sources from the amplifier. If

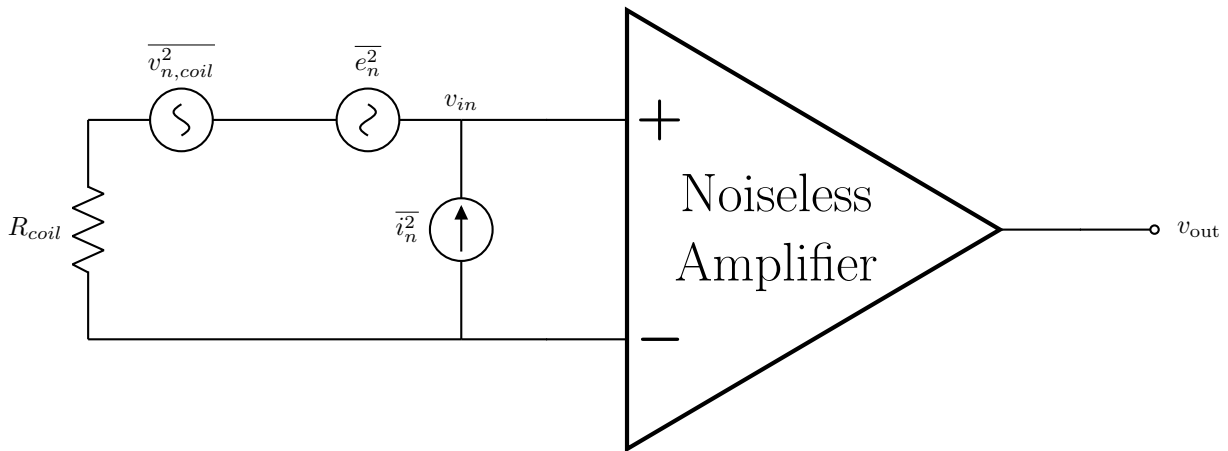


Figure 2.3: The Two Port Noise Model for a Resistive Sensor includes input referred voltage noise e_n and input referred current noise i_n modelled outside the amplifier, which is now considered "noiseless." This model simplified noise factor calculations for analysis and optimal noise matching.

we assume these three noise sources are independent, it is simple to show that the overall voltage noise variance is simply the sum of the three noise variances. That is, the total variance seen at the input of the preamplifier is:

$$\overline{v_{n,tot}^2}/\Delta f = 4kTR_{src} + \overline{e_n^2} + \overline{i_n^2}R_{src}^2 \quad (2.19)$$

It is possible to solve for optimal noise matching even if there is some correlation between the three noise sources. This is sometimes incorporated to account for (modest) correlation

between voltage and current noise in preamplifiers. For a source impedance that is not purely real, the voltage noise variance is

$$\overline{v_{n,tot}^2}/\Delta f = 4kT[\Re(Z_s)] + \overline{e_n^2} + \overline{i_n^2}|Z_s|^2 \quad (2.20)$$

2.4.4 Noise Performance Metrics

One metric that measures the noise performance of an amplifier is the Noise Figure or Noise Factor, which is defined to be the factor of how much the SNR is degraded. This can be expressed as the ratio of the SNR at the input over the SNR at the output or as the ratio of the total noise variance of the system over the noise variance due to just the source.

$$\text{NF} = \frac{SNR_{in}}{SNR_{out}} = \frac{\sigma_{n,tot}^2}{\sigma_{n,src}^2} \quad (2.21)$$

The Noise Figure for the amplifier in the previous section can then be written as:

$$\text{NF} = \frac{4kTR_{src} + \overline{e_n^2} + \overline{i_n^2}R_{src}^2}{4kTR_{src}} = 1 + \frac{\overline{e_n^2} + \overline{i_n^2}R_{src}^2}{4kTR_{src}}. \quad (2.22)$$

We note that this expression is always greater than or equal to 1, implying that the SNR at a particular frequency can never get better through amplification and that amplifying our signal with noisy amplifiers only serves to hurt the signal's integrity. However, avoiding amplification is not feasible; we need the amplifier to boost the signal to within a full scale range so that an analog-digital converter (ADC) can reasonably digitize our signal. We can only afford a small degradation in SNR, so the preamp design is crucial.

The effect of noise added in subsequent stages is reduced by the factor of the gain of the stage before it. This is demonstrated by the Friis' Noise Figure of a Cascaded System with n stages [19]. This is the reason why careful design is essential for the preamplifier, since it is the first amplifier in the receive chain. The preamplifier is also usually a low noise amplifier (LNA) because of this. Here,

$$F_{tot} = F_1 + \frac{F_2 - 1}{G_1} + \frac{F_3 - 1}{G_1 G_2} + \frac{F_4 - 1}{G_1 G_2 G_3} + \dots + \frac{F_n - 1}{\prod_{i=1}^{n-1} G_i}. \quad (2.23)$$

If we let F_1 be the noise figure of our preamplifier and consider the noise figure of the rest of the cascade F_{rest} , we can rewrite this equation as

$$F_{tot} = F_{preamp} + \frac{F_{rest} - 1}{G_{preamp}}. \quad (2.24)$$

This means that if the preamplifier has large gain, then it roughly sets the overall noise factor of the system and therefore sets how much SNR we lose.

2.4.5 Optimal Noise Figure

Since the noise figure of the preamplifier is dependent on R_{src} , if we consider the source resistance R_{src} to be a free variable, then we can find the R_{src} at which the noise figure is minimized. First, let's consider two notional values inherent to the preamplifier: its “noise power” $p_n = e_n \cdot i_n$ (units of W/Hz) and “noise impedance” $R_n = \frac{e_n}{i_n}$ (units of Ω) where e_n and i_n are the voltage and current noise density standard deviations of the preamplifier. In actuality for a given coil and our preamplifier, the free variable is actually the ratio of e_n and i_n , which we called R_n . This derivation is to show that the lowest noise figure achievable for a system is when the source resistance R_{src} is matched to the noise resistance R_n . We maintain the product p_n but can freely change the ratio of e_n/i_n .

From our noise figure equation, we manipulate e_n and i_n into p_n and R_n .

$$\begin{aligned} \text{NF} &= 1 + \frac{\overline{\frac{e_n^2}{i_n^2}} + R_{src}^2}{4kTR_{src}} \cdot \overline{i_n^2} \\ \text{NF} &= 1 + \frac{\overline{\frac{e_n^2}{i_n^2}} + R_{src}^2}{4kTR_{src} \cdot \frac{e_n}{i_n}} \cdot e_n i_n \\ \text{NF} &= 1 + \frac{R_n^2 + R_{src}^2}{4kTR_{src}R_n} \cdot p_n \end{aligned} \tag{2.25}$$

From there, we take a partial derivative with respect to R_n and set the derivative to 0 and solve for R_n .

$$\begin{aligned} \frac{\partial \text{NF}}{\partial R_{src}} &= \frac{p_n}{4kT} \frac{2R_{src}(R_{src}R_n) - R_n(R_n^2 + R_{src}^2)}{R_{src}^2 R_n^2} \\ \frac{\partial \text{NF}}{\partial R_{src}} &= \frac{p_n}{4kT} \frac{2R_{src}^2 R_n - R_n^3 - R_{src}^2 R_n}{R_{src}^2 R_n^2} \\ \frac{\partial \text{NF}}{\partial R_{src}} &= \frac{p_n}{4kT} \frac{R_{src} R_n - R_n^3}{R_{src}^2 R_n^2} \\ \frac{\partial \text{NF}}{\partial R_{src}} &= \frac{p_n}{4kT} \left(\frac{1}{R_n} - \frac{R_n}{R_{src}^2} \right) = 0 \implies R_{src} = R_n \end{aligned} \tag{2.26}$$

We see that the minimal noise figure occurs when $R_{src} = R_n$. We should be careful to note that this is the case for a particular pair of p_n and R_n or e_n and i_n . Plugging this critical point $R_{src} = R_n$ back into the noise figure formula,

$$\begin{aligned} \text{NF}_{min} &= 1 + \frac{R_n^2 + R_n^2}{4kTR_n R_n} \cdot p_n \\ \text{NF}_{min} &= 1 + \frac{2R_n^2}{4kTR_n^2} \cdot p_n \\ \text{NF}_{min} &= 1 + \frac{p_n}{2kT} \end{aligned} \tag{2.27}$$

As a sanity check, we confirm that kT and p_n both have dimensions of W/Hz which keeps

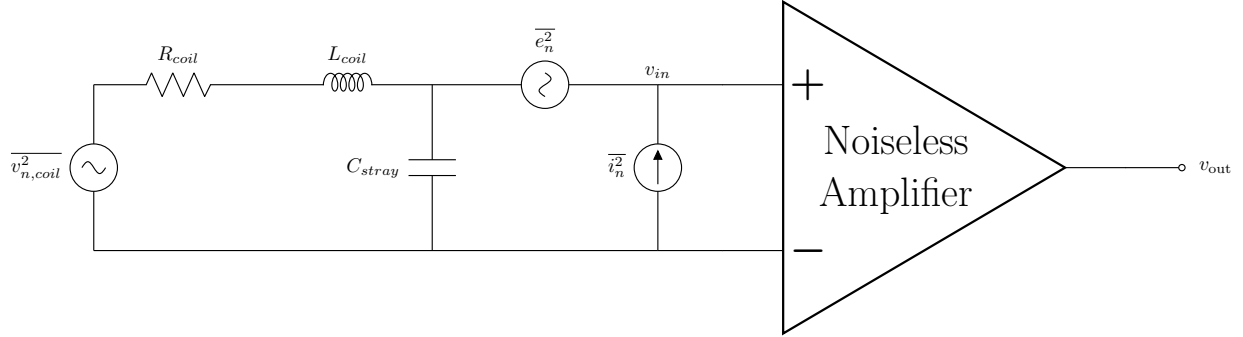


Figure 2.4: The Two-Port Noise Model now includes the coil inductance and stray capacitance. This presents a challenge when noise matching because the current noise contribution increases with frequency due to the frequency dependent impedance of the coil.

NF_{min} unit-less. It is important to note that the minimal noise figure depends, not on R_n , the quotient of the voltage and current noise densities, but on p_n , the product of the voltage and current noise densities e_n and i_n . This show that low-noise preamp designs must employ *both* low current noise and low voltage noise preamps over the bandwidth of your signal.

This is especially true when we finally put into consideration the fact that our sensor has a reactive source impedance. We simply include the inductive impedance of the receive coil into the noise model along with the stray capacitance, as shown in Figure 2.4. If we consider $R_{src} \rightarrow Z_{src} = R_{src} + jX_{src} = R_{src} + j\omega L_{src}$ (ignoring the very small stray capacitance), then the noise figure is then

$$NF(\omega) = 1 + \frac{\overline{e_n^2} + \overline{i_n^2} |Z_{src}(\omega)|^2}{4kTR_{src}} \quad (2.28)$$

$$NF(\omega) = 1 + \frac{\overline{e_n^2} + \overline{i_n^2} (R_{src}^2 + \omega^2 L_{src}^2)}{4kTR_{src}}$$

At higher frequencies, the voltage induced in the coil from the preamp's current noise increases. This frequency dependence presents a challenge when trying to noise match, since we want to noise match for all frequencies.

2.4.6 Signal-to-Noise Ratio in MPI

As shown in the previous section, the signal in the receive coil is dependent on the detection limit of the receive coil. The signal-to-noise ratio of the signal at the sensor is the fundamental sensitivity of an inductive coil.

$$SNR = \frac{-\mathbf{B} \cdot \frac{d\mathbf{m}}{dt}}{\sqrt{4kTR_{src}BW}} \propto \frac{B}{\sqrt{4kTR_{src}BW}} \quad (2.29)$$

The integrated SNR with the noise from the preamplifier included is

$$SNR \approx \frac{B}{\sqrt{(4kTR_{src}BW + e_n^2BW + \int_{BW/2}^{BW/2} \overline{i_n^2} |Z_s(\omega)|^2 d\omega)}} \quad (2.30)$$

2.5 Optimal Noise Matching

In this section, we discuss the concept of optimal noise matching for resistive sensors. The primary objective is to match the source impedance to the effective noise resistance of the preamplifier. We explore three techniques of noise matching: using transformers, LC-matching networks, and averaging with parallel amplifiers. We discuss the advantages and disadvantages to each.

2.5.1 Bandwidth Considerations

The bandwidth of the matching network is a critical parameter, especially in the context of MPI's operational range (DC to 1 MHz). Designing for a low-quality factor in the matching network is required for optimal matching across the entire bandwidth.

2.5.2 Preventing In-Band Coil Resonance

When noise matching for inductive sensors, we have to be wary about the change in the coil's resonance frequency. The coil's self resonance frequency is:

$$f_r = \frac{1}{2\pi\sqrt{L_{coil}C_{coil}}} \quad (2.31)$$

However, components in the matching network may contribute to the effective inductance and capacitance, driving down the resonant frequency.

2.5.3 Transformer Matching

Transformer operation is described by Faraday's Law of Induction, where the voltage induced on the primary and secondary coils is dependent on the change in flux through the core and the number of turns. Since it is a passive device, the product of $I \cdot V$ is constant on both

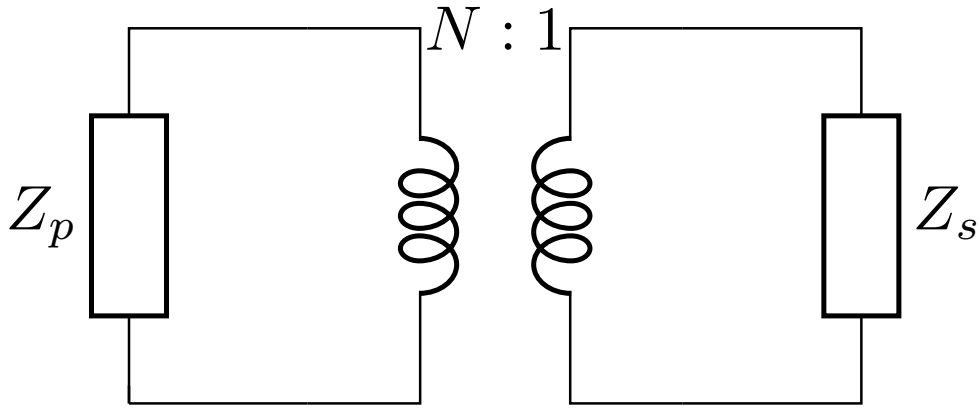


Figure 2.5: Transformers transform the impedance of the primary to the secondary and is one method in noise matching and impedance matching.

sides.

$$\begin{aligned}
 V_p &= -N_p \frac{d\phi}{dt} \\
 V_s &= -N_s \frac{d\phi}{dt} \\
 V_p &= \frac{N_p}{N_s} V_s = N V_s \\
 I_p &= \frac{N_s}{N_p} I_s = \frac{1}{N} I_s
 \end{aligned} \tag{2.32}$$

The effective impedance seen from the primary side is

$$Z_p = \frac{V_p}{I_p} = N^2 \frac{V_s}{I_s} = N^2 Z_s \tag{2.33}$$

We can therefore choose the turn ratio N to be the matching ratio $M = \frac{Z_p}{Z_s}$:

$$N = \sqrt{\frac{Z_p}{Z_s}} . \tag{2.34}$$

The effect on the noise figure using transformers with a $N : 1$ turn ratio is as follows:

$$\text{NF}(\omega) = 1 + \frac{\overline{e_n^2}}{N^2} + \frac{N^2 \overline{i_n^2} |Z_s(\omega)|^2}{4kTR_{src}} . \tag{2.35}$$

The advantage of using a transformer to perform noise matching is that it has a large matching bandwidth and excellent amplitude and phase balance over the matching bandwidth.

The disadvantage when matching with a transformer is that it is actually a lossy component due to copper and core loss; in addition, there are primary and secondary inductances and parasitic capacitances that limit the usage of transformers for MPI. Large inductances and capacitances due to the transformer windings increases the effective inductance and capacitance seen by the preamplifier stage, increasing Z_{src} and lowering the resonant frequency.

2.5.4 LC Matching Networks

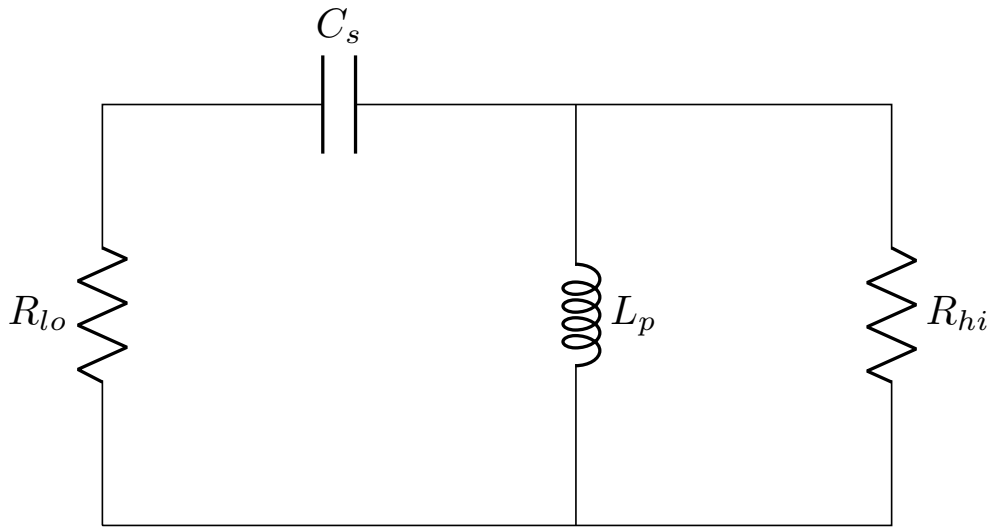


Figure 2.6: LC matching networks can transform impedances for high-Q applications

LC Ladder Matching Networks are great for high-Q matching. For a simple LC match, such as the one shown in Figure 2.6, the quality of the match is dependent on the ratio of the higher impedance and lower impedance.

$$Q = \sqrt{\frac{R_{hi}}{R_{lo}} - 1} \quad (2.36)$$

For an AC coupled LC match at a center frequency f_c , the design equations are as follows:

$$\begin{aligned} X_p &= \frac{R_{hi}}{Q} \\ L_p &= \frac{X_p}{2\pi f_c} \\ X_s &= \frac{X_p}{1 + Q^2} \\ C_s &= \frac{1}{X_s \cdot 2\pi f_c} \end{aligned} \quad (2.37)$$

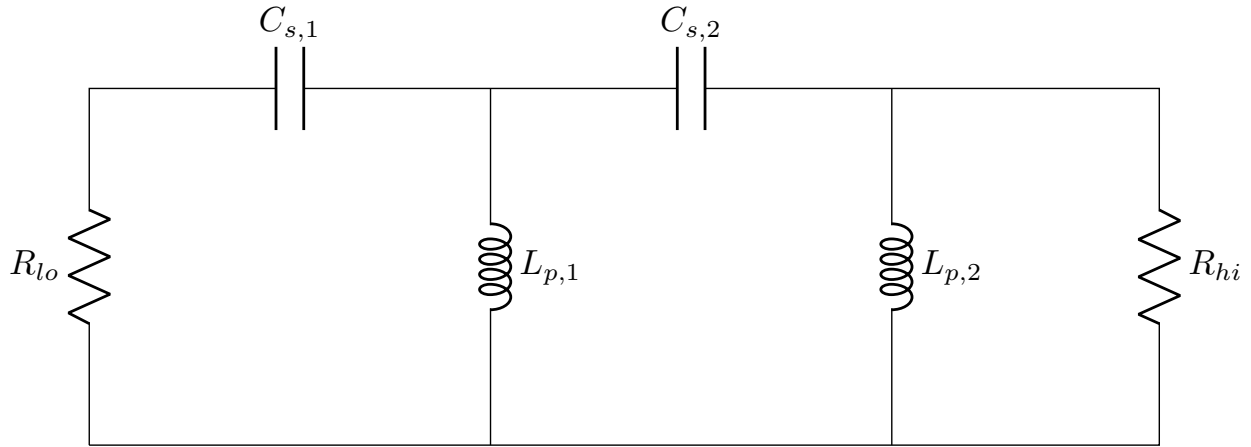


Figure 2.7: Multi-section LC networks can be used to match impedances for specific quality factors.

More complex LC matching networks can be employed to design for a specific Q . While Tee and Pi networks allow for more narrowband matches with higher Q , multi-section LC matching allows for wideband, lower Q matching by choosing intermediate impedances. An example of a multi-section LC matching network is shown in Figure 2.7. The minimum Q for a two section network is when the optimal intermediate impedance is

$$R_{int,opt} = \sqrt{R_{hi} \cdot R_{lo}} \quad (2.38)$$

This can be generalized to a N -section LC network where the optimal intermediate impedance between sections is a geometric progression from the previous stage impedance. This leads to the optimal lowest Q of

$$Q_{min} = \sqrt{\left(\frac{R_{hi}}{R_{lo}}\right)^{1/N} - 1}. \quad (2.39)$$

The advantages of using the multi-section LC network is being able to achieve a larger matched bandwidth. There is also a minimum number of sections N such that the insertion loss due to lossy components is also minimized. The disadvantage of using a multi-section LC network at a low center frequency is the use of unreasonably sized component values such as large inductances.

2.5.5 Parallel LNA Devices

In the case where parallel LNAs are used as the preamplifier, we can take the sum of the outputs of each LNA as shown in Figure 2.8, which is similar to taking an average. We can increase SNR by summing the signal since the variance of the sum of N noisy observations

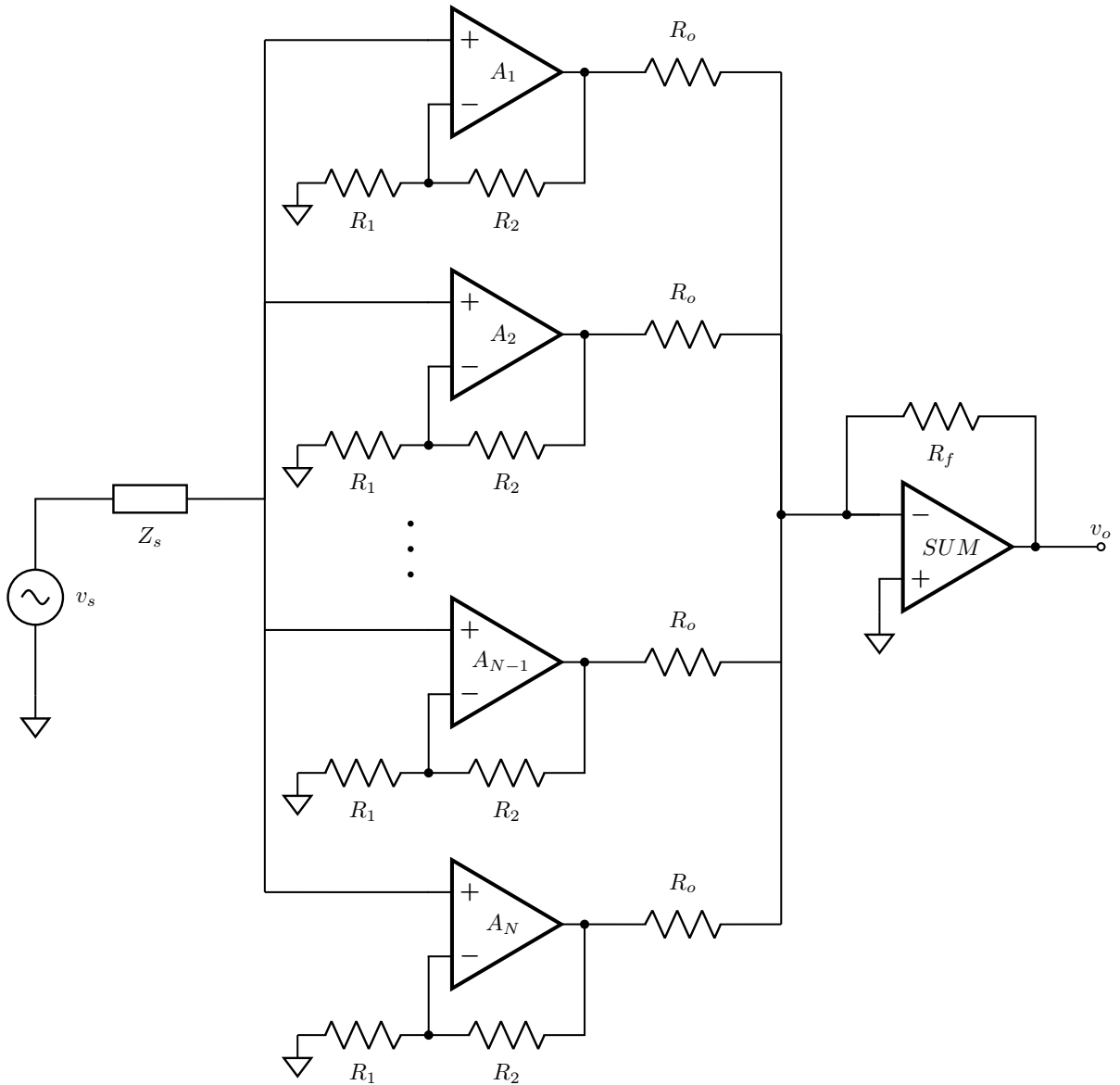


Figure 2.8: Using N parallel amplifiers provide \sqrt{N} improvement in voltage noise and a concomitant increase in current noise. This means the effective noise power, p_n , remains constant. A summing amplifier in the second stage sums the N signals. We can use the number of parallel amps, N , as a free design parameter to optimize noise figure.

increases by factor of N . The variance of a white gaussian noise process X can be described

in the following equation:

$$\text{Var}\left(N \sum_i^N X_i\right) = N \text{Var}(X) . \quad (2.40)$$

The standard deviation of the noise is therefore larger by \sqrt{N} . However, summing the signal N times yields a factor of N larger signal strength. The net increase in SNR is therefore $\frac{N}{\sqrt{N}} = \sqrt{N}$. However, as we add more devices in parallel we also effectively add the current noise sources of the N parallel devices, which means that our effective current noise variance is multiplied by N . The Noise Figure for this case can be described in the following equation:

$$\text{NF}(\omega) = 1 + \frac{\frac{\overline{e_n^2}}{N} + N \overline{i_n^2} |Z_s(\omega)|^2}{4kTR_{src}} . \quad (2.41)$$

The advantage of averaging using parallel amplifiers is very low voltage noise and a wide bandwidth match. However, this comes at the cost of very high power consumption, higher current noise and bandwidth of the amplifier. The bandwidth of the amplifier decreases by a factor of N since the system is now loaded by N input capacitances. This should not be a concern if the input capacitance is sufficiently small and the bandwidth of the LNA is sufficiently large. This is discussed in more detail in Chapter 3.

Chapter 3

Optimal Broadband Low Noise Preamplifier Design Methodology for Inductive Sensors Improves SNR

3.1 Introduction

Magnetic particle imaging (MPI) is a tracer imaging modality that detects superparamagnetic iron oxide nanoparticles (SPIOs). Since its inception [1], MPI has enjoyed a rich developmental history - from its k-space and x-space formulation [20], [21]; to scanner design [22]–[25]; to optimized coil and instrumentation [26]–[29]. Promising clinical applications for MPI include brain imaging [24], [25], [30]; stem cell tracking [31], [32]; immune cell tracking [4]; lung imaging [3]; gastrointestinal bleed imaging [2]; and cancer imaging [33]. Magnetic Particle Spectroscopy (MPS) and Magnetic Particle Relaxometry (MRX) are used to characterize the nanoparticles used in MPI, as well as other biosensing applications [34]. Signal-to-Noise Ratio (SNR), Resolution, and Contrast are the biggest challenges in any imaging method. SNR is primarily effected by front end noise matching [27] and direct feedthrough challenges [29], [34]–[38]. New MPI Tracers are crucial to optimizing MPI resolution and SNR per picogram of iron. MPI has already demonstrated robust systemic tracking of SPIO-labeled cells with a detection limit of 100s of cells in a preclinical scanner [31], [32], [39]–[41]. The detection sensitivity of MPI is soon approaching that of nuclear medicine techniques, making it useful for future clinical applications in cancer imaging, stroke diagnosis and staging, and cell therapy tracking [27]. However, too low of a receive gain prevents robust detection of small amounts of SPIO-labelled cells at full scale range. Literature has shown that labelling efficiency of SPIO-labelled cells vary widely from 1-100 pg Fe/cell [32], [42]–[47].

MPI has exceptional sensitivity due to the strong intense electronic magnetization of SPIOs. However, there is plenty of room for improvement of signal-to-noise ratio over the receive bandwidth. Previous works have improved sensitivity using matching networks [22], matching transformers [27], and parallel amplifiers to reduce noise [27]. This work aims to

solidify the design methodology needed to create an optimal low noise preamplifier tailored for MPI receive coils.

3.2 Theory

3.2.1 Motivation

Preclinical MPI is highly sensitive and quantitative with resolution comparable to other deep tissue imaging modalities such as MRI and nuclear medicine, but needs a lot of room for improvement in resolution for MPI to scale to a human-size scanner [30], [48]. Novel tracers called Superferromagnetic Iron Oxide (SFMIO) particles show an order-of-magnitude improvement in resolution - these high-resolution tracers show a rich harmonic spectrum showing strong peaks at harmonic numbers where Vivotrax's signal would already be at the noise floor [5]. Therefore, an order of magnitude improvement in resolution with SFMIOs necessitates a corresponding increase in the receive (RX) signal bandwidth. This work will focus mainly on optimizing the RX frontend of MPI/MPS/MRX systems to realize this 10-fold increase in bandwidth while also improving the limit of detection with broadband noise matching.

Previous work in MPI broadband noise matching has shown exquisite noise performance down to 100s of $\text{pV}/\sqrt{\text{Hz}}$ voltage noise density [25], [27]. However, increasing the noise matching ratio N leads to decreasing effective noise bandwidth due to two major factors. The first is that the resonant frequency of the RX coil decreases as the effective inductance increases (winding more turns or using a transformer increases inductance and capacitance) and effective capacitance increases (adding more amplifiers in parallel increases the contribution of input capacitance). Reported resonance frequencies of 200 kHz to 300 kHz, which lends to adequate bandwidth to reconstruct 10-15 harmonics for Vivotrax and other commercial particles but would squander the several remaining harmonics of SFMIOs. The current noise contribution of the preamplifier due to the increasing impedance of the inductive coil over frequency can also become more dominant than the coil noise voltage and noise voltage of the preamplifier. These two factors limit effective noise match bandwidth. This work will showcase a design procedure for minimizing RX noise over a desired bandwidth and improving limit-of-detection.

3.2.2 Noise Model of MPI

The most common way to detect the MPI signal is with an inductive pick-up receive coil. We can model this coil as an inductor with series resistance (see Figure 3.1). The noise associated with this lumped circuit model is

$$\overline{v_{n,\text{coil}}^2} = \int_0^{BW} 4kTR_{\text{coil}}df = 4kTR_{\text{coil}}BW \quad (3.1)$$

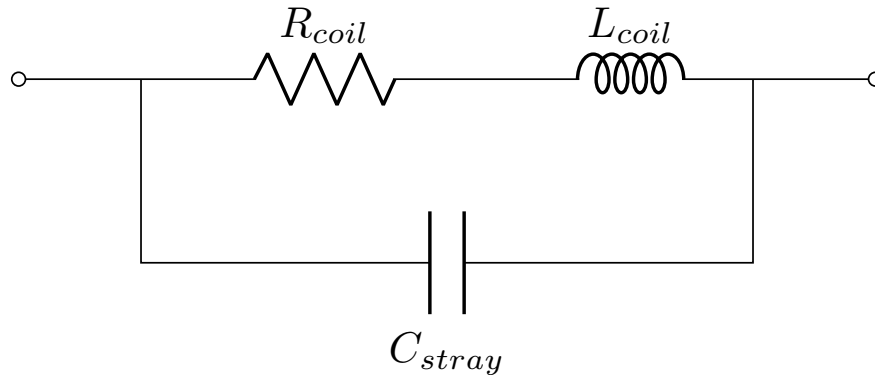


Figure 3.1: Circuit model of receive coil includes the inductance L_{coil} , equivalent series resistance R_{coil} , and stray capacitance C_{stray} . For the purposes of noise integration and analysis, we only consider the inductance and resistance.

where R_{coil} is the equivalent series resistance of the coil and BW is the receive bandwidth. The noise due to the coil is purely from thermal noise associated with its resistance.

Since the raw MPI signal is small (μVs to mVs), it must be amplified to the full scale range of the Analog-to-Digital Converter (ADC) to digitize it without significant loss of SNR due to quantization error. This is typically done with a low noise amplifier. Amplifiers have their own internal noise and thus contribute to the overall system noise and degrade SNR. Often, the first amplifier is called the preamplifier. How much the preamplifier adds noise relative to the sensor's is called its Noise Factor. Designers should strive to minimize Noise Factor and achieve sensor noise dominance.

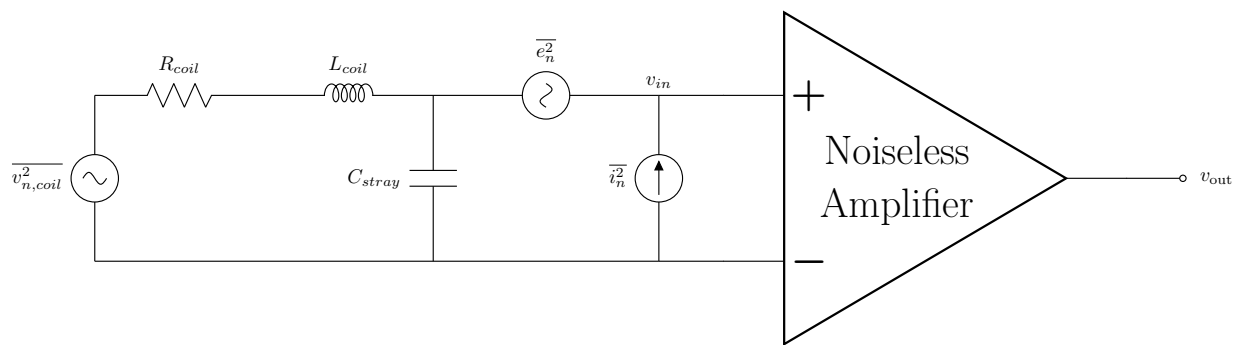


Figure 3.2: Noise model of receive coil and preamplifier includes the inductance L_{coil} , equivalent series resistance R_{coil} , and stray capacitance C_{stray} . For the purposes of noise integration and analysis, we only consider the inductance and resistance. It now also includes the preamplifier's input referred voltage e_n and current noise i_n .

Preamplifier noise can be modeled as input referred independent voltage and current noise

sources, ($\overline{e_n^2}$ and $\overline{i_n^2}$), respectively (see Figure 3.2). While there is a very small correlation amongst an amplifier's noise sources [49], we will treat them as uncorrelated for simplicity.

Factoring in the noise due to the preamplifier, the total input noise is

$$\overline{v_{n,in}^2} = \int_{-BW/2}^{BW/2} 4kTR_{\text{coil}} + \overline{e_n^2} + \overline{i_n^2} \left((2\pi f L_{\text{coil}})^2 + R_{\text{coil}}^2 \right) df \quad (3.2)$$

$$\overline{v_{n,in}^2} = 4kTR_{\text{coil}} \cdot BW + \overline{e_n^2} \cdot BW + \overline{i_n^2} R_{\text{coil}}^2 \cdot BW + \frac{4\pi^2}{3} \overline{i_n^2} L_{\text{coil}}^2 \cdot BW^3 \quad (3.3)$$

$$\overline{v_{n,in}^2} = 4kTR_{\text{coil}} \cdot BW + \overline{e_n^2} \cdot BW + \overline{i_n^2} \left(R_{\text{coil}}^2 + \frac{4\pi^2}{3} \overline{i_n^2} L_{\text{coil}}^2 \cdot BW^2 \right) \cdot BW \quad (3.4)$$

With the amplifier included in the model, the noise is now dependent on the inductance L_{coil} due to the current noise of the preamplifier. This presents a challenge in designing a low noise preamplifier over a wide receive bandwidth. As the bandwidth increases, the noise due to the current noise inductance contribution increases cubically.

3.3 Design Methodology

Noise matching methods improve noise factor and SNR by decreasing a dominant noise source in exchange for increasing a non-dominant noise source until their contributions are equal. The typical optimal noise matching occurs when the equivalent noise resistance $R_n = \frac{e_n}{i_n}$ is equal to the sensor resistance R_s . This can be achieved by paralleling N amplifiers until the desired R_n is achieved, as shown in Chapter 2. This is typically done for spot noise (noise at a particular frequency) when matching within a narrow bandwidth or a purely resistive source. However, this work uses an integrated noise approach to account for the frequency dependence of the noise due to the current noise inductance contribution.

3.3.1 Optimal Number of Devices

The optimal noise matching for an inductive sensor can be derived in a similar manner. For given bandwidth BW , coil inductance L_{coil} , and coil resistance R_{coil} , we can derive the required R_n by finding the ratio of e_n and i_n such that the contributions of these noise sources are equal. When noise matching with a factor of N , the integrated noise variance becomes a function of N :

$$\overline{v_{n,in}^2(N)} = 4kTR_{\text{coil}} \cdot BW + \frac{\overline{e_n^2}}{N} \cdot BW + N \cdot \overline{i_n^2} \left(R_{\text{coil}}^2 + \frac{4\pi^2}{3} L_{\text{coil}}^2 \cdot BW^2 \right) \cdot BW \quad (3.5)$$

This equation assumes that R_{coil} does not change much with frequency due to the skin effect. We use 100/44 served litz wire for the receive coil, which can operate well into a few MHz without much change in AC resistance.

Minimizing this value is a relatively straightforward optimization problem. If we want to minimize total integrated noise, we solve for when the first derivative is 0:

$$\frac{\overline{\partial v_{n,in}^2(N)}}{\partial N} = -\frac{\overline{e_n^2}BW}{N^2} + \overline{i_n^2} \left(R_{\text{coil}}^2 + \frac{4\pi^2}{3} L_{\text{coil}}^2 \cdot BW^2 \right) \cdot BW \quad (3.6)$$

$$\frac{\overline{\partial v_{n,in}^2(N)}}{\partial N} = 0 \implies -\frac{\overline{e_n^2}BW}{N_{\text{opt}}^2} + \overline{i_n^2} \left(R_{\text{coil}}^2 + \frac{4\pi^2}{3} L_{\text{coil}}^2 \cdot BW^2 \right) \cdot BW = 0 \quad (3.7)$$

$$N_{\text{opt}} = \sqrt{\frac{\overline{e_n^2}}{\overline{i_n^2} \left(R_{\text{coil}}^2 + \frac{4\pi^2}{3} L_{\text{coil}}^2 BW^2 \right)}} \quad (3.8)$$

$$N_{\text{opt}} = \text{round} \left(\sqrt{\frac{\overline{e_n^2}}{\overline{i_n^2} \left(R_{\text{coil}}^2 + \frac{4\pi^2}{3} L_{\text{coil}}^2 BW^2 \right)}} \right) \quad (3.9)$$

$$N_{\text{opt}} = \text{round} \left(\sqrt{\frac{R_n^2}{R_{\text{coil}}^2 + \frac{4\pi^2}{3} L_{\text{coil}}^2 BW^2}} \right) \quad (3.10)$$

where $R_n = \frac{e_n}{i_n}$ is the equivalent noise resistance. A second derivative test

$$\frac{\overline{\partial^2 v_{n,in}^2(N)}}{\partial N^2} = \frac{2\overline{e_n^2}BW}{N^3} > 0 \text{ for } N > 0$$

shows that $\overline{v_{n,in}^2(N_{\text{opt}})}$ is a minimum. As a sanity check, if the inductance is set to zero, this result simplifies to the expected noise matching result for a purely resistive source: $N_{\text{opt}}R_{\text{coil}} = R_n \equiv e_n/i_n$. Plugging in the *exact* result for N_{opt} into $v_{n,in}^2(N)$ yields the minimum achievable integrated noise:

$$\overline{v_{n,in}^2(N_{\text{opt}})} = 4kTR_{\text{coil}} \cdot BW + \frac{\overline{e_n^2}}{\sqrt{\frac{\overline{e_n^2}}{\overline{i_n^2}\beta}}} \cdot BW + \sqrt{\frac{\overline{e_n^2}}{\overline{i_n^2}\beta}} \cdot \overline{i_n^2}\beta \cdot BW \quad (3.11)$$

$$\overline{v_{n,in}^2(N_{\text{opt}})} = 4kTR_{\text{coil}} \cdot BW + \sqrt{e_n^2 i_n^2 \beta} \cdot BW + \sqrt{e_n^2 i_n^2 \beta} \cdot BW \quad (3.12)$$

$$\overline{v_{n,in}^2(N_{\text{opt}})} = 4kTR_{\text{coil}} \cdot BW + 2P_n \sqrt{\beta} \cdot BW \quad (3.13)$$

$$(3.14)$$

where $P_n = e_n \cdot i_n$ is the input referred equivalent noise power and $\beta = R_{\text{coil}}^2 + \frac{4\pi^2}{3} L_{\text{coil}}^2 \cdot BW^2$. This result can be reformatted similar to when calculating Noise Factor to illustrate the contribution of the preamplifier noise compared to the total input referred integrated noise.

$$\overline{v_{n,in}^2(N_{\text{opt}})} = 4kTR_{\text{coil}} \cdot BW \left(1 + \frac{2P_n \sqrt{R_{\text{coil}}^2 + \frac{4\pi^2}{3} L_{\text{coil}}^2 BW^2}}{4kTR_{\text{coil}}} \right) \quad (3.15)$$

This result suggests that designing for the lowest integrated input noise requires amplifiers that have a low $P_n = e_n \cdot i_n$ input referred noise product. However, there is another design constraint we have to consider when noise matching inductive sensors.

3.3.2 Preventing In-Band Coil Resonance

When noise matching for inductive sensors, we have to be wary about the change in the coil's resonance frequency. The coil's self resonance frequency is:

$$f_r = \frac{1}{2\pi\sqrt{L_{\text{coil}}C_{\text{coil}}}} \quad (3.16)$$

where C_{coil} is the coil's winding capacitance. When amplifying the signal from the coil, the coil now sees the amplifier's input capacitance C_{in} , reducing the resonance frequency.

$$f_r = \frac{1}{2\pi\sqrt{L_{\text{coil}}C_{\text{coil}} + C_{in}}} \quad (3.17)$$

Adding parallel amplifiers scales the capacitance seen by the coil's inductance by N . For simplification, we assume the amplifier input capacitance C_{in} dominates over the winding capacitance.

$$f_r = \frac{1}{2\pi\sqrt{L_{\text{coil}}(C_{\text{coil}} + NC_{in})}} \quad (3.18)$$

$$f_r \approx \frac{1}{2\pi\sqrt{L_{\text{coil}} \cdot NC_{in}}} \text{ for } NC_{in} \gg C_{\text{coil}} \quad (3.19)$$

For robust signal reconstruction, the resonance frequency **should not** be within the signal bandwidth:

$$f_r = \frac{1}{2\pi\sqrt{L_{\text{coil}} \cdot NC_{in}}} \leq BW \quad (3.20)$$

Solving for the inequality yields the maximum value of N :

$$N_{max} = \text{round} \left(\frac{1}{4\pi^2 \cdot BW^2 \cdot L_{\text{coil}}C_{in}} \right) \quad (3.21)$$

This determines the upper limit of the noise matching factor N . We apply this inequality constraint to N_{opt} in equation 3.10.

$$N_{opt} \leq N_{max} = \frac{1}{4\pi^2 \cdot BW^2 \cdot L_{coil} C_{in}} \quad (3.22)$$

$$\sqrt{\frac{\overline{e_n^2}}{i_n^2 \left(R_{coil}^2 + \frac{4\pi^2}{3} L_{coil}^2 BW^2 \right)}} \leq \frac{1}{4\pi^2 \cdot BW^2 \cdot L_{coil} C_{in}} \quad (3.23)$$

$$\sqrt{\frac{\overline{e_n^2}}{i_n^2}} \leq \frac{\sqrt{R_{coil}^2 + \frac{4\pi^2}{3} L_{coil}^2 BW^2}}{4\pi^2 \cdot BW^2 \cdot L_{coil} C_{in}} \quad (3.24)$$

$$\frac{e_n}{i_n} C_{in} \lesssim \frac{\sqrt{\frac{4\pi^2}{3} L_{coil}^2 BW^2}}{4\pi^2 \cdot BW^2 \cdot L_{coil}} \text{ for } R_{coil} \ll L_{coil} BW \quad (3.25)$$

$$\frac{e_n}{i_n} C_{in} \lesssim \frac{\sqrt{\frac{4\pi^2}{3} L_{coil}^2 BW^2}}{4\pi^2 \cdot BW^2 \cdot L_{coil}} \quad (3.26)$$

$$\frac{e_n}{i_n} C_{in} \lesssim \frac{\frac{2\pi}{\sqrt{3}} L_{coil} BW}{4\pi^2 \cdot BW^2 \cdot L_{coil}} \quad (3.27)$$

$$R_n C_{in} \lesssim \frac{1}{2\pi\sqrt{3} \cdot BW} \quad (3.28)$$

where $R_n = \frac{e_n}{i_n}$ is again the equivalent noise resistance. This result shows that noise matching over a wide bandwidth requires low $R_n = \frac{e_n}{i_n}$ input referred noise ratio and low input capacitance C_{in} and can be used to check whether N_{opt} can be used, otherwise N_{max} must be used.

3.3.3 Optimization Goal

The constraint in equation 3.28 can be used to re-formulate the optimization problem to minimize for the lowest integrated input noise.

$$\begin{aligned} \text{Minimize: } & \frac{\overline{e_n^2}}{N} + N \cdot \overline{i_n^2} \left(R_{coil}^2 + \frac{4\pi^2}{3} L_{coil}^2 \cdot BW^2 \right) \\ \text{Subject to: } & N \leq \frac{1}{4\pi^2 \cdot BW^2 \cdot L_{coil} C_{in}} \end{aligned} \quad (3.29)$$

where the optimal N is:

$$N_{opt} = \begin{cases} \sqrt{\frac{\overline{e_n^2}}{i_n^2 \left(R_{coil}^2 + \frac{4\pi^2}{3} L_{coil}^2 BW^2 \right)}} & \text{for } R_n C_{in} \leq \frac{1}{2\pi\sqrt{3} \cdot BW} \\ \frac{1}{4\pi^2 \cdot BW^2 \cdot L_{coil} C_{in}} & \text{for } R_n C_{in} > \frac{1}{2\pi\sqrt{3} \cdot BW} \end{cases} \quad (3.30)$$

Designing the optimal preamplifier requires carefully selecting for low P_n to achieve low noise while having the required $R_n C_{in}$ to achieve the required bandwidth.

3.3.4 Unit Amplifier Selection

Designers have several options for unit amplifiers to choose from to build parallel amplifiers. They can construct preamplifiers from discrete Junction Field Effect Transistors (JFET), JFET OpAmps, and Bipolar Junction Transistor (BJT) OpAmps. The tradeoffs are as follows:

3.3.4.1 Discrete JFETS

Discrete JFETs have incredibly low current noise (on the order of a few fA/ $\sqrt{\text{Hz}}$) and low voltage noise (less than a nV/ $\sqrt{\text{Hz}}$). The drawbacks to discrete JFETs are very high input capacitance (10s to 100s of picofarads) and high device-to-device variation, making it hard to parallel many devices to decrease noise.

Advantages:

- Low input referred equivalent noise power P_n

Disdvantages:

- High input referred equivalent noise resistance R_n and input capacitance C_{in} make it hard to match over large bandwidth
- High device-to-device variation makes it hard to parallel many devices

3.3.4.2 JFET OpAmps

JFET OpAmps, similar to discrete JFETS, have very low current noise (on the order of a few fA/ $\sqrt{\text{Hz}}$) and low input capacitance (a few picofarads). Their drawbacks are moderately low voltage noise (on the order of a few nV/ $\sqrt{\text{Hz}}$).

Advantages:

- Low P_n and C_{in}

Disdvantages:

- High R_n make it hard to match over large bandwidth

3.3.4.3 BJT OpAmps

BJT OpAmps can have very low voltage noise (less than a nV/ $\sqrt{\text{Hz}}$) and low input capacitance (a few picofarads). Their drawbacks are higher current noise (on the order of pA/ $\sqrt{\text{Hz}}$).

Advantages:

- Low R_n and C_{in}

Disdvantages:

- Higher P_n suggests higher noise contribution from amplifier to overall system noise even with optimal matching.

3.3.4.4 Selecting an Appropriate Device

For low inductance receive coils ($< 10 \mu\text{H}$) typically used for relaxometry or spectroscopy or higher bandwidth applications ($> 1 \text{ MHz}$), BJT OpAmps may be more appropriate. For high inductance receive coils ($> 1 \text{ mH}$) used for MPI scanners or lower bandwidth applications ($< 1 \text{ MHz}$), JFET OpAmps may be more appropriate.

3.4 Methods

We apply this methodology to design an optimal preamplifier for the Arbitrary Waveform Relaxometer (AWR) system. The AWR uses a receive coil with a resistance $R = 0.3 \Omega$ and inductance $L = 3 \mu\text{H}$. The bandwidth requirement of the preamplifier for this system is motivated by the rich harmonic spectrum of SFMIOs. We set the bandwidth here to be 5 MHz, 5 times more than the 1 MHz bandwidth limit of the SR560 (Stanford Research Systems, Sunnyvale, CA) low-noise preamplifier we currently use.

Table 3.1: AWR Receive Chain Specifications

Specification	Value
Coil Resistance (R)	0.3Ω
Coil Inductance (L)	$3 \mu\text{H}$
Bandwidth	5 MHz

From the design methodology, the best unit amplifier for this application is a BJT input stage OpAmp. Currently, the lowest noise BJT OpAmp that is commercially available is the LMH6629 (Texas Instruments, Dallas, TX). It has a low voltage noise $e_n = 0.69 \text{ nV}/\sqrt{\text{Hz}}$, a moderate current noise $i_n = 2.6 \text{ pA}/\sqrt{\text{Hz}}$ and a moderate input capacitance $C_{in} = 1.7 \text{ pF}$. Its 900 MHz GBW is more than sufficient for a gain of 10 over 5 MHz. Table 3.2 shows the improved specifications of the LMH6629 over the SR560. Since $R_n C_{in} < \frac{1}{2\pi\sqrt{35} \text{ MHz}}$, the optimal number of parallel amplifiers will be the result from equation 3.10,

$$N_{opt} = \text{round} \left(\sqrt{\frac{(0.69 \text{ nV}/\sqrt{\text{Hz}})^2}{2.6 \text{ pA}/\sqrt{\text{Hz}} \left(0.3 \Omega^2 + \frac{4\pi^2}{3} (3 \mu\text{H})^2 (5 \text{ MHz})^2 \right)}} \right) = 5 \quad (3.31)$$

whereas the high R_n and C_{in} of the SR560 only allows for a maximum of 3 devices in parallel even though the optimal number of devices is about 32. It is important to note that there is diminishing and even deteriorating returns on the number of devices to add in parallel, as shown in Figure 3.5. This is because the current noise contribution will start to dominate at higher frequencies. The frequency at which this crossover occurs is when the voltage noise and current noise are equivalent:

$$\overline{e_n^2} = i_n^2 \left((2\pi f L_{\text{coil}})^2 + R_{\text{coil}}^2 \right) \quad (3.32)$$

$$\frac{\overline{e_n^2}}{i_n^2} = 4\pi^2 f^2 L_{\text{coil}}^2 + R_{\text{coil}}^2 \quad (3.33)$$

$$R_n^2 = 4\pi^2 f^2 L_{\text{coil}}^2 + R_{\text{coil}}^2 \quad (3.34)$$

$$f = \sqrt{\frac{R_n^2 - R_{\text{coil}}^2}{4\pi^2 L_{\text{coil}}^2}} \quad (3.35)$$

$$(3.36)$$

For $R_{\text{coil}} \ll R_n$, we can approximate the noise corner frequency as:

$$f \approx \frac{R_n}{2\pi L_{\text{coil}}} \quad (3.37)$$

Note that increasing N decreases the effective R_n , so the corner frequency also decreases with N . Figures 3.4 and 3.4 illustrate the inflection point and decrease in corner frequency with increased N .

Table 3.2: Low Noise Preamplifier Specifications

Specification	This Work	SR560
Noise Voltage e_n	0.69 nV/ $\sqrt{\text{Hz}}$	4 nV/ $\sqrt{\text{Hz}}$ @ 1 kHz, 3.4 nV/ $\sqrt{\text{Hz}}$ @ 100 kHz
Noise Current i_n	2.6 pA/ $\sqrt{\text{Hz}}$	8 fA/ $\sqrt{\text{Hz}}$
Bandwidth ($G = 10$)	90 MHz	1 MHz
Input Capacitance C_{in}	1.7 pF	25 pF
N'_{opt}	5	32
N'_{opt} meets BW Constraint?	Yes	No

Table 3.3: Specifications of the LMH6629 Unit OpAmp used in this work compared to the commercial SR560 preamplifier show a much lower voltage noise, larger bandwidth, and lower input capacitance.

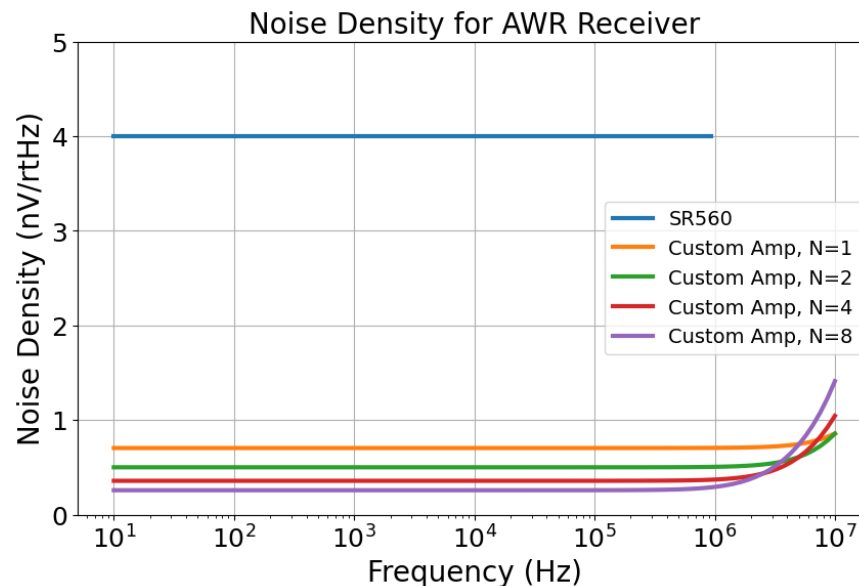


Figure 3.3: Simulations show that the custom preamplifier designed with $N=5$ LMH6629 parallel opamps achieves 10-fold improved SNR compared to the SR560 commercial preamp. Note also how important it is to optimize the correct number, N , of parallel amps for bandwidth. While $N = 8$ preamps shows reduced low frequency noise density, it also shows a rapid noise density increase above 5 MHz for $N = 8$. Our optimization procedure balances these effects by minimizing the total integrated noise.

It is important to also consider all possible components in an amplifier design that contribute to noise. In this case, for a non-inverting amplifier that uses the LMH6629, the gain setting resistors also add noise. Flicker noise or $1/f$ noise also needs to be considered. Simulations in LTSpice (Analog Devices Inc., Wilmington, MA) which factor in all these noise sources. SPICE simulations validate that $N = 5$ is the optimal number of amplifiers (Figure 3.5.)

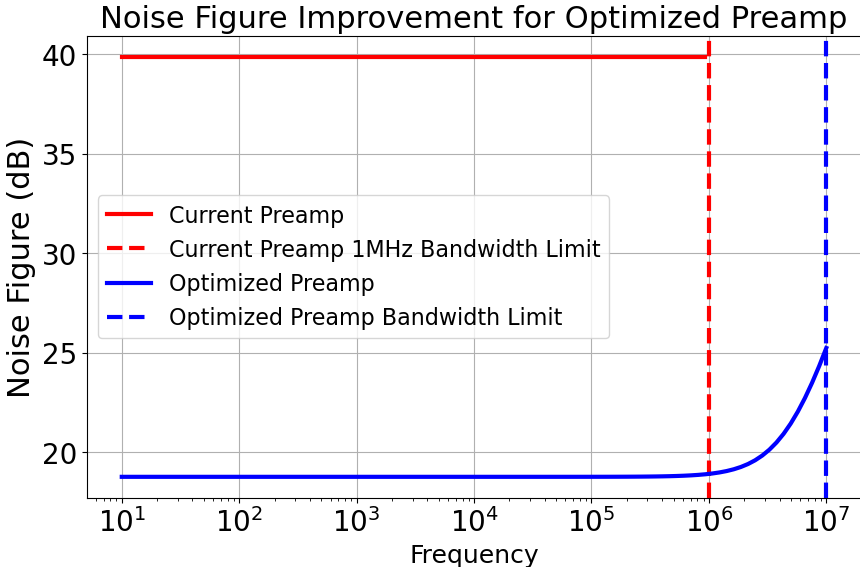


Figure 3.4: Simulations show that the optimized custom preamplifier with $N = 5$ parallel unit amplifiers achieves more than a ten-fold SNR boost (20 dB noise figure improvement) across the desired receive bandwidth.

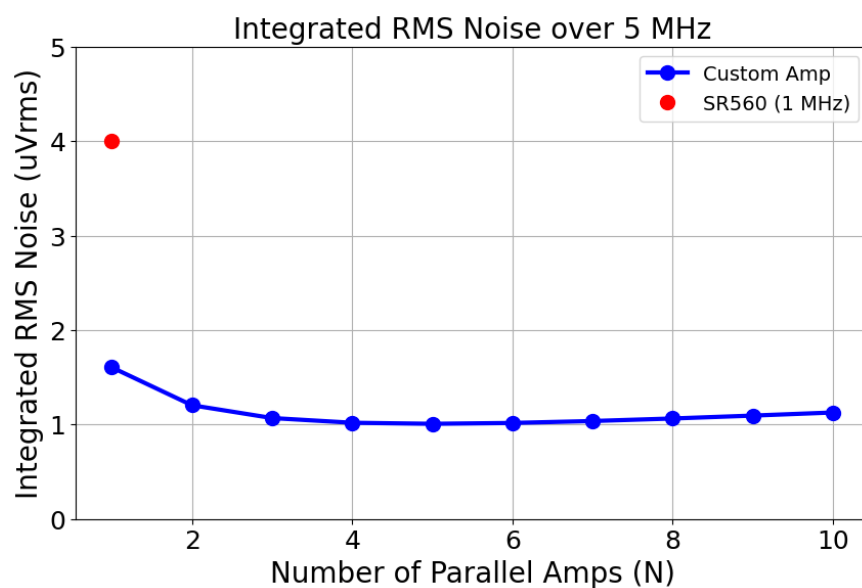
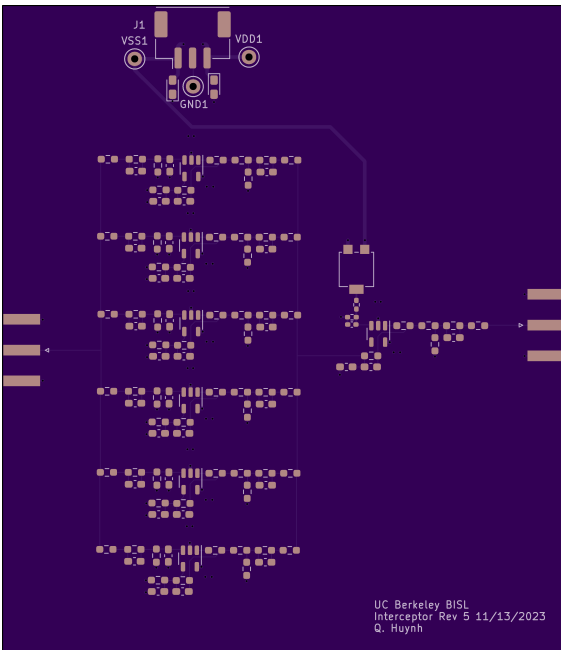


Figure 3.5: SPICE Simulations show that the integrated root-mean-square (RMS) noise for the optimized custom preamplifier has 4x lower noise over 5x larger bandwidth. Note that the minimum integrated RMS noise is very shallow as a function of the number of parallel unit amplifiers. Note that this doesn't match the 10-fold boost from Figure 3.4 since the integrated bandwidth for the custom preamp is 5x that of the SR560, resulting in 2.5x increased integrated noise.

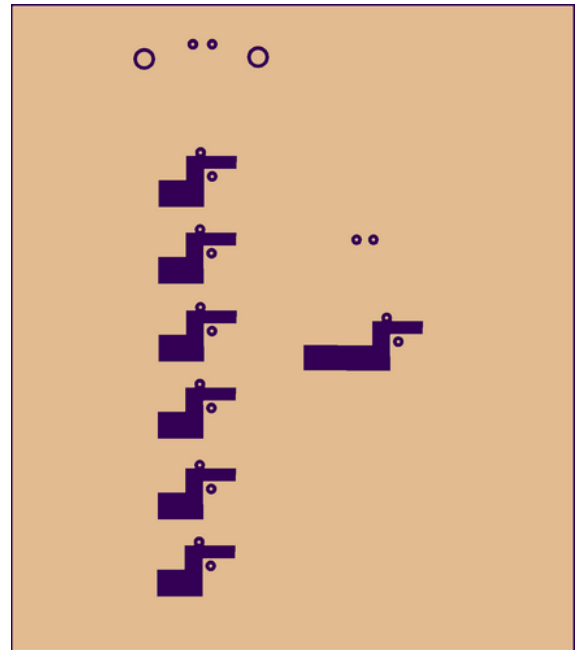
3.4.1 Circuit Board Design and Construction

Printed circuit board (PCB) layout of the low noise preamplifier requires a few considerations to maintain low noise and stability. Power was routed such that there is a nearby return path through ground and on a different plane from the signal. Decoupling and bypass capacitors were placed nearby the power pins of the amplifiers. Bulk capacitors were placed further away. Ground was kept out of high impedance and sensitive nodes such as the feedback pin of the amplifier, reducing parasitic capacitance and maintaining stability. Input traces were kept thin and short to reduce the effect of parasitic capacitance on input capacitance. Layout was done using KiCAD software [50] and fabricated through OSH Park (OSH Park LLC Lake Oswego, OR).

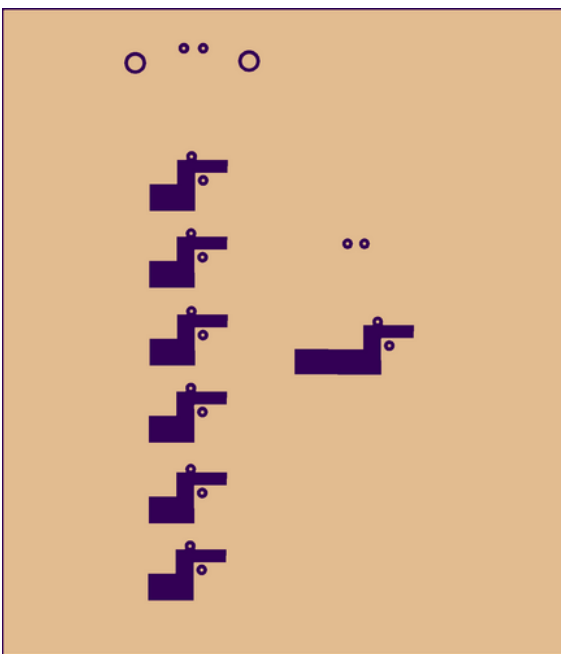
We construct a printed circuit board that consists of two stages. The first stage is the 5 parallel amplifiers using the LMH6629 unit preamplifier. Each unit amplifier is a non-inverting amplifier with a gain of $A_v = 10$ using $R_1 = 27$ and $R_2 = 249$. Shunt input resistors of $R_{in} = 50 \Omega$ at the non-inverting input along with the equivalent resistance seen at the inverting input were used to balance the input bias current. Each stage has a $R_{out} = 50 \Omega$ to balance the output and provide a branch for the output current to flow into the virtual ground of the second stage. The second stage is an inverting summing amplifier also using the LMH6629. The effective gain is $A_v = \frac{R_f}{R_{out}/5} = 10$ with $R_f = 100$. Shunt capacitors were placed across R_2 and R_f to set the cut-off frequency at 5 MHz.



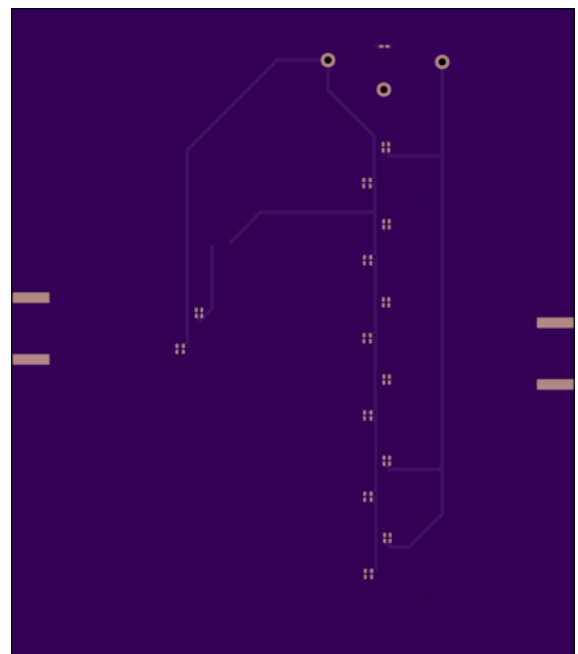
(a) Top Layer



(b) In1 Layer



(c) In2 Layer



(d) Bottom Layer

Figure 3.6: Layout of Preamplifier PCB. In Figs. 3.6b and 3.6b, the ground planes were removed from the inverting input nodes of the amplifiers to reduce parasitic capacitance and prevent instability. In Figure 3.6d, $0.1\ \mu\text{F}$ and $0.01\ \mu\text{F}$ decoupling capacitors were placed close to the supply pins of the amplifiers. $10\ \mu\text{F}$ tantalum capacitors were placed closer to the power inputs of the board.

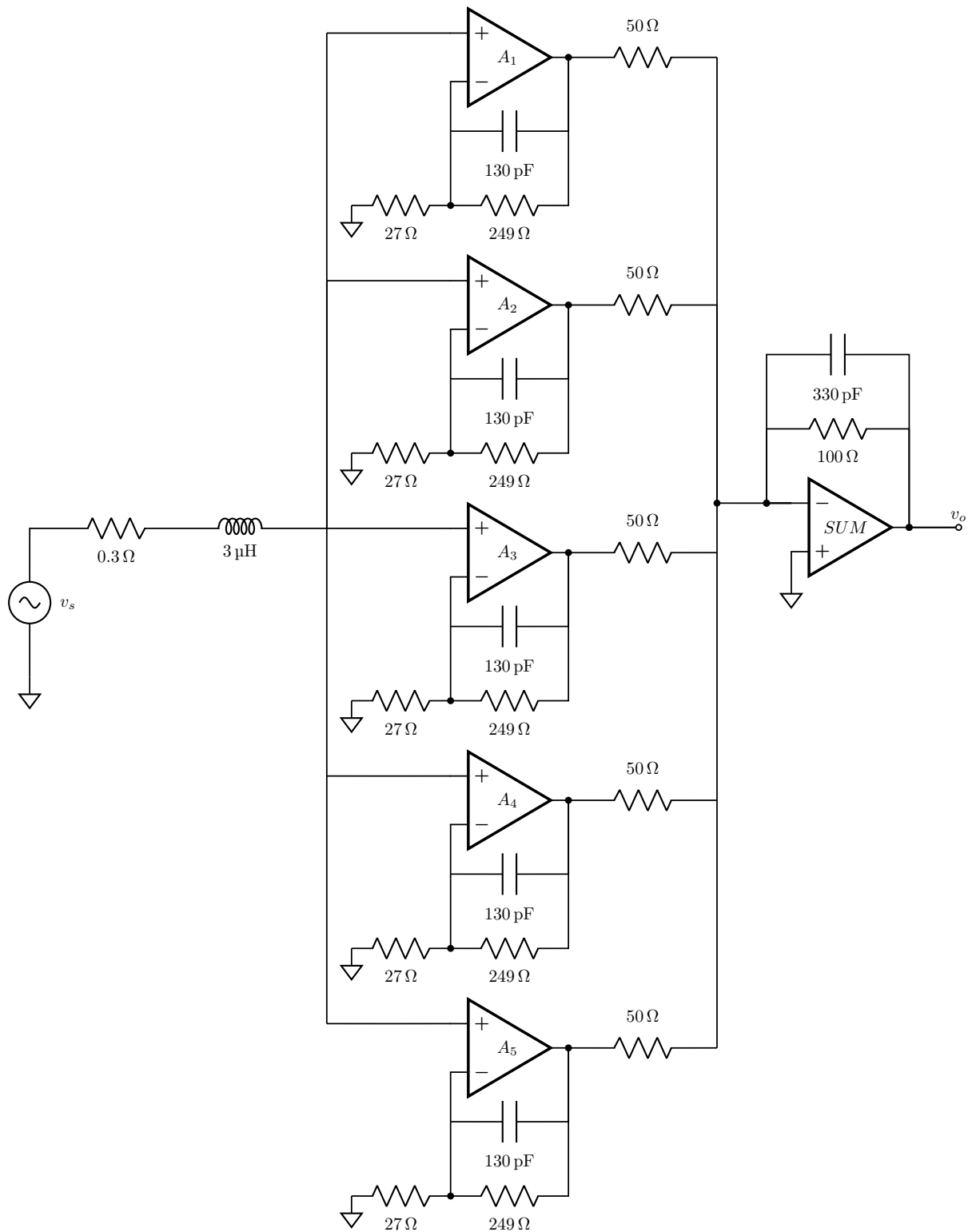


Figure 3.7: The optimal design methodology yields a preamplifier circuit that with 5 parallel amplifiers in the first stage. The second stage is an inverting summing amplifier with gain of 10. Capacitors were placed in shunt with the feedback resistors of each stage to set a low-pass filter cut-off frequency at 5 MHz.

3.5 Results

3.5.1 Experimental Noise Data

We validate the theory and simulation results above by testing the constructed amplifier with SPIO and SFMIO nanoparticles. We first measure the noise of the SR560 and custom optimized preamplifiers with the receive coil attached, and no excitation or particles using the 16-bit 10MSPS ADC of the PicoScope 4262 (Pico Technology, St Neots, UK). The custom preamp measured an input rms noise of $0.9\ \mu\text{V}$, very close to the simulated noise of roughly $1\ \mu\text{V}$. The SR560 measured $5.2\ \mu\text{V}$, a little higher than the simulated $4\ \mu\text{V}$. This can be explained due to the fact that the frequency response of the SR560 is not a brick wall filter at 1 MHz. We can use the equivalent noise bandwidth $\text{ENBW} = \frac{\pi}{2}BW \approx 1.57\ \text{MHz}$, approximating the preamplifier's frequency response as a first order low pass filter [51]. This results in an integrated noise of $\sqrt{(3.4\ \text{nV}/\sqrt{\text{Hz}})^2 \cdot (1.57\ \text{MHz})} = 5.2\ \mu\text{V}$, which agrees well with the measured noise data.

We then measure the noise spectrum of the two preamplifiers with the inputs shorted to validate the noise density over bandwidth using a SSA3021X Spectrum Analyzer (SIGLENT TECHNOLOGIES, Solon, Ohio). Figure 3.9 shows that the experimental noise data agrees with the simulated noise density, with the custom preamplifier achieving $e_n = 300\ \text{pV}/\sqrt{\text{Hz}}$, more than a 10-fold improvement over the SR560.

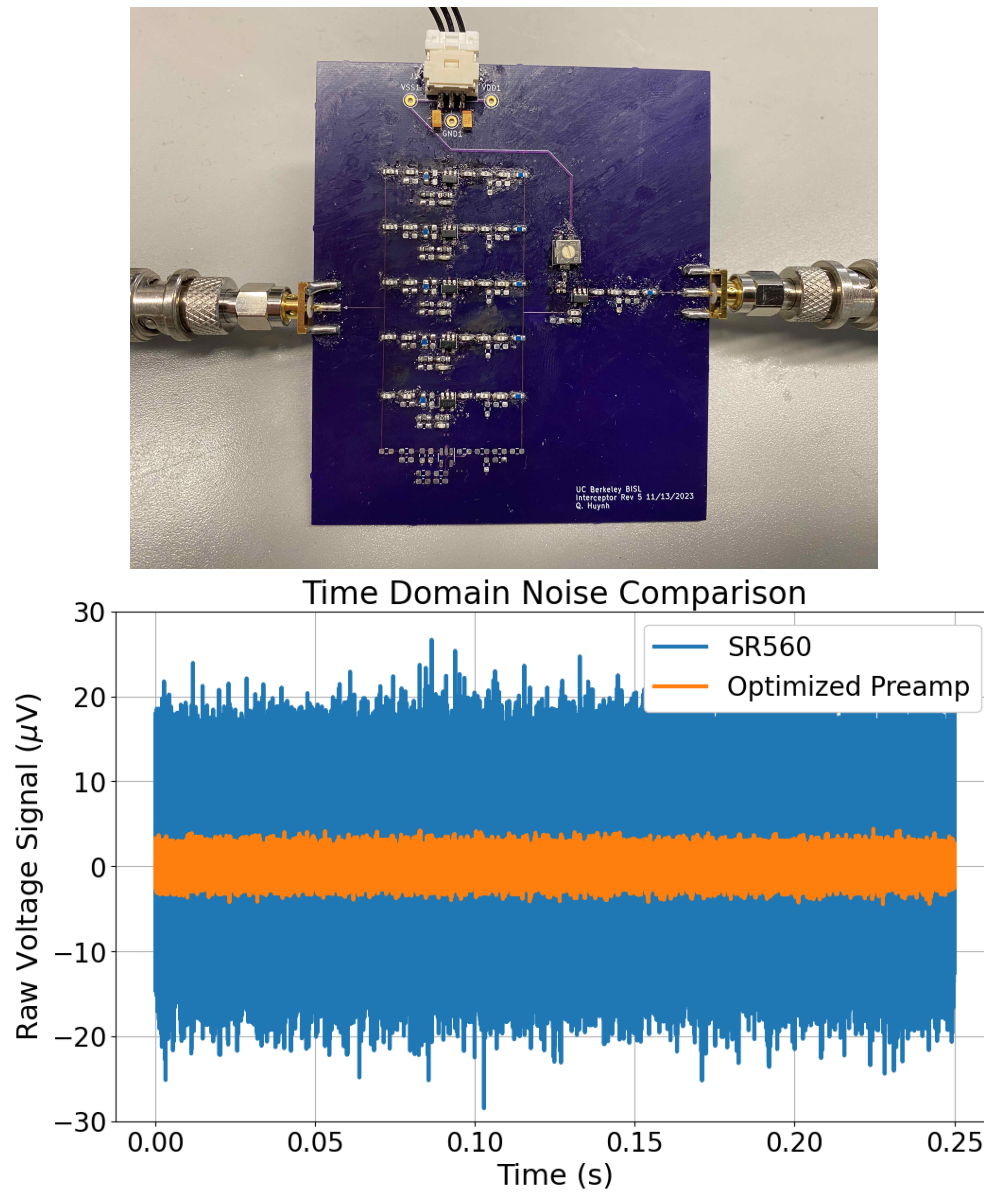


Figure 3.8: Constructed Preamp PCB shows a factor of more than 4 decrease in noise. Input referred integrated noise of the optimized preamplifier was measured to be $0.9 \mu\text{V}$ whereas the SR560 preamplifier measured $5.2 \mu\text{V}$ noise.

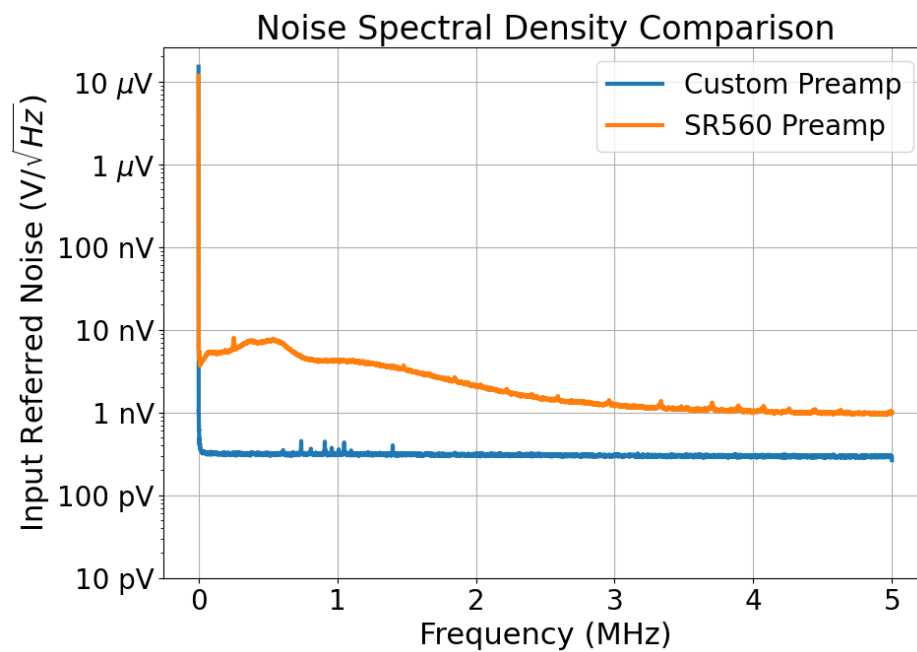


Figure 3.9: Custom optimized preamplifier achieves $e_n = 300 \text{ pV}/\sqrt{\text{Hz}}$, more than a 10-fold improvement over the SR560's $e_n = 3.4 \text{ nV}/\sqrt{\text{Hz}}$ over a wider bandwidth. Data was collected with a spectrum analyzer and the inputs to the amplifier shorted.

3.5.2 Experimental SPIO Data

To showcase the improved noise of the custom preamplifier, we evaluate the preamp board with a serial dilution of Ferucarbotran (VivoTrax™, Magnetic Insight Inc., Alameda, CA) using the AWR. The AWR's transmit chain consists of an AE7224 Power Amplifier (AE Techron, Elkhart, IN) driving the excitation waveform generated by the 12-bit DAC channel of an PCI-6115 (National Instruments, Austin, TX) Data Acquisition (DAQ) Module. The receive chain consists of the preamplifier (this work's custom preamplifier) and/or the SR560 preamplifier) and the 14-bit ADC channels of the PCI-6115. The scan parameters for these acquisitions were as follows: 20 mT 20 kHz sinusoidal excitation for 0.25 second acquisitions. The experimental data show that the custom preamplifier board achieves roughly 200 ng iron limit of detection whereas the SR560 only achieves 1 μg , a factor of 5 improvement in signal-to-noise ratio.

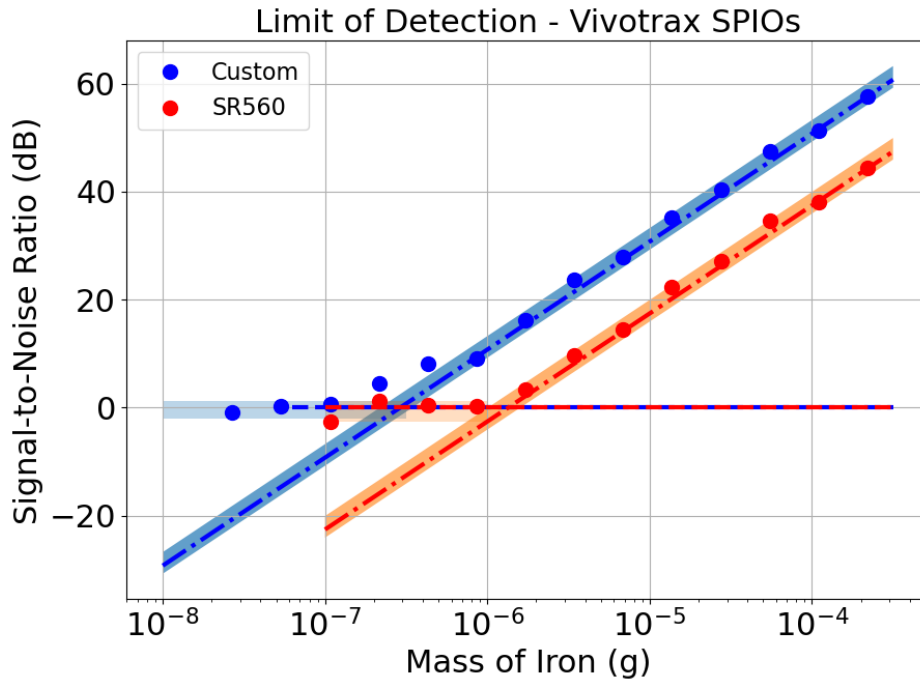


Figure 3.10: 20 mT 20 kHz sinusoidal excitation for 0.25 second acquisitions of serial dilution of VivoTrax™ show that the custom preamplifier board achieves roughly 200 ng iron limit of detection whereas the SR560 only achieves 1 μg . This experimentally confirms the 5-fold boost in SNR from optimal noise matching. This experiment also confirms that with just 25 seconds of averaging, our AWR design should detect roughly $200\text{ng}/\sqrt{25\text{s}/0.25\text{s}} = 20\text{ ng}$ of SPIOs.

3.5.3 Experimental SFMIO Data

To really showcase the improvement of the custom optimized preamplifier, we evaluate its performance against the SR560 preamplifier with superferromagnetic iron oxide nanoparticles developed by the group using the AWR. The sharp magnetic transitions of these particles leads to higher spatial resolution. This improved resolution also lends to higher order harmonics in the signal acquisition for a sinusoidal excitation. Figure 3.11 shows that the improved bandwidth of the custom optimized preamplifier exposes more of the harmonics in SFMIO signal acquisition. In reconstruction of the point spread function (PSF), the PSF of the SFMIO signal is improved by 23 percent over the PSF of the SFMIO signal acquired by the SR560 preamplifier.

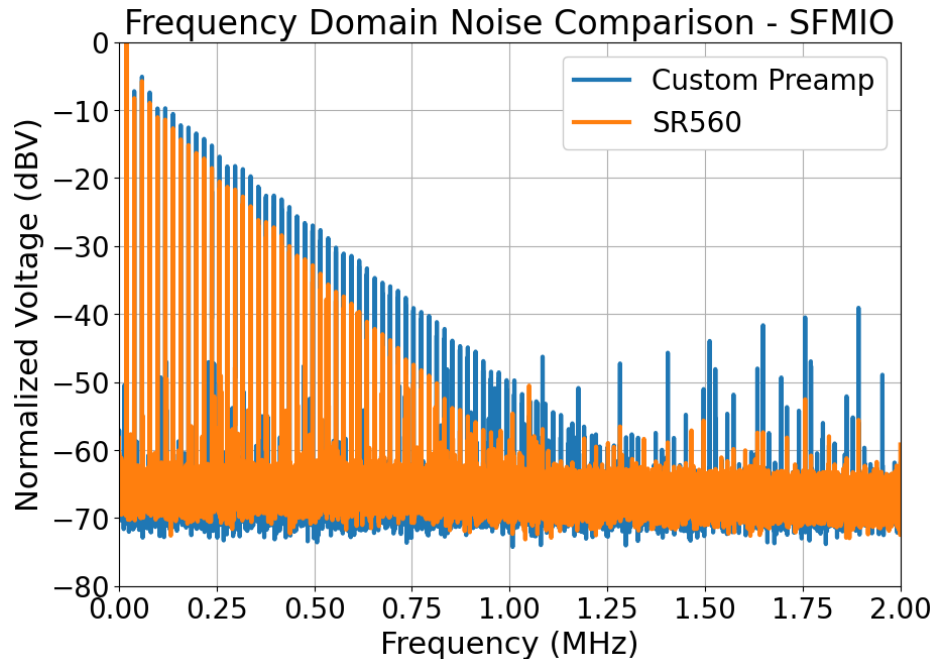


Figure 3.11: Improved bandwidth of the custom optimized preamplifier exposes more of the harmonics in SFMIO signal acquisition. The scan parameters were $f_0 = 20$ kHz, 20 mT sinusoidal excitation for 0.25 seconds. Even with shielding, the AWR’s receiver unfortunately still acts as a great pickup coil for other EMI sources such as local AM radio stations. Further shielding can be done by placing the receive frontend in a Faraday cage.

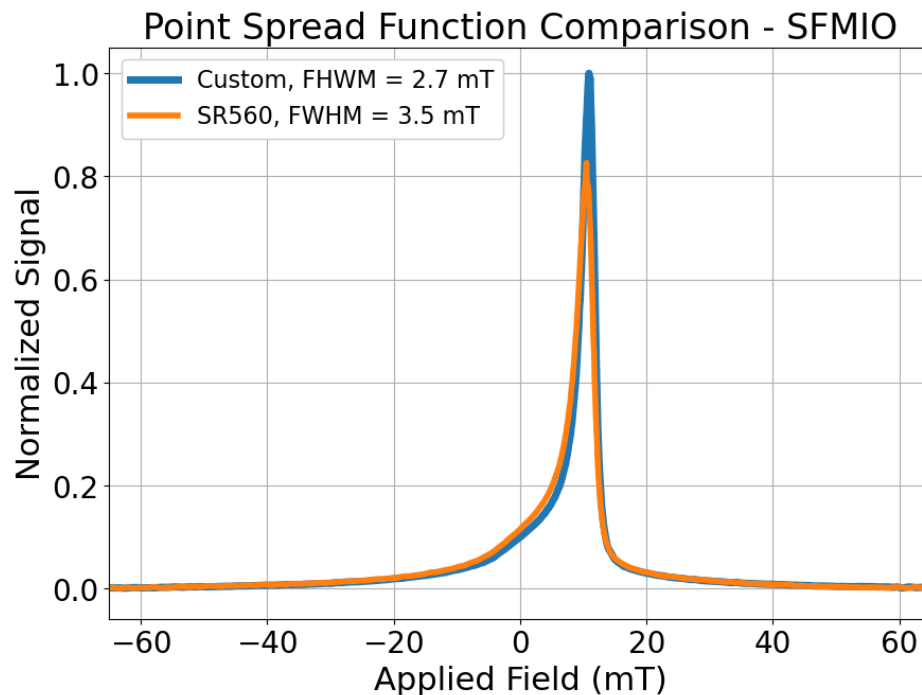


Figure 3.12: PSF of the SFMIO signal acquired by the custom optimized preamplifier is improved by 23 percent over the PSF of the SFMIO signal acquired by the SR560 preamplifier.

3.6 Conclusion

In this work, a design methodology for optimized preamplifiers was introduced for MPI receive frontends. Using this methodology, we designed a preamplifier that achieved an incredible 10-fold better noise figure and 5-fold better integrated noise over a 5-fold increased bandwidth. This methodology can apply to any inductive sensor system. Particularly in MPI, this methodology can be used to achieve very close to coil noise dominance. Achieving higher SNR in MPI is crucial to cell tracking applications, where labelling efficiency may be poor and tracking 10s to 100s of cells is desired.

Chapter 4

Receive Coil Optimization with Microcoil Design Improves Sensitivity

4.1 Introduction

MPI preclinical scanners require electromagnetic receive coils of roughly 4-cm bore size. Clinical MPI scanners will need much larger receive coils, approaching 65-cm bore sizes for whole-body human scanners [23], [24]. Previous works have shown methods for coil design of MPI preclinical scanners [26], [52], but benchtop particle relaxometers such as the Arbitrary Waveform Relaxometer (AWR) and Magnetic Particle Spectrometers (MPS) do not have to adhere to this bore size constraint and can focus on improvement of signal-to-noise ratio (SNR) per volume of SPIOs for characterization and analysis. Mass-limited and volume-limited analysis of samples is primarily motivated by reducing the need to take large aliquot samples of iron-oxide nanoparticles during the synthesis process, as these aliquots are no longer able to be returned to the original synthesis solution once analyzed. Improved sensitivity also reduces the required signal acquisition time, speeding up analysis. Previous works in Nuclear Magnetic Resonance (NMR) have used microcoil design to accomplish *order-of-magnitude* improvements in sensitivity per sample volume [53]. Microcoils exhibit improved sensitivity due to increased coil efficiency \mathbf{B} and reduced coil resistance [54] as a result of much smaller coil radii — hence the term microcoils. This has enabled NMR analysis of mass-limited and volume-limited samples [55], [56], spawning a whole field in RF microcoil design.

Here we aim to achieve, for the first time, roughly the same 10-fold gains in SNR per fixed volume as previous works in NMR microcoil design for novel AWR and MPS table-top scanners.

4.2 Theory and Methods

Here we first model the receive coil signal per volume of sample and geometric parameters. Then we model the noise as a function of the same parameters. We will then model the signal-to-noise ratio and attempt to optimize for it:

$$\text{SNR} = \frac{\text{signal}_{\text{coil}}/\text{volume}}{\text{noise}_{\text{coil}}} . \quad (4.1)$$

4.2.1 Modelling the Coil Signal

Typical receive coils used in magnetic particle relaxometers and spectrometers are solenoids [34]. The sensitivity of solenoids can be determined from the principle of reciprocity [15], where the receive sensitivity of an electromagnetic coil is the same as its ability to transmit and generate a magnetic field (coil efficiency B with units of [mT/A]). In this work we will use coil sensitivity and coil efficiency interchangeably. The on-axis sensitivity of a solenoid of length ℓ , radius r , number of turns N , and current I is

$$B(z) = \frac{\mu_0 I N}{2\ell} \left[\frac{z + \ell/2}{\sqrt{(z + \ell/2)^2 + r^2}} - \frac{z - \ell/2}{\sqrt{(z - \ell/2)^2 + r^2}} \right] \quad (4.2)$$

where the field at the center of the coil is

$$B(z = 0) = \frac{\mu_0 I N}{\sqrt{\ell^2 + 4r^2}} . \quad (4.3)$$

This assumes a single layer, tightly wound and packed solenoid at low enough frequencies where we can neglect frequency dependence due to the quasi-static approximation. We will discuss the skin effect in a later section. When a sample is placed in the receive coil, it is ideal for it to take up most of the coil's extent (from $z = -\ell/2$ to $z = \ell/2$) for the best sensitivity. The total particle signal captured by the receive coil (assuming a homogeneous particle sample solution covers the coil extent) is proportional to the spatial integration over the length of the coil.

$$\text{signal}_{\text{coil}} \propto \int_{-\ell/2}^{\ell/2} \frac{\mu_0 I N}{2\ell} \left[\frac{z + \ell/2}{\sqrt{(z + \ell/2)^2 + r^2}} - \frac{z - \ell/2}{\sqrt{(z - \ell/2)^2 + r^2}} \right] dz \quad (4.4)$$

$$\propto \frac{\mu_0 I N}{2\ell} \left[\sqrt{(z + \ell/2)^2 + r^2} - \sqrt{(z - \ell/2)^2 + r^2} \right]_{z=-\ell/2}^{z=\ell/2} \quad (4.5)$$

$$\propto \frac{\mu_0 I N}{2\ell} \left[\sqrt{\ell^2 + r^2} - \sqrt{r^2} - \left(\sqrt{r^2} - \sqrt{\ell^2 + r^2} \right) \right] \quad (4.6)$$

$$\text{signal}_{\text{coil}} \propto \frac{\mu_0 I N}{\ell} \left(\sqrt{\ell^2 + r^2} - r \right) \quad (4.7)$$

$$\text{signal}_{\text{coil}}/\text{volume} \propto \frac{\mu_0 I N}{\ell} \left(\sqrt{\ell^2 + r^2} - r \right) / V \quad (4.8)$$



Figure 4.1: An example of a receive solenoid coil is pictured above. Typically receive coils for the AWR are litz wire solenoids to reduce the skin effect.

For analysis of SNR per volume, we must hold the volume of the coil constant. We define a constant volume V over which the radius r is varied. We also define a coil gauge w_c that is the width of the coil. Since volume and radius are known, we can determine ℓ from

$$V = \pi r^2 \ell \quad (4.9)$$

$$\ell = \frac{V}{\pi r^2} \quad (4.10)$$

Since the coil length of a single-layer coil is known, we can determine the number of turns N :

$$N = \frac{\ell}{w_c} . \quad (4.11)$$

We plug the values of ℓ and N back into the coil signal model equation 4.8:

$$\text{signal}_{\text{coil}}/\text{volume} (r, V, w_c) \propto \frac{\mu_0 I (\frac{\ell}{w_c})}{\ell} \left(\sqrt{\left(\frac{V}{\pi r^2}\right)^2 + r^2} - r \right) / V \quad (4.12)$$

$$\propto \frac{\mu_0 I}{w_c} \left(\sqrt{\frac{V^2}{\pi^2 r^4} + r^2} - r \right) / V . \quad (4.13)$$

4.2.2 Modelling the Coil Noise

Here we model the noise of the receive coil in terms of its geometric parameters. The noise in a coil is due to the thermal noise of the coil winding resistance.:

$$R_{\text{coil}} = \rho \frac{N \cdot 2\pi r}{\pi w_c^2}, \quad (4.14)$$

$$R_{\text{coil}} = \frac{2\rho\pi r}{\pi w_c^2} \frac{V}{w_c\pi r^2}, \quad (4.15)$$

$$R_{\text{coil}}(r, V, w_c) = \frac{2\rho V}{\pi w_c^3 r}. \quad (4.16)$$

where ρ is the resistivity of copper. Since this is only the DC resistance, we must also consider the skin effect.

$$\delta(f) = \sqrt{\frac{\rho}{\pi f \mu_0}} \quad (4.17)$$

The AC resistance is then

$$R_{AC} = \frac{w_c^2}{w_c^2 - (w_c - \delta(f))^2} R_{\text{coil}}(r, V, w_c) \quad (4.18)$$

To mitigate the increased AC resistance due to skin effect we use 100/44 served litz wire, which has a nominal wire strand diameter of 51 μm . This means that skin effect is negligible for frequencies up to 1.7 MHz and more than adequate enough for MPI/MPS frequencies (DC - 1 MHz) unlike NMR which uses frequencies from 100 MHz up to 800 MHz depending on the strength of the magnet. Therefore we can treat $R_{AC} \approx R_{DC}$.

However, this is not the only source of noise in the system. We have to amplify the coil signal with a preamplifier, which has its own noise sources in the form of input referred voltage noise e_n and input referred current noise i_n . Due to the current noise contribution and frequency dependent coil impedance, the coil's inductance also affects noise over BW . The inductance of a single-layer solenoid is a well-modelled empirical function of its geometry [11]:

$$L_{\text{coil}} = \frac{r^2 N^2}{9r + 10\ell}, \quad (4.19)$$

$$L_{\text{coil}} = \frac{r^2 \frac{V^2}{\pi^2 r^4 w_c^2}}{9r + 10 \frac{V}{\pi r^2}}, \quad (4.20)$$

$$L_{\text{coil}} = \frac{V^2}{\pi^2 r^2 w_c^2 \left(9r + 10 \frac{V}{\pi r^2}\right)}, \quad (4.21)$$

$$L_{\text{coil}}(r, V, w_c) = \frac{V^2}{9\pi^2 r^3 w_c^2 + 10\pi w_c^2 V}. \quad (4.22)$$

Note that the formula is empirical and uses imperial units (inches), yielding the inductance in microhenries. The total integrated noise due to the coil can therefore be written as

$$\text{noise}_{\text{coil}} = \sqrt{4kTR_{\text{coil}}(r, V, w_c) \cdot BW + \overline{e_n^2} \cdot BW + \overline{i_n^2} \left(R_{\text{coil}}(r, V, w_c)^2 + \frac{4\pi^2}{3} \overline{i_n^2} L_{\text{coil}}(r, V, w_c)^2 \cdot BW^2 \right) \cdot BW} \quad (4.23)$$

$$= \sqrt{8kT \frac{\rho V}{\pi w_c^3 r} \cdot BW + \overline{e_n^2} \cdot BW + \overline{i_n^2} \left(\frac{4\rho^2 V^2}{r^2 w_c^2} + \frac{4\pi^2}{3} \overline{i_n^2} \frac{V^2}{(9\pi^2 r^3 w_c^2 + 10\pi w_c^2 V)^2} \cdot BW^2 \right) \cdot BW} \quad (4.24)$$

For full derivation of the integrated noise of an inductive sensor, see equation 3.4 in chapter 3.

4.2.3 Final Signal-to-Noise Ratio Model

Putting the two models together, we get a finalized SNR model of

$$\text{SNR} = \frac{\text{signal}_{\text{coil}}/\text{volume}}{\text{noise}_{\text{coil}}} \quad (4.25)$$

$$\text{SNR} \propto \frac{\frac{\mu_0 I}{w_c} \left(\sqrt{\frac{V^2}{\pi^2 r^4} + r^2} - r \right) / V}{\sqrt{8kT \frac{\rho V}{\pi w_c^3 r} \cdot BW + \overline{e_n^2} \cdot BW + \overline{i_n^2} \left(\frac{4\rho^2 V^2}{r^2 w_c^2} + \frac{4\pi^2}{3} \overline{i_n^2} \frac{V^2}{(9\pi^2 r^3 w_c^2 + 10\pi w_c^2 V)^2} \cdot BW^2 \right) \cdot BW}} \quad (4.26)$$

4.2.4 SNR Model Sensitivity Analysis

Unfortunately for this model, there is no global maximum. A closer look at the $\text{signal}_{\text{coil}}/\text{volume}$ formula shows that the signal increases roughly quadratically with decreasing r when the first term of the radicand of equation 4.24 dominates.

$$\frac{\partial \text{signal}_{\text{coil}}/\text{volume}}{\partial \frac{1}{r}} \propto r^2 \quad \text{for } r \ll \sqrt[3]{\frac{V}{\pi}} \quad (4.27)$$

To understand how SNR changes with decreasing radius we explore the three cases of noise dominance to determine the sensitivity to decreasing r - when the coil noise is dominant, when the preamplifier e_n is dominant, and when $i_n \cdot Z_{\text{coil}}$ is dominant.

4.2.4.1 Coil Noise Dominance

When the coil noise is dominant, only the first term $8kT \frac{\rho V}{\pi w_c^2 r} \cdot BW$ contributes significantly to noise. The noise increases with decreasing r as follows:

$$\frac{\partial \text{noise}_{\text{coil}}}{\partial \frac{1}{r}} \propto \sqrt{r} \quad (4.28)$$

4.2.4.2 Preamplifier Voltage Noise Dominance

When the preamplifier voltage noise e_n dominates, then the noise does not change with decreasing r and remains relatively constant.

$$\frac{\partial \text{noise}_{\text{coil}}}{\partial \frac{1}{r}} = 1 \quad (4.29)$$

4.2.4.3 Preamplifier Current Noise Dominance due to Coil Inductance

When the preamplifier current noise and coil impedance $i_n \cdot Z_{\text{coil}}$ dominates, then the noise increases with decreasing r as follows:

$$\frac{\partial \text{noise}_{\text{coil}}}{\partial \frac{1}{r}} \propto \sqrt{r^3} \quad \text{for } r \gg \sqrt[3]{\frac{10V}{9\pi}} \quad (4.30)$$

$$\frac{\partial \text{noise}_{\text{coil}}}{\partial \frac{1}{r}} \propto r \quad \text{for } r \ll \sqrt[3]{\frac{10V}{9\pi}} \quad (4.31)$$

With three different noise dominances, we analyze the sensitivity of the SNR model to decreasing r .

Noise Dominant Regime	Change with $1/r$	Vernier Slope (dB/dec) of r
Coil Noise	$r^{3/2}$	30 dB/dec
Preamp Voltage Noise	r^2	40 dB/dec
Preamp Current Noise	$r^{1/2} \sim r$	10 \sim 20 dB/dec

Table 4.1: For each of the noise dominance regimes, the slope of the SNR curve with respect to r changes. Generally the coil noise should be dominant for best SNR and noise figure.

4.3 Results

To validate this model we simulate the construction of microcoils of 100 nL, 10 μ L, and 1 mL volumes from 10 μ m to 10 cm radii. We determine the sensitivity, inductance, resistance,

and finally the SNR/volume as a function of coil radius. For SNR/volume, the preamplifier is modelled to be the optimized preamplifier in 3, with $0.3 \text{ nV}/\sqrt{\text{Hz}}$ and $6 \text{ pA}/\sqrt{\text{Hz}}$. We see that from these plots that it is challenging to achieve coil noise dominance, but it is worth decreasing the coil radius until we start reaching diminishing returns in order to improve SNR/volume. Another factor to consider is construct-ability. While winding 1-10 turn(s) to construct a coil is feasible, winding 100s to 1000s of turns may not be.

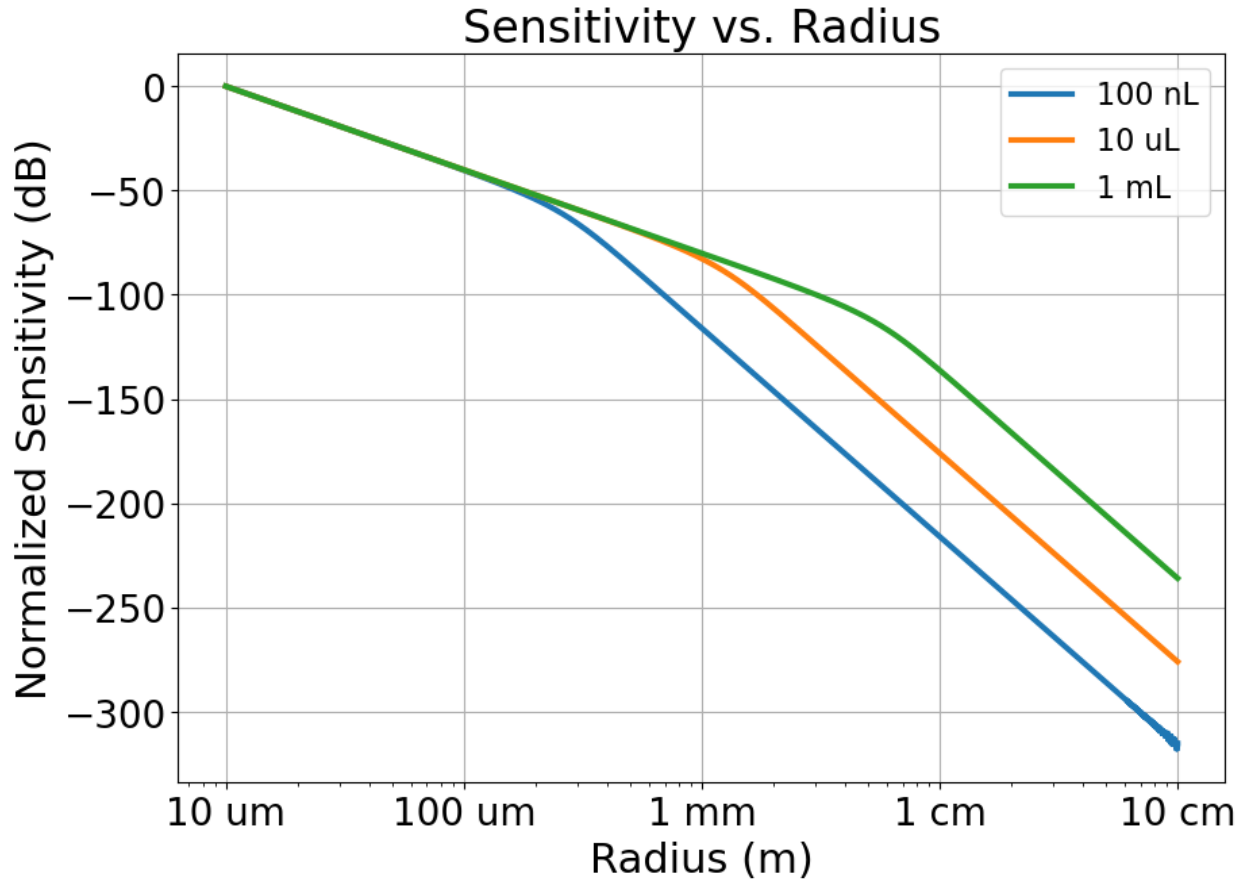


Figure 4.2: Decreasing radius shows a 40 dB/decade increase with sensitivity. Note that this regime is only when $r \ll \sqrt[3]{\frac{V}{\pi}}$. Outside this regime, the sensitivity of the coil per volume is weaker.

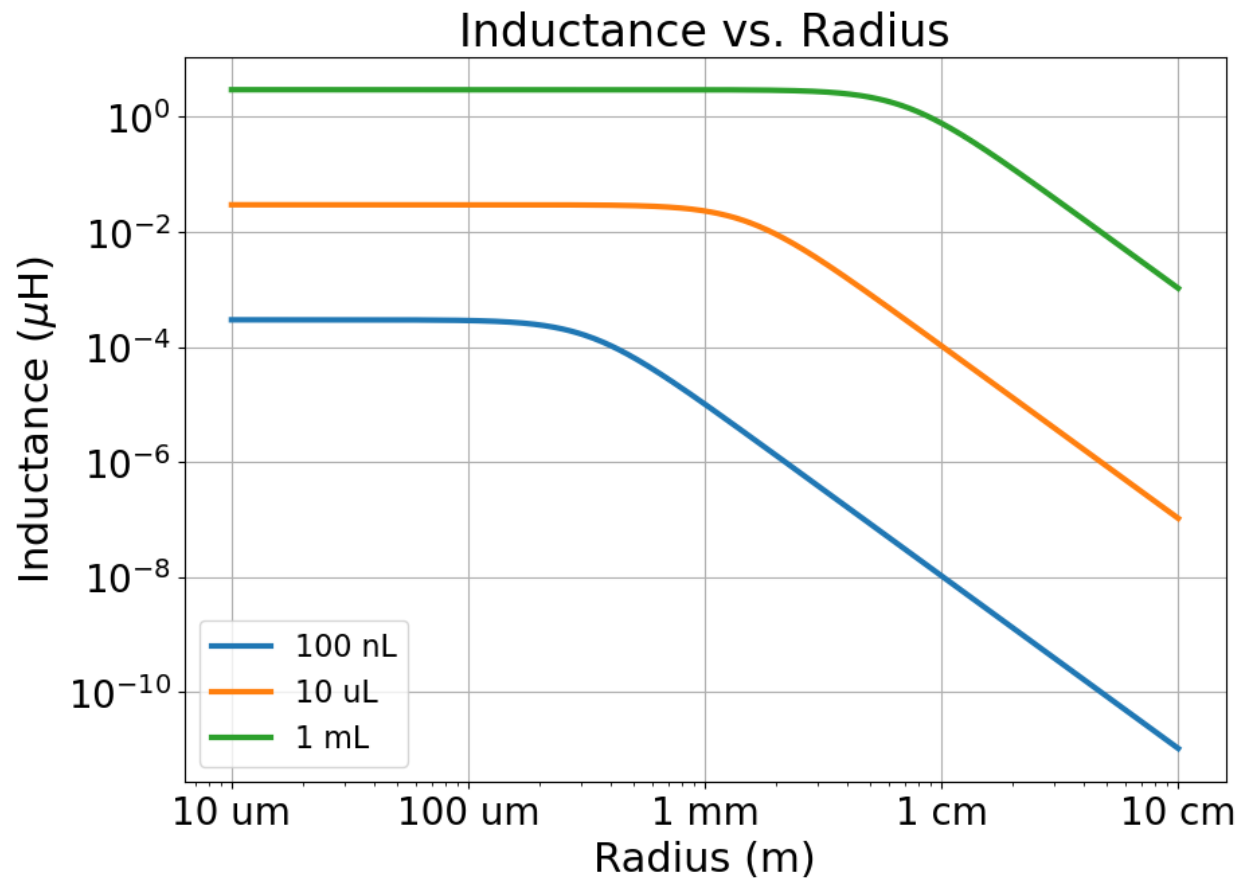


Figure 4.3: Decreasing radius shows an increase in coil inductance up until a certain point when the inductance is constant. This regime is when $r \ll \sqrt[3]{\frac{10V}{9\pi}}$. This is due to the long solenoid approximation where $r \ll \ell$ and the coil inductance no longer is strongly dependent on radius

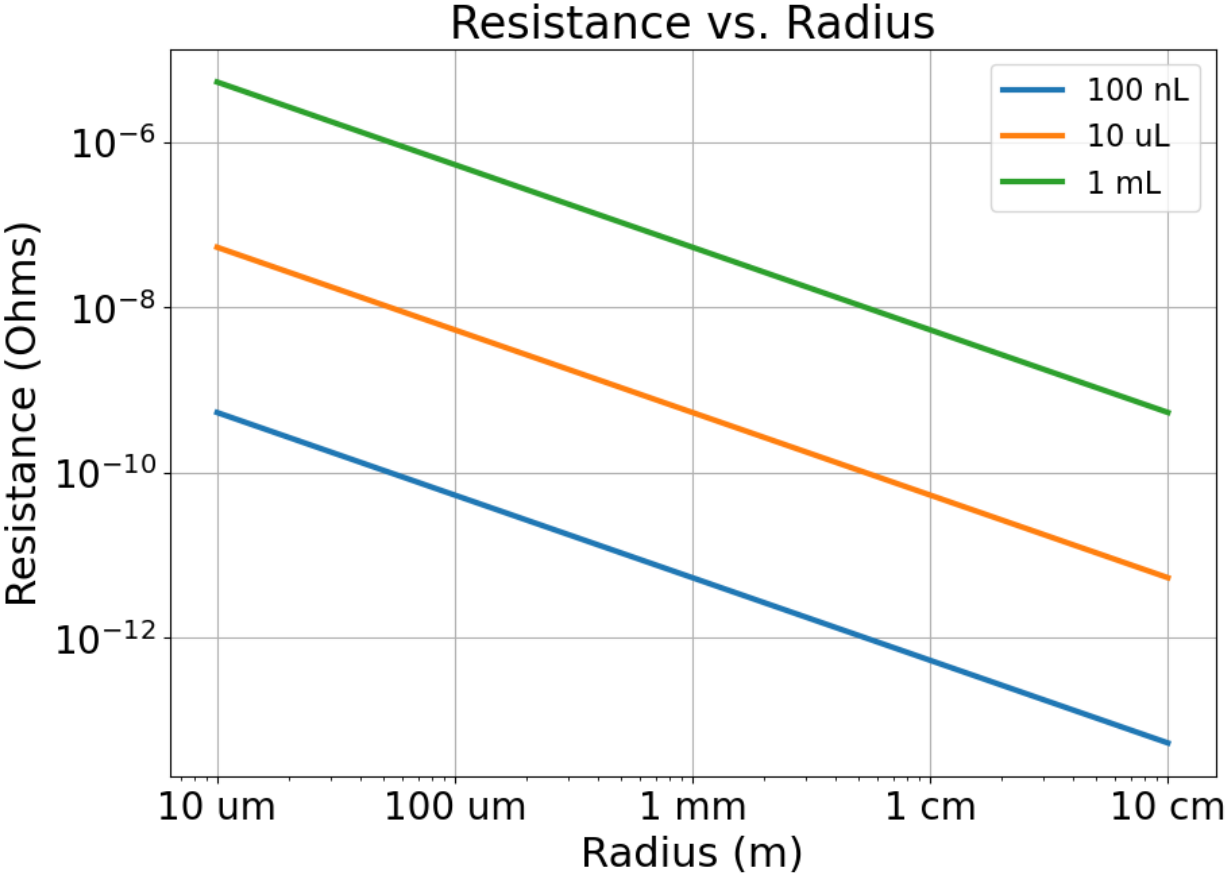


Figure 4.4: Coil resistance increases linearly with decreasing r .

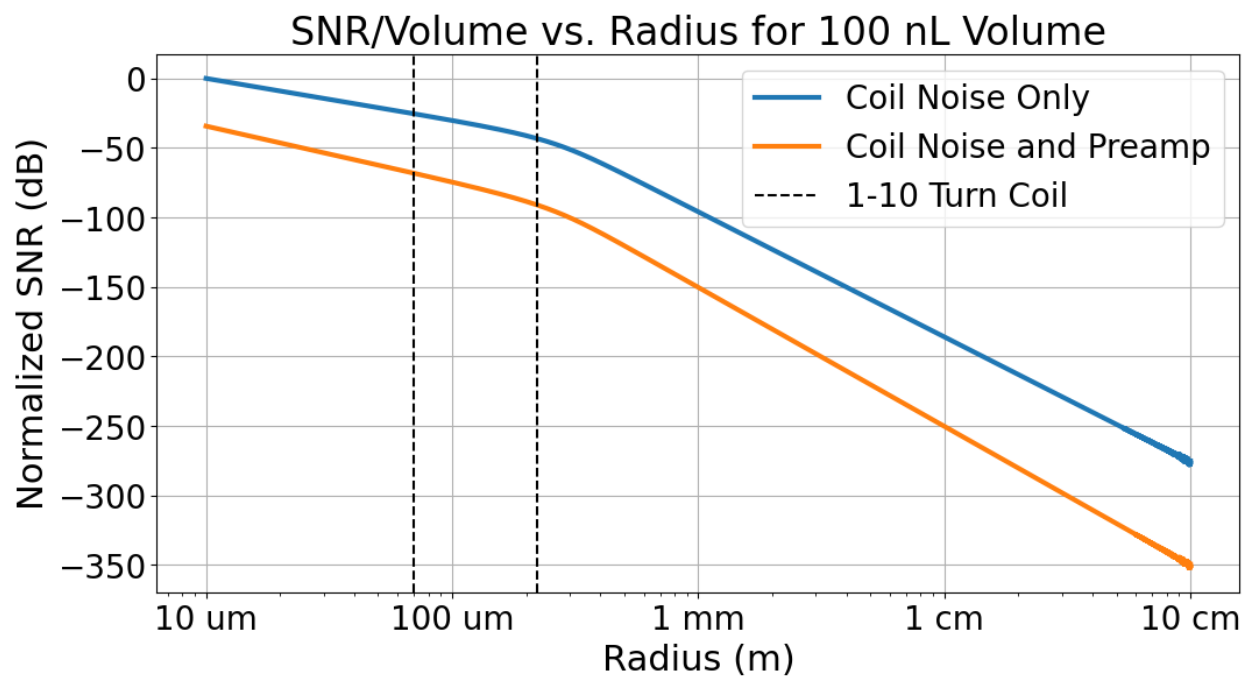


Figure 4.5: For 100 nL volume the SNR/volume shows a 40 dB/dec slope for $r < 300 \mu\text{m}$ for the coil and preamp model versus 30 dB/dec for the coil only model. This shows that the preamplifier noise is dominant in this model.

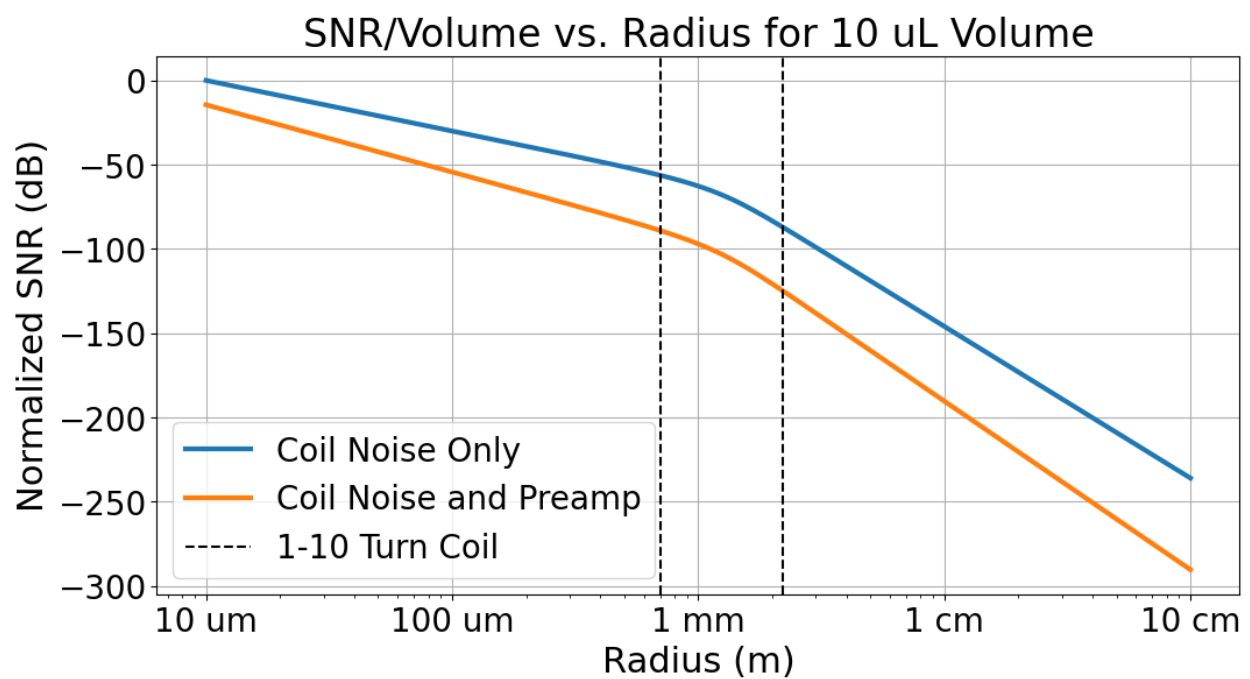


Figure 4.6: For 100 nL volume the SNR/volume shows a 40 dB/dec slope for $r < 1.5$ mm for the coil and preamp model versus 30 dB/dec for the coil only model. This shows that the preamplifier noise is still dominant in this model.

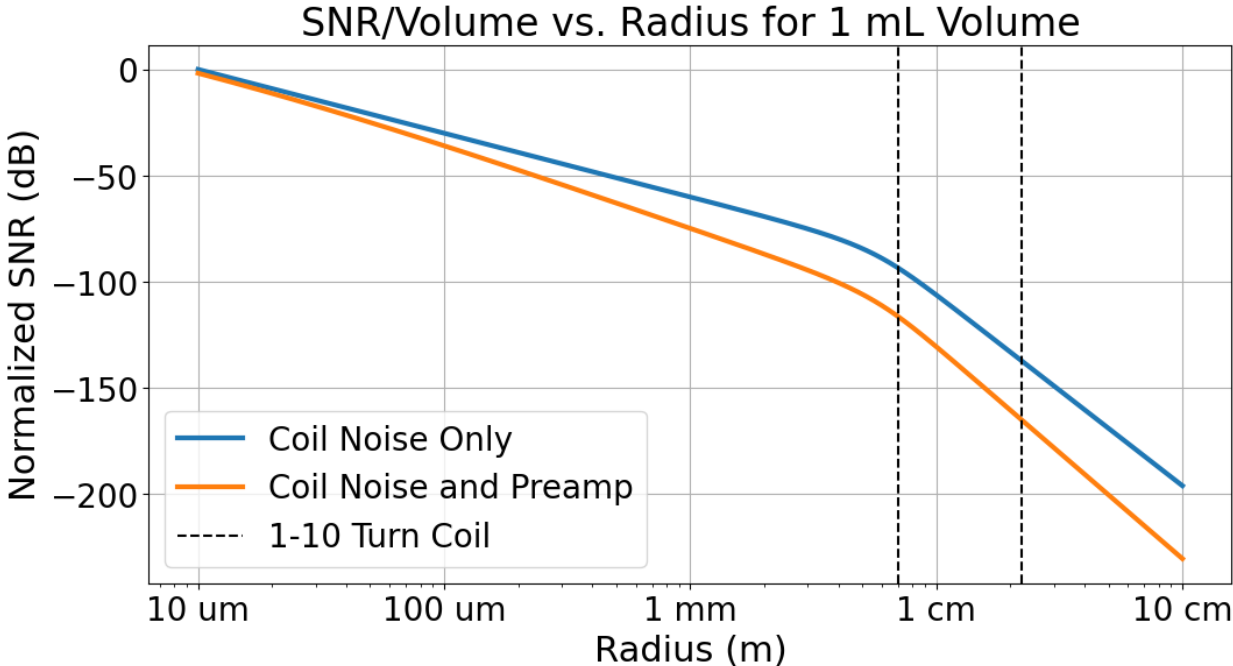


Figure 4.7: For 100 nL volume the SNR/volume shows a 40 dB/dec slope for $r < 4$ mm but tapers down to 30 dB/dec for the coil and preamp model versus 30 dB/dec for the coil only model. This shows that the preamplifier noise and coil noise have relatively equal contributions in this model.

4.4 Conclusion

In this work, a design methodology for optimized preamplifiers was introduced for benchtop particle relaxometer receiver coils for AWR/MPS applications. Using this methodology, we designed microcoils for different volumes of samples to get the best SNR per volume. Achieving higher SNR per volume for receiver coils is crucial to applications that require analysis of mass-limited or volume-limited sample solutions. As an example, we stand to gain a factor of 100 in SNR per volume in the 1 mL fixed volume case if we reduce a 5 mm receive coil radius to 500 microns. The trade off is a factor of 100 increase in the number of turns. This imposes another possible constraint which is construct-ability. This can be eased by perhaps going from 5 mm to 1.25 mm coil radius, only requiring a factor of 16 increase in the number of turns but only getting a factor of 16 increase in SNR. The trade-off is then number of turns with SNR for a preamplifier noise dominant case. However, an order of magnitude increase in SNR is exceptional and it is hard to find such an increase in performance through simple geometry changes.

Part II

Active and Passive Direct Feedthrough Suppression Improves Dynamic Range

Chapter 5

Direct Feedthrough Interference in Magnetic Particle Imaging

5.1 Overview

In this chapter, I discuss the direct feedthrough interference phenomenon in MPI starting from the underlying physics, how this interference affects the overall system, and ways to reduce the effect of this interference using passive and active cancellation. In Chapter 5, I discuss methods to design a more easily shimmable gradiometric cancellation coil for passive cancellation. In Chapter 7, I discuss a method to actively cancel broadband feedthrough using instrumentation amplifiers with a feedforward cancellation scheme.

5.2 Cause of Direct Feedthrough Interference

Magnetic particle excitation and detection requires a simultaneous transmit/receive system. MPI cannot use a T/R switch like MRI and wait for the relaxation signal. As a result, the applied field generated by the transmit coil can couple into the receive coil.

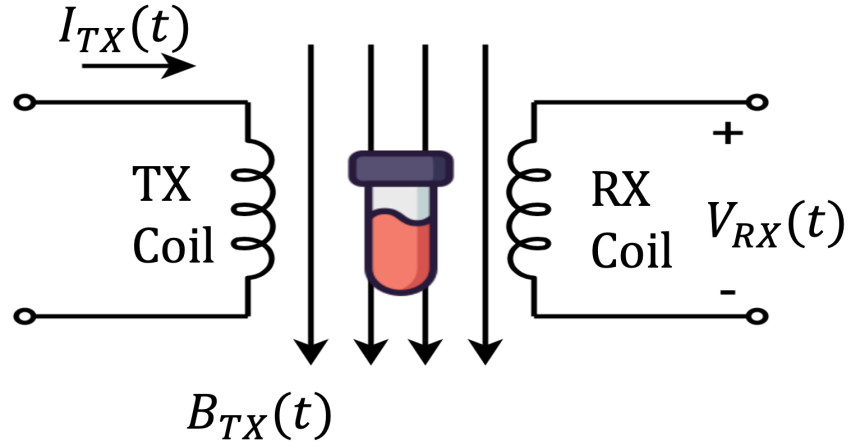


Figure 5.1: Excitation of particles requires simultaneous TX/RX

5.2.1 Transmit to Receive Inductive Coupling

Since the TX and RX coils are concentric, they are inductively coupled. Direct feedthrough is directly proportional to the mutual inductance of the TX/RX coil pairs which can be calculated by the Neumann formula for mutual inductance [57]

$$M = \frac{\mu_0}{4\pi} \oint_{C_{RX}} \int_{C_{TX}} \frac{dz_{TX} \cdot z_{RX}}{|z_{TX} - z_{RX}|} \quad (5.1)$$

Feedthrough can also be formulated as the voltage due to the change in flux due to the AC magnetic field created by the TX coil:

$$V_{ft}(t) = -\frac{d\Phi(t)}{dt} = -\frac{d}{dt} \iint_A \mathbf{B}_{TX}(t) \cdot d\mathbf{A}_{RX} \quad (5.2)$$

$$(5.3)$$

where \mathbf{B}_{TX} is the field vector generated by the TX coil and \mathbf{A}_{RX} is the cross sectional area vector of the RX coil.

5.2.2 Feedthrough Contaminates Signal

Feedthrough interference is generally undesired as it contaminates the MPI signal by up to 6 orders of magnitude. For sensitive applications such as cancer imaging or cell tracking, we want noise-limited detection at higher gain, not feedthrough interference-limited detection due to reduced dynamic range. Generally in preclinical MPI, works have noted that the reticuloendothelial system (RES) in subject mice experience a much higher SPIO uptake, whereas other areas where we wish to detect SPIOs have much lower amounts of SPIOs.

This necessitates the highest possible dynamic range to distinguish tumors from healthy cells in cancer imaging, and labelled white blood cells for immuno-imaging applications. This dynamic range is only available after cancelling residual direct feedthrough.

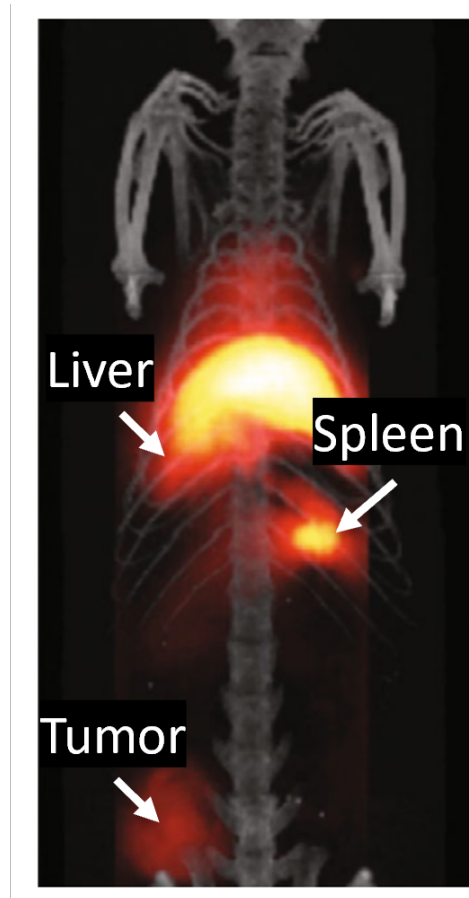


Figure 5.2: High dynamic range is needed to robustly image tumors in preclinical MPI cancer imaging, where the organs of the RES (liver and spleen) exhibit high particle uptake. Reduced feedthrough interference enables higher contrast-to-noise (CNR) imaging.

5.3 Direct Feedthrough Inteference Suppression Methods

Traditionally in MPI and MPS, a high-pass filter and tuned filter are applied to filter out the single tone direct feedthrough interference, which cannot be done for arbitrary waveform excitation. Passive feedthrough attenuation techniques include gradiometric coils [34] (which

this work discusses more in-depth), passive shimming with a second order gradiometer [58] or secondary finer mechanical shimming [59].

Active cancellation has been shown to further suppress direct feedthrough interference using a signal injection transformer [29], vector modulator [35], and lock-in amplifier [36]. These methods work very well in suppressing feedthrough at particular frequencies but there is still an open challenge to cancel out the feedthrough of an arbitrary excitation waveform or broadband cancellation.

5.3.1 Gradiometric Cancellation Coils

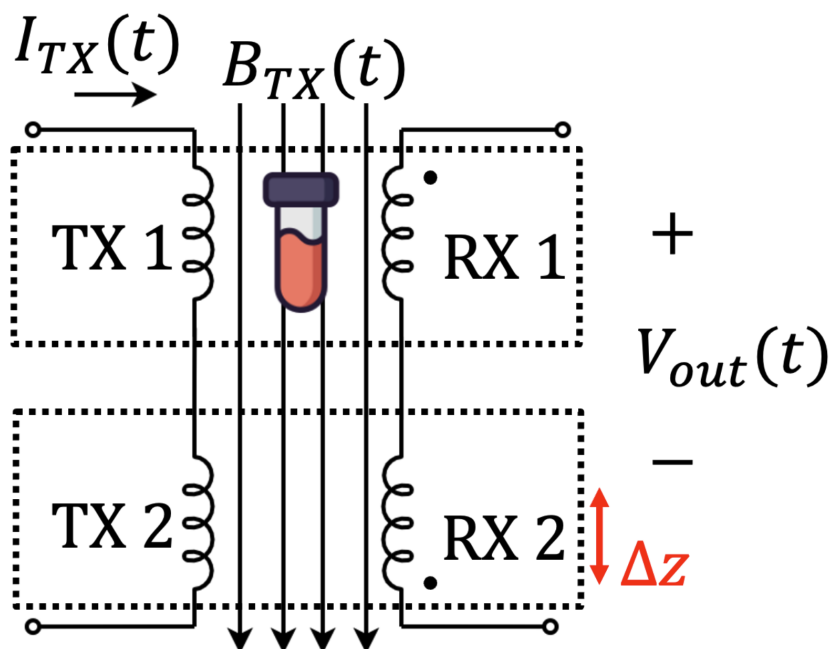


Figure 5.3: A gradiometer can be constructed by winding two coils in anti-series, where one coil is wound in the opposite direction of the other.

Gradiometric coils are two identical receive coils wound in anti-series (i.e., the coil windings are in opposite directions of each other as shown in Figure 5.3). Each receive coil experiences the same amount of change in flux due to the changing field generated by a corresponding transmit coil. The net change in flux is the difference of the two. If the two transmit and receive coil pairs are identical, then the net change in flux is ideally zero. Cancellation using gradiometric coils is a simple mechanism that can achieve excellent feedthrough rejection. However, this mechanism is highly sensitive to mechanical variations and requires precise mechanical shimming for adequate feedthrough suppression. The AWR uses a very

fine shimming system, which employs a cantilever and duplicated gradiometer receive coil (Figure 5.4). This mechanism currently achieves over 70 dB of direct feedthrough attenuation, shown in Figure 5.5. However, coils are sensitive in mechanical placement, with nearly 10 dB feedthrough attenuation per 50 μm near the ideal placement point [34]. In Chapter 6, I showcase an optimization method to design gradiometric coils that have more forgiving mechanical tolerance and are more easily shimmable.

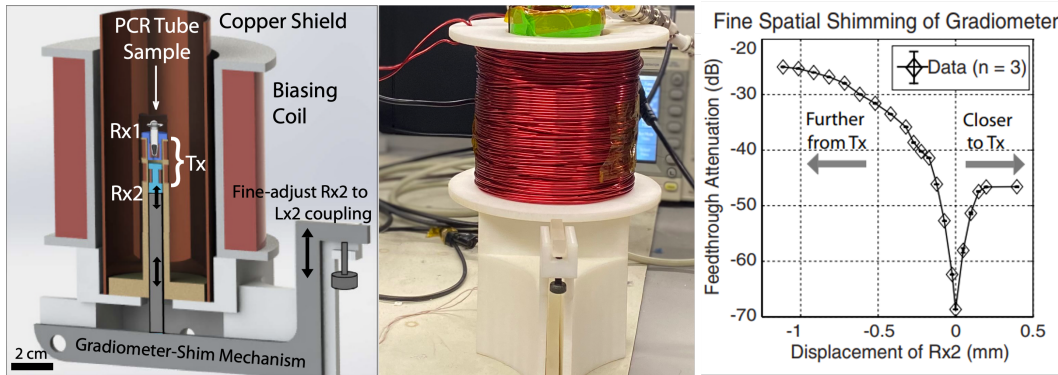


Figure 5.4: (Left) CAD model of the gradiometric cancellation coil shows the cantilever mechanism used to shim the relative distance between the receive coils. (Middle) Constructed gradiometric coil system as part of building the next generation Arbitrary Waveform Relaxometer. (Right) Coils are sensitive in mechanical placement, with nearly 10 dB feedthrough attenuation per 50 μm near the ideal placement point.

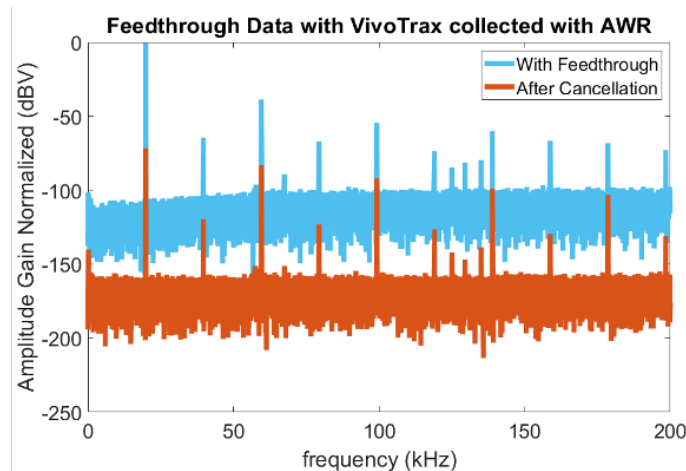


Figure 5.5: Constructed gradiometer for the next generation AWR achieves 71 dB attenuation of direct feedthrough.

Chapter 6

Design of Optimized Gradiometric Coils for Magnetic Suppression of Direct Feedthrough using Linear Programming

This work is adapted from the author’s first-author publication titled “Design of a more easily shimmable gradiometric coil using linear programming” which has been published in the International Journal on Magnetic Particle Imaging in 2022 [37].

6.1 Introduction

Magnetic particle imaging (MPI) is a tracer imaging modality that detects superparamagnetic iron oxide nanoparticles (SPIOs), enabling sensitive, radiation-free imaging of cells and disease pathologies. Tracer development and evaluation is crucial to optimizing MPI performance. The arbitrary waveform relaxometer (AWR) is an indispensable platform for developing magnetic nanoparticle tracers for magnetic particle imaging (MPI) applications. By characterizing the point spread function (PSF) of a specific magnetic nanoparticle, the AWR can evaluate the performance (e.g., SNR and spatial resolution) of the magnetic nanoparticle for MPI [34]. The design of wideband (DC-400 kHz) and arbitrary waveforms (up to 10 MHz) enables rapid optimization of pulse sequence design.

One of the biggest challenges in arbitrary waveform excitation is direct feedthrough interference due to the drive field, which is usually much larger than the signal from magnetic nanoparticles. The flux induced by the excitation coil couples into the receive coil, contaminating the magnetic particle signal. In MPI and conventional magnetic particle spectrometers (MPS), a high-pass filter and tuned filter are applied to filter out the single tone interference, which cannot be done for arbitrary waveform excitation. The AWR uses a very fine shimming system, which employs a cantilever and duplicated gradiometer receive coil.

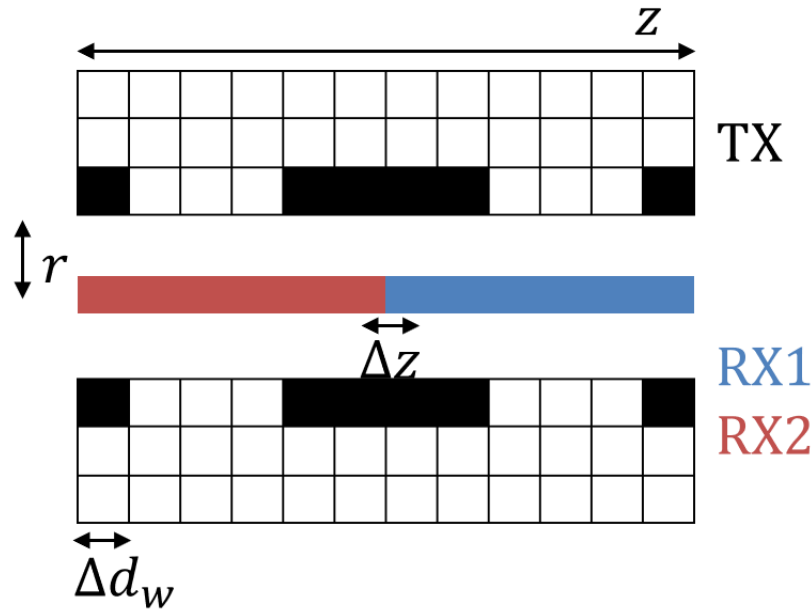


Figure 6.1: A possible solution for the wiring/current distribution of an optimal transmit coil design. The black filled in grids are windings and the rest is air. Blue and Red are locations of the receive coils relative to the transmit coil in the axial direction z .

This mechanism currently achieves over 60 dB of direct feedthrough attenuation, but is sensitive in mechanical placement, with nearly 10 dB feedthrough attenuation per 50 μm near the ideal placement point [34]. Other feedthrough attenuation techniques include passive shimming by applying a second order gradiometer [58], secondary finer mechanical shimming [59] and active compensation by feeding back the drive feedthrough signal [29].

A challenge in mechanical coil shimming of a gradiometer is that it is highly sensitive to spatial variations. This requires a shimming process that is done before each scan to ensure the highest possible feedthrough rejection. This work will show results for a design of an optimally shimmable excitation coil for a given gradiometric coil design using L_1 -norm minimization formulated as a linear programming (LP) problem. We wish to achieve a coil design similar to that of Figure 6.1. Linear programming is a power optimization tool that has been used to design RF and gradient coils for MRI [60], [61].

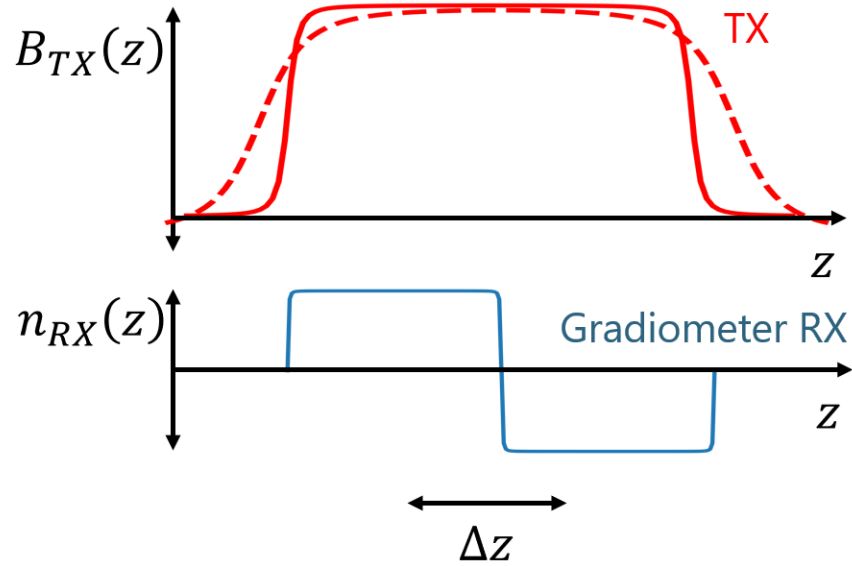


Figure 6.2: Illustration of transmit receive profiles with minimized mutual inductance. The standard transmit design (solid red) shows a sharp field profile that is by design orthogonal to the receiver coil in blue, thereby minimizing direct feedthrough interference. However winding imperfections are unavoidable and hence we must incorporate a worm gear to mechanically shim the receive coil at the magnetic center of the transmit coil. To improve prior designs, we hereby propose the dashed red transmit profile, which allows for zero mutual inductance shimming with very gradual mechanical precision. Like a vernier adjustment, this makes it far simpler to shim the coil and also keeps the zero mutual coupling more stable in response to normal building ambient vibrations.

6.2 Theory and Methods

6.2.1 Problem Formulation

To best understand how to optimize the mechanical tolerance of the transmit/receive (TX/RX) coil pairs, we must formulate direct feedthrough as a function of axial placement of the RX coils Δz . Feedthrough is directly proportional to the net mutual inductance of the TX/RX coil pairs which can be calculated by the Neumann formula for mutual inductance [29], [57]

$$M(\Delta z) = \frac{\mu_0}{4\pi} \left[\oint_{C_{RX1}} \int_{C_{TX}} \frac{d\mathbf{z}_{TX} \cdot \mathbf{z}_{RX1}}{|\mathbf{z}_{TX} - \mathbf{z}_{RX1}|} - \oint_{C_{RX2}} \int_{C_{TX}} \frac{d\mathbf{z}_{TX} \cdot \mathbf{z}_{RX2}}{|\mathbf{z}_{TX} - \mathbf{z}_{RX2}|} \right] \quad (6.1)$$

where $M(\Delta z)$ is the net mutual inductance of the transmit coil with the anti-series combination of the receive coil (RX1) and cancellation coil (RX2). Using the fact that mutual inductance is directly proportional to flux, we can relax Equation 6.1 into a more digestible

form by calculating the total flux of concentric solenoids with current loops $i_{tx}(r, z)$ illustrated in Figure 6.1, which are the values of the currents at radius r and axial location z . For our problem we assume the radius for the TX and RX coils are the same.

For a single winding of a transmit coil, the on-axis field generated per unit current is

$$\frac{B_{turn}(z)}{I} = \frac{\mu_0 r^2}{2(r^2 + z^2)^{\frac{3}{2}}} \quad (6.2)$$

from Biot-Savart law. The total flux can then be written as a dot product of the RX winding pattern coil area with the spatial convolution of the TX current loops with the field of a single turn:

$$M = \int \pi r^2 i_{rx}(z) \cdot \left(\frac{B_{turn}(z)}{I} * i_{tx}(z) \right) dz \quad (6.3)$$

where $i_{rx} = i_{rx1} - i_{rx2}$.

To formulate M as a function of axial placement of the RX coils Δz , we perform another spatial convolution with respect to the RX winding pattern:

$$M(\Delta z) = \int \pi r^2 i_{rx}(z - u) \cdot \left(\frac{B_{turn}(u)}{I} * i_{tx}(u) \right) du . \quad (6.4)$$

This formulation can be more easily understood as a series of convolutions, which are linear operations and represented as matrices. The current loops and winding patterns can be represented as vectors. The mutual inductance can therefore be represented as a resultant vector of the following matrix operations:

$$\mathbf{b}_{\mathbf{tx}}(\mathbf{i}_{\mathbf{tx}}) = C_{B_{turn}} \mathbf{i}_{\mathbf{tx}} \quad (6.5)$$

$$\mathbf{m}(\mathbf{i}_{\mathbf{tx}}) = C_{rx} C_{B_{turn}} \mathbf{i}_{\mathbf{tx}} \quad (6.6)$$

where $\mathbf{i}_{\mathbf{tx}}$ is a vector denoting the current loops spaced by Δd , and C_{rx} and $C_{B_{turn}}$ are convolution matrices for the RX winding patterns and the field of a single current loop, respectively. To design for a given mechanical tolerance of the coil, we impose a shimmability constraint ϵ_{dM} on the difference of the mutual inductance m for a symmetric displacement of $+z_{disp}$ and $-z_{disp}$ similar to how a field homogeneity constraint can be placed:

$$\left| \mathbf{m}(+z_{disp}) - \mathbf{m}(-z_{disp}) \right| \leq \epsilon_{dM} . \quad (6.7)$$

To ensure a symmetric design we must impose a constraint that the mutual inductance when the coils are placed in the ideal spot is close to zero ϵ_M and that the field at the symmetric displacements are the same as well:

$$\left| \mathbf{m}(z = 0) \right| \leq \epsilon_M ; \quad (6.8)$$

$$\mathbf{b}_{\mathbf{tx}}(+z_{disp}) = \mathbf{b}_{\mathbf{tx}}(-z_{disp}) . \quad (6.9)$$

To prevent a trivial solution, we must also impose a field strength constraint on the coil design:

$$\mathbf{b}_{\mathbf{tx}}(z = 0) \geq B_{min} . \quad (6.10)$$

We impose the mechanical tolerance as opposed to minimizing for it and instead minimize the sum of the absolute value of currents in the transmit coil subject to these constraints:

$$\begin{aligned} \text{Minimize: } & \sum |i_{tx,n}| \\ \text{Subject to: } & -\epsilon_{dM} \leq \mathbf{m}(+z_{disp}) - \mathbf{m}(z_{disp}) \leq \epsilon_{dM} \\ & -\epsilon_M \leq \mathbf{m}(z = 0) \leq \epsilon_M \\ & -\mathbf{b}_{\mathbf{tx}}(z = 0) \leq -B_{min} \\ & \mathbf{b}_{\mathbf{tx}}(+z_{disp}) = \mathbf{b}_{\mathbf{tx}}(-z_{disp}) . \end{aligned} \quad (6.11)$$

6.2.2 L_1 - Norm Optimization

Equation 6.11 is an L_1 -norm minimization problem which is a convex optimization problem. This formulation is powerful because it not only is tractable, but it promotes sparsity in the coil solution due to the L_1 -norm constraint. This means that the optimal coil will have very few windings while the shimmability constraint ϵ_{dM} is met. This problem can be reformulated into an LP problem by adding auxiliary variables t_1, \dots, t_N as follows:

$$\begin{aligned} \text{Minimize: } & \sum t_n \\ \text{Subject to: } & \text{same constraints as 6.11;} \\ & -t_n \leq i_{tx,n} \leq t_n \quad \forall n = 1, \dots, N . \end{aligned} \quad (6.12)$$

6.2.3 Formulation as an Integer Programming Minimum Sum Set Cover Problem

To simplify the design of the coil, we can also impose an integer constraint on the current loops:

$$|i_{tx,n}| \in \{0, 1\} . \quad (6.13)$$

Now the problem is an Integer Linear Programming (ILP) problem. Inherently the coil design optimization problem requires integer linear programming (ILP) to solve since the solution is a spatially discrete grid placement of the coil windings to generate the current loops. However, ILP problems are NP-hard and may take a long time to solve since they are less tractable [62]. IP problems can instead be relaxed to a regular LP problem by imposing continuous constraints instead of the integer constraints. The integer constraint $|i_{tx,n}| \in \{0, 1\}$ is then relaxed to $0 \leq |i_{tx,n}| \leq 1$. This LP problem can now be solved very efficiently with standard convex optimization software packages. For example, MATLAB's `lp()` function or Python's `linprog()` method with SciPy can efficiently generate an optimal solution to this LP. This work uses the SciPy `linprog()` method.

6.2.4 Final Form of the Optimization Problem

$$\begin{aligned}
& \text{Minimize: } \sum t_n \\
& \text{Subject to: } \left| \mathbf{m}(+z_{disp}) - \mathbf{m}(z_{disp}) \right| \leq (\epsilon_{dM} - \Delta \mathbf{m}_0) \\
& \quad \left| \mathbf{m}(z = 0) \right| \leq (\epsilon_M - \mathbf{m}_0) \\
& \quad -\mathbf{b}_{\mathbf{tx}}(z = 0) \leq -(B_{min} - B_0) \\
& \quad \mathbf{b}_{\mathbf{tx}}(+z_{disp}) = \mathbf{b}_{\mathbf{tx}}(-z_{disp}) \\
& \quad -t_n \leq i_{tx,n} \leq t_n \quad \forall n = 1, \dots, N \\
& \quad 0 \leq i_{tx,n} \leq 1 \quad \forall n = 1, \dots, N.
\end{aligned} \tag{6.14}$$

where \mathbf{m}_0 is the mutual inductance between the TX/RX coils due to the initial TX coil at $z = 0$, $\Delta \mathbf{m}_0$ is the change in mutual inductance due to a symmetric displacement in the initial TX coil, and B_0 is the maximum field generated due to the initial TX coil. The coil is designed at $r = r_{rx} + d_w$ to account as a layer on top of the RX coil.

6.2.5 Solution Quality of LP Solution vs. ILP Solution

If it so happens that the solution of the relaxed LP problem is all integers, then it will also be the optimal solution to the original ILP problem. This is not always true, as the result may include fractional values that point towards "partial" windings of the coil. In any case, the solution quality of the LP problem is as good as the solution of the IP problem, providing a lower bound for minimization problems. The "partial" winding issue can be reconciled in various ways. We can simply round the result of the windings to either 1 or 0 to enforce the original ILP constraints. This is the rounded result, which usually yields a slightly worse solution since the LP solution is the lower bound. We can also change the radii of the solution windings to simulate a partial winding (e.g., to roughly create a 0.5 winding, create a winding that is 2x the radius). This is the enhanced result, which yields a solution that is much closer in quality to the LP solution.

6.3 Results and Discussion

In this section we apply the LP design to a candidate TX/RX coil pair. For our problem, we define the radius $r = 5$ mm, the wire diameter $d_w = 0.5$ mm (100/44 served Litz Wire for reduced AC resistance), and $\Delta z = 500$ μ m. We define a 20-turn solenoid for the initial TX coil, a 10-turn RX1 coil, and a 10-turn RX2 (cancellation) coil, all tightly wound. The initial coil winding configuration is show in Figure 6.3.

We can immediately improve the shimmability of the gradiometric coils by separating the (+) and (-) halves of the anti-series pair by the optimal (anti-)Helmholtz coil spacing. The optimal spacing for circular coils is $d = r_{coil}$ [63].

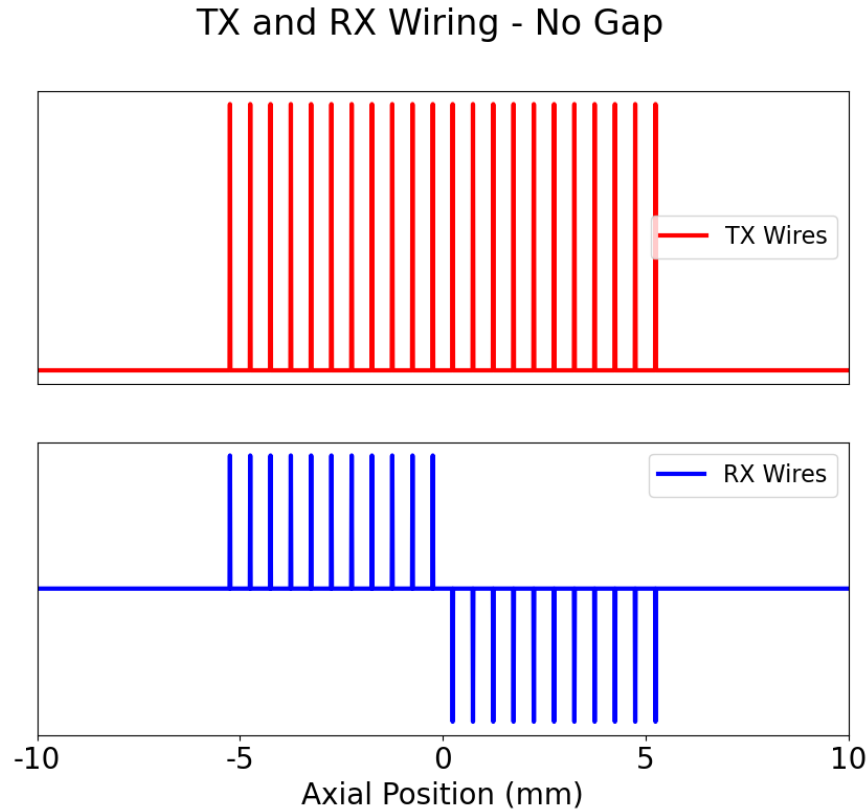


Figure 6.3: TX/RX Wiring of Initial Gradiometer Coil Pair with no gap between the pair.

Because of the sparsity of the solution, it is helpful to bootstrap this optimization problem by superimposing the solution onto an existing solenoid coil design. The modified optimization problem then only has to account for the bootstrapped TX coil. We impose a more forgiving mechanical tolerance constraint of less than 60 dB direct feedthrough rejection from $-250\ \mu\text{m}$ to $250\ \mu\text{m}$ displacement of the RX coils relative to the TX coils. This 0.5 mm of mechanical tolerance allows for more coarse shimming of the gradiometer without the need of a super fine screw or tuning mechanism. Comparing the three coil pair configurations show that the LP designed coil is the most "shimmable", meaning it has the most mechanical tolerance in reaching the desired feedthrough decoupling.

We now have to handle the partial windings offered by the LP solution. Comparing both the rounded ILP solution and enhanced ILP solution to the LP solution shows that the enhanced solution is only slightly worse than the best case LP solution and still meets the 60 dB over $500\ \mu\text{m}$ shimming distance requirement.

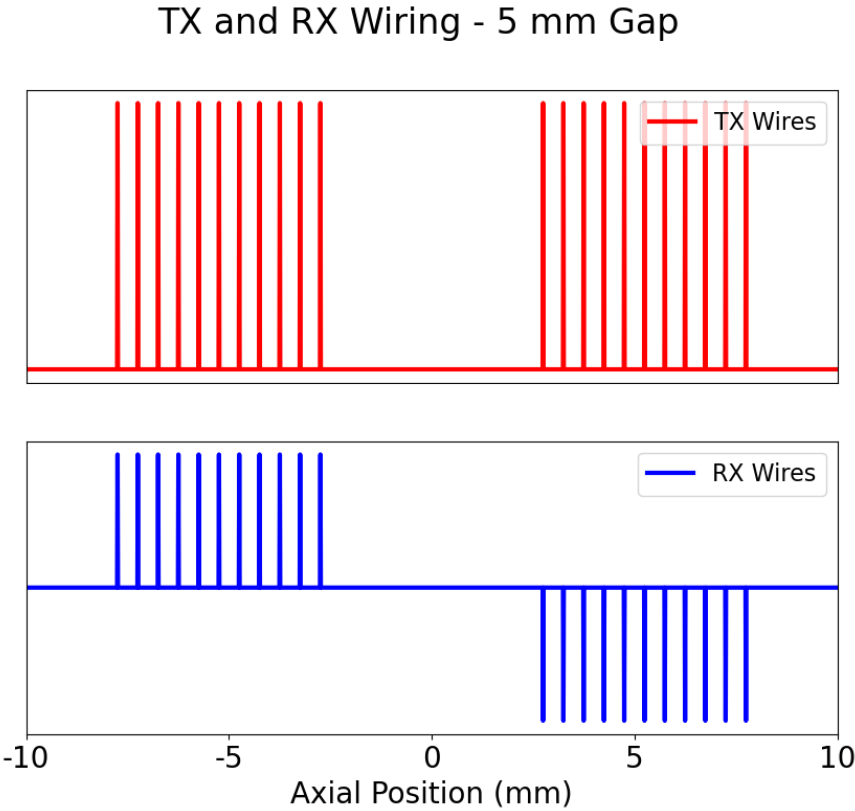


Figure 6.4: TX/RX Wiring of Initial Gradiometer Coil Pair with a gap equal to the radius of the coils between the pair.

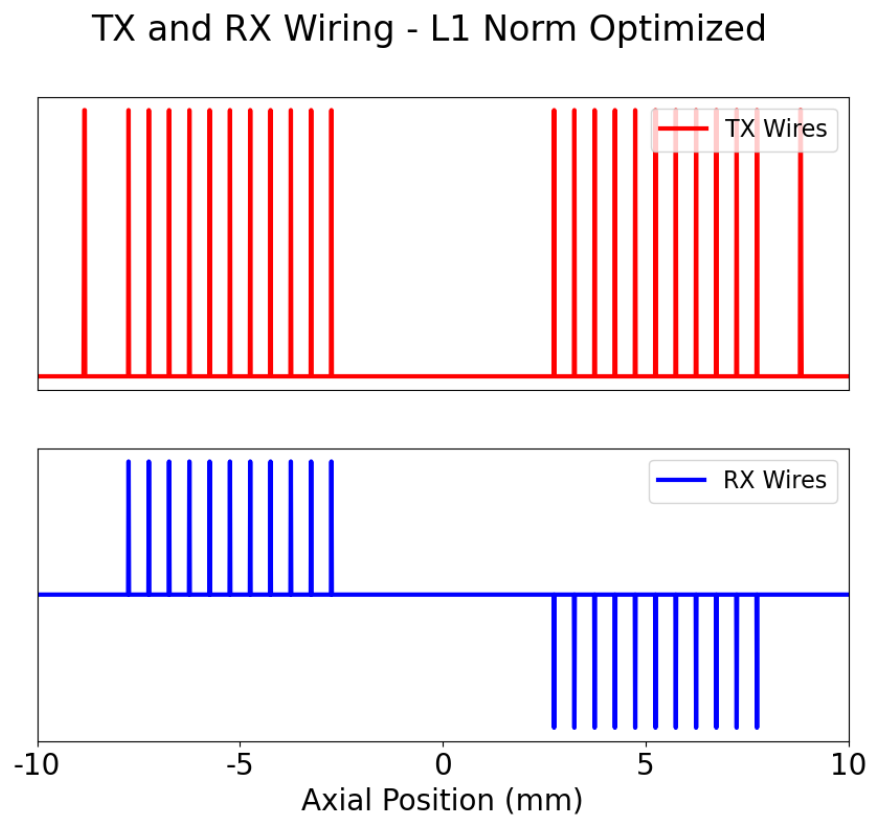


Figure 6.5: TX/RX Wiring Solution given by the Linear Program. The LP provided a solution that adds a few extra winding towards the edges of the coil. Not seen are the partial windings also offered by the solution.

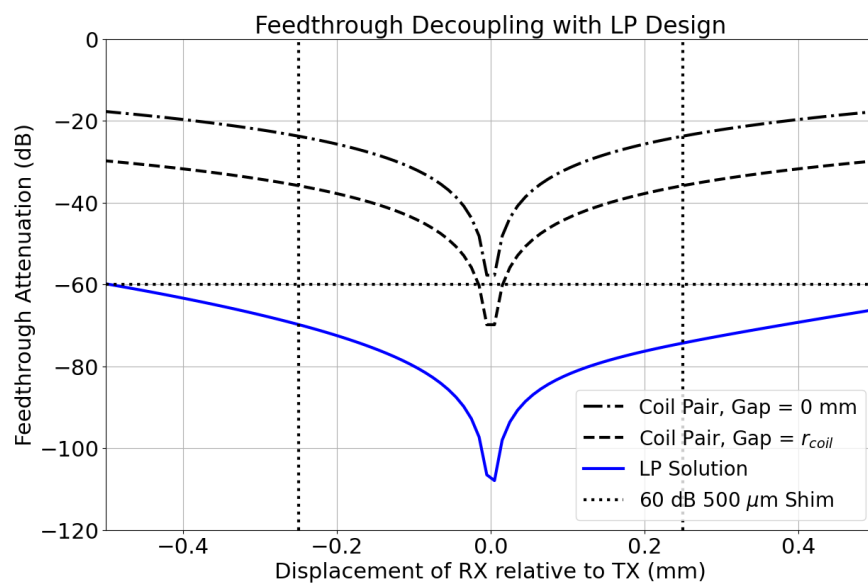


Figure 6.6: All coil configurations show that the best feedthrough rejection occurs when the coil pair is aligned with each other. The anti-Helmholtz coil pair with the gap equal to the coil radius shows better mechanical tolerance than the no-gap pair but still fails to meet the tolerance constraint. The Linear Program solution meets the 60 dB rejection constraint over 500 μm shimming distance whereas the other coil configurations require fare greater dexterity within 20 μm .

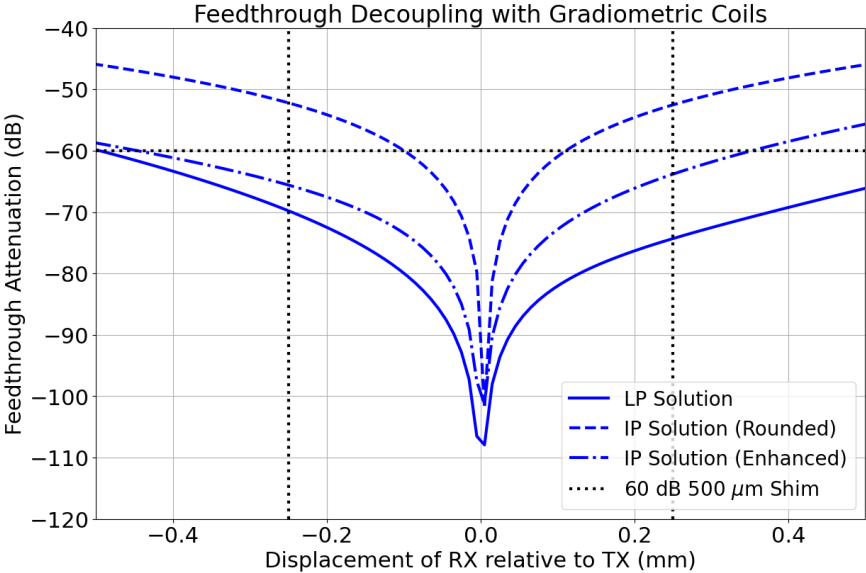


Figure 6.7: The rounded ILP solution no longer meets the original constraints of the relaxed LP while the enhanced solution created by partial windings is only slightly worse than the best case LP solution and still meets the 60 dB over 500 μm shimming distance requirement

6.4 Discussion and Conclusion

This excitation coil design procedure is promising for applications where direct feedthrough mitigation is important, generating a minimal power solution for a given mechanical tolerance and field constraint. However, this procedure assumes perfect placement of wires according to the solution grid and does not account for winding errors or partial windings in the construction of the coil itself. This is the very first transmit-receive design procedure that allows for practical shimming precision. Our preliminary *in silico* designs show an superb 60 dB direct feedthrough cancellation with a very practical 500 microns tolerance in the shimming position. Our prior AWR shimming design required better than **50 microns tolerance** to achieve the same direct feedthrough suppression. The author can attest that that level of painstaking shimming is slow and extremely frustrating. I should note that the extra turns on the transmit coil do cost a small percentage of transmit power efficiency. However, the transmit power amplifiers used to drive current into the TX coils are typically 1 kW that usually requires a 1-4 ohm series load resistor to keep the amplifier's output within the safe operation area, so this is not a serious trade-off. Because we do not alter the receive coil, there is no loss of SNR. This procedure is very promising for experimental demonstration. It will be exciting to see if a real-world experimental demonstration can achieve 60 dB direct feedthrough suppression with 500 microns tolerance, using real-world coils, which have unavoidable winding errors and partial turns.

Chapter 7

Active Feedforward Cancellation of Feedthrough Interference with Automated Phase Correction

This work is adapted from the author’s manuscript for (at the time of writing this dissertation) pre-print publication titled ”Broadband Untuned Active Cancellation and Phase Correction of Direct Feedthrough Interference Enables 100-fold Improved Magnetic Particle Imaging Detection” which has been successfully submitted online in 2023 and is presently being given full consideration for publication in the IEEE Transactions on Biomedical Circuits and Systems [64].

7.1 Introduction

Magnetic particle imaging (MPI) is a tracer imaging modality that detects the strong change in magnetization of superparamagnetic iron oxide nanoparticles (SPIOs), enabling sensitive, radiation-free imaging of cells and disease pathologies [1], [65]. Smaller benchtop magnetic particle sensing systems have proven to be crucial in the development and characterization of particle tracers for novel biosensing applications and point-of-care devices. Several groups have developed benchtop magnetic particle detection systems in the form of magnetic particle spectrometers, relaxometers, differential magnetometers, and quantifiers [28], [38], [66]–[83]. The arbitrary waveform relaxometer (AWR) is one platform for developing magnetic nanoparticle tracers for magnetic particle imaging (MPI) applications [34]. By characterizing the point spread function (PSF) of a specific magnetic nanoparticle, the AWR can evaluate the performance (e.g. SNR and spatial resolution) of the magnetic nanoparticle for MPI [34]. The design of wideband (DC-400 kHz) and arbitrary waveforms enables rapid optimization of pulse sequence design and characterization of MPI tracers [48].

MPI has promising applications in cancer imaging, gut-bleed imaging, stem cell tracking, and white blood cell tracking [2], [4], [31], [33]. Signal-to-Noise Ratio (SNR), Resolution,

and Contrast are the biggest challenges in any imaging method. SNR is primarily effected by front end noise matching [27] and direct feedthrough challenges [29], [34]–[38]. New MPI Tracers are crucial to optimizing MPI resolution and SNR per picogram of iron.

MPI has already demonstrated robust systemic tracking of SPIO-labeled cells with a detection limit of 100s of cells in a preclinical scanner [31], [32], [39]–[41]. The detection sensitivity of MPI is soon approaching that of nuclear medicine techniques, making it useful for future clinical applications in cancer imaging, stroke diagnosis and staging, and cell therapy tracking [27]. However, too low of a receive gain prevents robust detection of small amounts of SPIO-labelled cells at full scale range. Literature has shown that labelling efficiency of SPIO-labelled cells vary widely from 1-100 pg Fe/cell [32], [42]–[47]. It is crucial that MPI has a large dynamic range capable of detecting trace amounts of labelled cells. In this work we aim to provide a solution for a common challenge in MPI and MPS, direct feedthrough interference.

7.2 Theory

7.2.1 Motivation

One of the biggest challenges in arbitrary waveform excitation is direct feedthrough interference. To induce a signal from the SPIOs, we apply an external magnetic field with an excitation or transmit (TX) coil. The particles align with the applied field and the change in magnetization induces a voltage signal in a receive (RX) coil proportional to the concentration of particles [1], [21]. However, the change in flux induced by the TX coil mutually couples into the RX coil and contaminates the magnetic particle signal in the form of the derivative of the TX field (Fig. 7.1).

$$V_{RX}(t) = V_{spio}(t) + V_{ft}(t) \tag{7.1}$$

$$V_{ft}(t) = -\frac{d\Phi(t)}{dt} = -\frac{d}{dt} \iint_A \mathbf{B}_{TX}(t) \cdot d\mathbf{A}_{RX} \tag{7.2}$$

$$V_{spio}(t) \ll V_{ft}(t) \tag{7.3}$$

where $\mathbf{B}_{TX}(t)$ is the magnetic field generated by the TX coil and \mathbf{A} is the total surface in the RX coil over which the change in magnetic flux is calculated.

This interference is often several orders of magnitude larger than the SPIO signal. Digital subtraction can be done to remove the interference, but the minimum detectable amount of SPIO is determined by the highest gain of the receive system that does not saturate the frontend due to the feedthrough, or where the signal-to-interference ratio (SIR) is 1. This is the feedthrough-limited limit-of-detection (LOD). The limit of detection should be due to the thermal noise of the system, or signal-to-noise ratio (SNR) limited.

Traditionally in MPI and conventional magnetic particle spectrometers (MPS), a high-pass filter and tuned filter are applied to filter out the single tone direct feedthrough interference, which cannot be done for arbitrary waveform excitation. The AWR instead uses a very

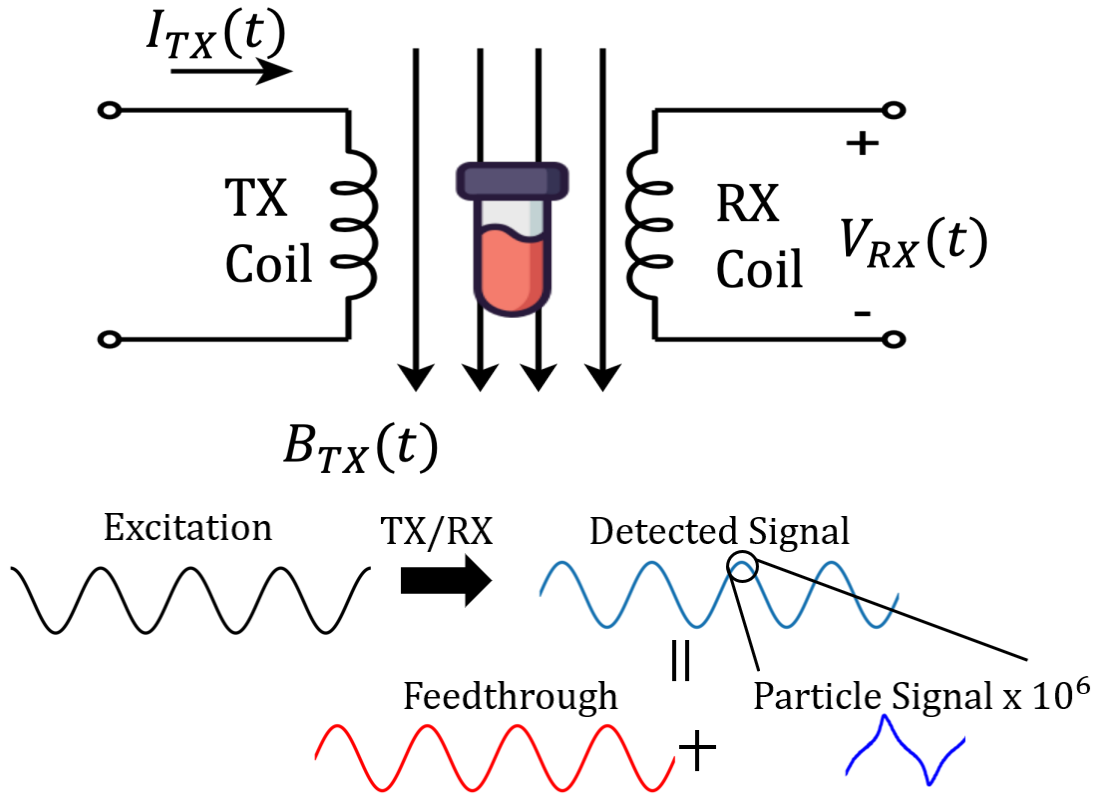


Figure 7.1: Particle Excitation creates direct feedthrough interference. A transmit coil is driven with a current waveform which generates the excitation field. The detected signal is a combination of both the nanoparticle signal and induced voltage from the transmit to receive coil coupling. This feedthrough interference is much larger than the particle signal.

fine shimming system, which employs a cantilever and duplicated gradiometer receive coil. This mechanism currently achieves over 60 dB of direct feedthrough attenuation. However, coils are sensitive in mechanical placement, with nearly 10 dB feedthrough attenuation per 50 μm near the ideal placement point [34]. Other passive feedthrough attenuation techniques include passive shimming with a second order gradiometer [58] or secondary finer mechanical shimming [59].

A challenge in mechanical coil shimming of a gradiometer is its high sensitivity to spatial variations. This requires a shimming process that is done before each scan to ensure the highest possible feedthrough rejection. Previous work has shown a design of an optimally shimmable excitation coil for a given gradiometric coil design using L_1 -norm minimization formulated as a linear programming problem [37].

Active cancellation has been shown to further suppress direct feedthrough interference using a signal injection transformer [29], vector modulator [35], and lock-in amplifier [36].

These methods work very well in suppressing feedthrough at particular frequencies but there is still an open challenge to cancel out the feedthrough of an arbitrary excitation waveform.

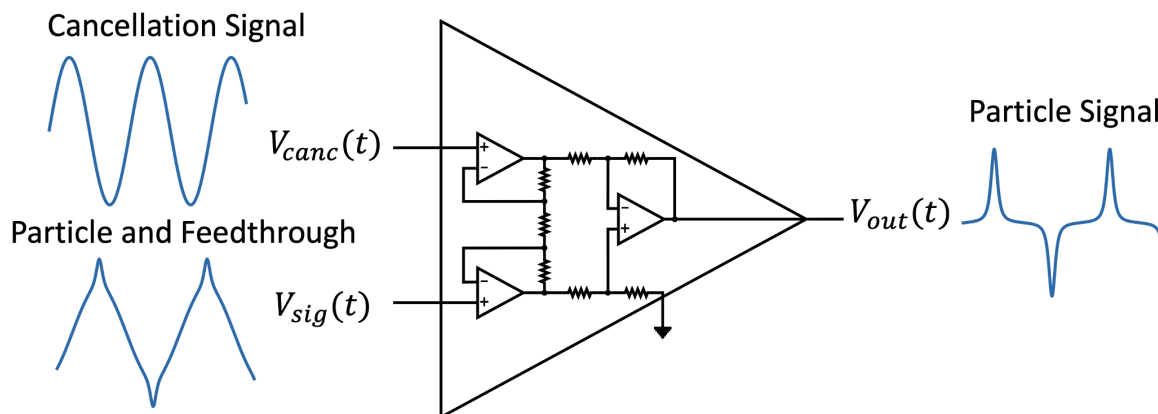


Figure 7.2: The instrumentation amplifier can cancel signals common to both inputs. If the direct feedthrough can be captured, generated as a cancellation signal, and fed into the other input, then the difference amplifier can output the difference $V_{out}(t) = V_{sig}(t) - V_{canc}(t) = V_{spio}(t) + V_{ft}(t) - V_{ft}(t) = V_{spio}(t)$ allowing us to capture just the particle signal.

In this work we will present an instrumentation amplifier (in-amp) based active cancellation scheme to suppress feedthrough interference of arbitrary excitation waveforms and enable an order of magnitude higher dynamic range over a wide excitation bandwidth (DC-400 kHz). This higher dynamic range allows the detection of much smaller masses of iron oxide nanoparticles.

7.2.2 Common Mode Rejection in Instrumentation Amplifiers

The instrumentation amplifier is a classic composite amplifier topology used to measure differential signals (Fig. 7.2). The main advantage of an in-amp is very high common-mode rejection (CMR). The CMR of an amplifier is its ability to amplify the difference of the voltage inputs while rejecting the common signal.

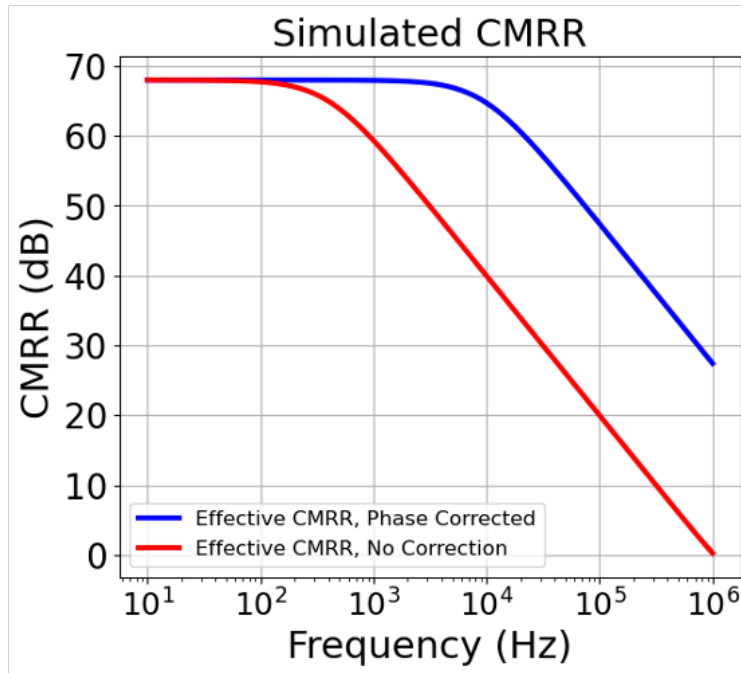


Figure 7.3: Using the data sheet of the AD8429 instrumentation amplifier, we simulated in LTspice the effective CMRR against frequency, CMRR against phase error at different DAC resolutions, and CMRR against DAC sampling rate. Phase error correction was also factored in. Simulation results show that CMRR falls off with frequency, but can be improved with phase correction.

7.2.3 Feedthrough Cancellation with Instrumentation Amplifier

We can utilize the in-amp's CMR to cancel the direct feedthrough interference as follows. We write the signal from the RX coil as $V_{rx}(t) = V_{spio}(t) + V_{ft}(t)$ where V_{spio} is the desired SPIO particle signal and V_{ft} is the direct feedthrough interference. We construct a cancellation signal $V_{canc} = V_{ft}$ from a Digital-to-Analog Converter (DAC) and use the CMR of an in-amp to reject V_{ft} and isolate just V_{spio} . The output should then be $V_{out}(t) = A_{dm}V_{spio}(t) + A_{cm}[V_{ft}(t)]$ where A_{dm} is the differential mode gain and A_{cm} is the common mode gain. For $A_{dm} = 1$, we can write the output as $V_{out}(t) = V_{spio}(t) + \frac{1}{CMR}[V_{ft}(t)]$ where $CMR = \frac{A_{dm}}{A_{cm}}$.

7.2.4 Non-idealities in Cancellation

There are a few non-idealities to consider when using an instrumentation amplifier to cancel out a signal.

1. The first is that CMR is finite and frequency dependent, resulting in residual common-mode at the output.

2. The second is quantization error ϵ due to the DAC generating the cancellation signal V_{canc} . The root-mean-squared error is $\sigma_{DAC} = \frac{LSB}{\sqrt{12}} = \frac{FSR/2^{n+1}}{\sqrt{12}}$ where FSR is the full scale voltage range, and n is the resolution in number of bits of the DAC.
3. The final non-ideality is phase error between the feedthrough signal V_{ft} and the cancellation signal V_{canc} . Suppose there is some delay t_d in generating V_{canc} relative to V_{ft} due to digital timing signal differences, signal propagation path differences, and the finite time sampling of the DAC. The output voltage would be $V_{out}(t) = A_{dm}(V_{ft}(t) - V_{ft}(t - t_d)) + A_{cm}V_{ft}(t)$. Because the feedthrough is periodic, we represent the voltages as analytic signals with amplitude V_{ft} and frequency ω to simplify analysis: $V_{ft}(t) = V_{ft} \cos(\omega t)$ and $V_{canc}(t) = V_{ft} \cos(\omega t - \phi)$ where $\phi = \omega t_d$ is the phase offset.

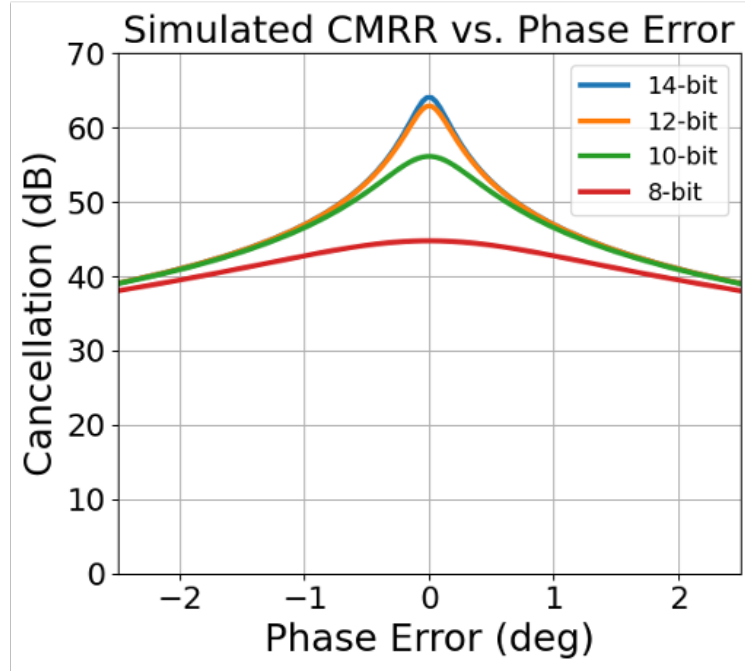


Figure 7.4: Simulation results suggest that any resolution DAC above 8 bits provides acceptable cancellation, but there are diminishing returns after 12 bits.

We derive the effective CMR of an in-amp based cancellation that includes the non-idealities mentioned above.

$$\frac{1}{CMR_{\text{eff}}} = \sqrt{\frac{1}{CMR^2} + \frac{\epsilon^2}{V_{ft,rms}^2} + \frac{(2CMR^2 + 2)(1 - \cos \phi)}{CMR^2}} \quad (7.4)$$

where the first, second, and third terms of the radicand correspond to the respective non-ideality. This equation is derived in the appendix and used to determine theoretical cancellation performances for Figs. 7.3, 7.4, 7.5, and 7.8.

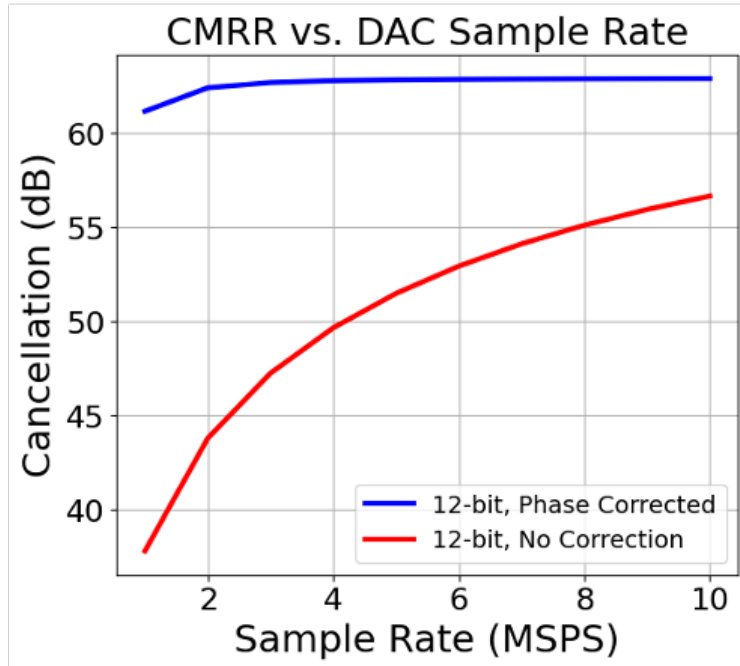


Figure 7.5: Simulation results show that cancellation is highly dependent on DAC sample rate, unless phase correction is applied, in which case there are diminishing returns after 2 MSPS.

7.3 Methods

7.3.1 Design of the Cancellation Circuit

Our receive system consists of a receive (RX) coil, low-noise amplifier (LNA), and analog-to-digital converter (ADC). The RX coil is a solenoid with a resistance $R = 0.3\ \Omega$ and inductance $L = 3\ \mu\text{H}$. The LNA used in our receive system is the SR560 (Stanford Research Systems, Sunnyvale, CA), which has a voltage noise density of $e_n = 4\ \text{nV}/\sqrt{\text{Hz}}$, user set gain of $G = 1000$, and analog bandwidth of 1 MHz. The ADC used is part of the PCI-6115 (National Instruments, Austin, TX) Data Acquisition (DAQ) Module with a full scale range of $\pm 20\ \text{V}$, 12-bit resolution, and 10 MSPS sampling rate. With this system we expect a total receive root-mean-square noise of $\sigma_{n,\text{theory}} = 5.2\ \text{mV}_{\text{rms}}$ using equivalent noise bandwidth $\text{ENBW} = \frac{\pi}{2}BW$, approximating the preamplifier’s frequency response as a first order low pass filter [51].

Table 7.1: Instrumentation Amplifier Specifications

Specification	Required	AD8429 + PCI-6115
CMRR	≥ 20 dB	35.4 dB
Bandwidth	≥ 10 MHz	15 MHz
Noise Density	≤ 400 nV/ $\sqrt{\text{Hz}}$	45 nV/ $\sqrt{\text{Hz}}$
DAC Resolution	≥ 8 bits	12 bits
DAC Sample Rate	≥ 2 MSPS	2.5 MSPS

We select a commercial in-amp that meets the required CMR as well as our receive chain specifications, namely bandwidth and noise density. We need at least 20 dB rejection throughout the 400 kHz transmit bandwidth. The gain-bandwidth should be greater than 10 times that of the preamp stage to preserve the signal bandwidth. The noise contribution should be less than 1/10th of the preamp’s output noise to preserve signal-to-noise ratio (SNR). The instrumentation amplifier used in this work is the AD8429 (Analog Devices Inc., Wilmington, MA). With the AD8429, CMRR was simulated factoring in the non-idealities in (7.4) to determine the DAC requirements needed to achieve cancellation (Figs. 7.4 and 7.5). Simulation was done using LTSpice (Analog Devices Inc., Wilmington, MA). The simulation results also illustrated the drastic effect phase error has on cancellation, demonstrating the need for a phase correction scheme. The DAC used is part of the PCI-6115, with a full scale range of ± 20 V, 12-bit resolution, and 2.5 MSPS sampling rate. As shown in Table 7.1, this amplifier and DAC meet every requirement.

7.3.2 Phase Error Detection and Correction

Fig. (7.6) illustrates the phase error detection and correction process. We detect and correct the phase error as follows.

1. Acquire the direct feedthrough $V_{ft}(t)$ with $V_{canc}(t) = 0$.
2. Play back $V_{ft}(t)$ as $V_{canc}(t)$ with $V_{sig}(t) = 0$.
3. Detect the phase error/time delay t_d using Fast-Fourier Transform (FFT) Cross Correlation.
4. Correct the phase by multiplying $V_{canc}(\omega)$ with $e^{j\omega t_d}$
5. Isolate the particle signal by playing the adjusted $V_{canc}(t)$ while $V_{sig}(t) = V_{spio}(t) + V_{ft}(t)$.

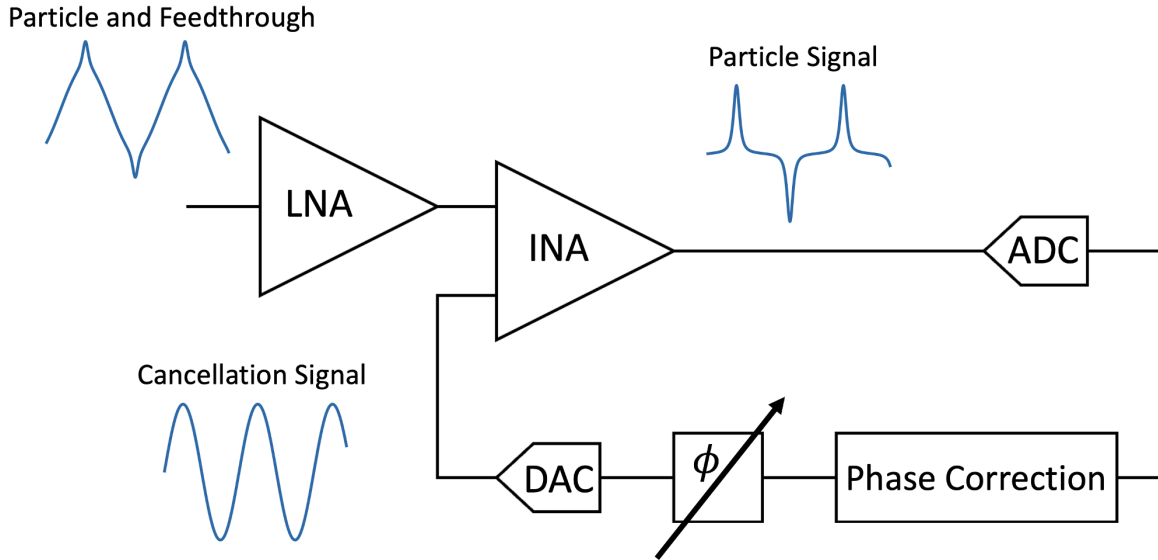


Figure 7.6: The complete receive system architecture is shown as follows. The receive coil picks up the desired particle signal and undesired feedthrough. Both components are amplified by the LNA. The instrumentation amplifier (IA) takes the generated cancellation signal and subtracts it from the LNA’s output, resulting in only the desired particle signal going into the ADC.

7.3.2.1 Phase Error Detection Procedure

Cross-correlation can be used for time delay estimation. For a time-delayed signal $y(t) = x(t - t_d)$, $r(t)$ has a peak at $t = t_d$. This result is used to estimate the time-delay. In the time domain the smallest detectable difference is the ADC sampling period T_s . For our 10 MSPS ADC, this is 100 ns, which is not fine enough. However, cross-correlation in the frequency domain can provide higher resolution. Since convolution in the time domain is multiplication in the frequency domain, $r(t) = x(t) * y(-t) \xleftrightarrow{\mathcal{F}} R(\omega) = X(\omega) \cdot Y^*(\omega)$. For $y(t) = x(t - t_d)$, $R(\omega) = |X(\omega)|^2 e^{j\omega t_d}$.

Since $|X(\omega)|^2$ is purely real, we can determine t_d by taking the phase of $R(\omega)$, resulting in $t_d = \frac{\angle R(\omega)}{\omega} = \frac{X(\omega) \cdot Y^*(\omega)}{\omega}$.

7.3.2.2 Phase Error Correction Procedure

We correct for the previously determined phase error/time-delay offset in the frequency domain. For our 2.5 MSPS DAC, time domain shifting cannot resolve time differences less

than 400 nanoseconds.

$$y_{adj}(t) = y(t + t_d) \xleftrightarrow{\mathcal{F}} Y_{adj}(\omega) = Y(\omega)e^{j\omega t_d} \quad (7.5)$$

Applying this phase correction significantly improves cancellation over a wider range of frequencies (Fig. 7.3).

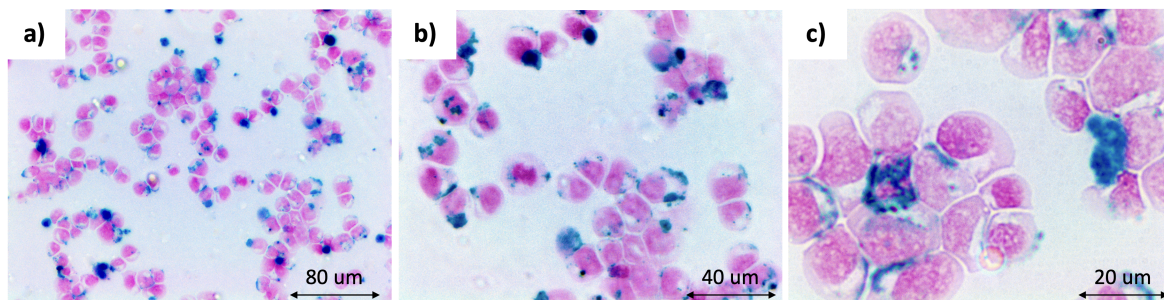


Figure 7.7: Images taken using an Olympus IX81 microscope with 10x (a), 20x (b), and 40x (c) objective lenses show cellular uptake of iron oxide nanoparticle in RAW264.7 Macrophages. Extracellular iron oxide was thoroughly washed to ensure measurement of iron content is due to the intracellular iron.

7.3.3 Labelling Cells with Iron Oxide Nanoparticles

To validate the active cancellation platform against SPIO-labelled cells, we labelled Raw 264.7 Macrophages (TIB-71, ATCC) with ferucarbotran (Vivotrax, Magnetic Insight Inc.).

7.3.3.1 Labelling Procedure

Raw264.7 macrophages (TIB-71, ATCC) were incubated with 200 ug Fe/mL ferucarbotran for 24 hours. The following day, macrophages were washed 3 times with PBS before and after trypsin dissociation to remove excess unincorporated iron. Cell pellets were created for imaging through serial dilution, ranging from 1 million to 100 cells.

7.3.3.2 Labelling Validation

Perl's Prussian blue (PPB) histology was used to visually assess labelling (Fig. 7.7). A sample of 1×10^5 labeled macrophages was used to assess iron labeling by histology (Cytospin 4, ThermoFisher). The cells were fixed by methanol acetic acid solution (3:1) and stained in Perl's Prussian blue with nuclear fast red as counterstain (ab150674, Abcam). Slides were dehydrated (75, 95, and 100% ethanol) and incubated in xylene before coverslipping. Images were taken using an Olympus IX81 microscope with 10x, 20x, and 40x objective lenses. Macrophage loading with Vivotrax was 10.34 pg/cell.

7.4 Results

We constructed a printed circuit board (Fig. 7.8) with the AD8429 and used it as the intermediate cancellation stage as illustrated in Fig. (7.8). With this active cancellation board, we validate the simulation results by sweeping the frequency and phase (Fig. 7.8).

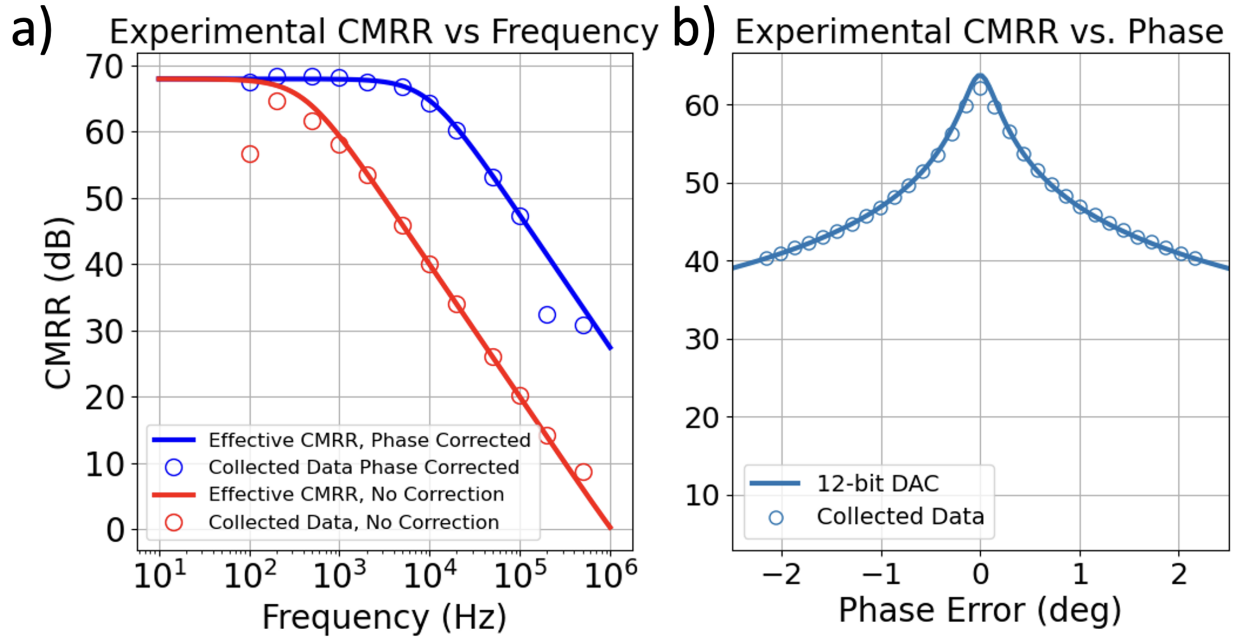


Figure 7.8: Constructed active cancellation board achieves ≥ 20 dB cancellation throughout the transmit bandwidth. We validate the simulation results against experimentally collected data. (a) There is good agreement of experimental data with simulated CMRR against frequency, with and without phase correction. (b) There is also excellent agreement of experimental data with simulated CMRR against artificially induced phase error. Artificially induced phase error was achieved by applying the same technique outlined in (7.5) with a set delay time. Full scale inputs were applied as feedthrough.

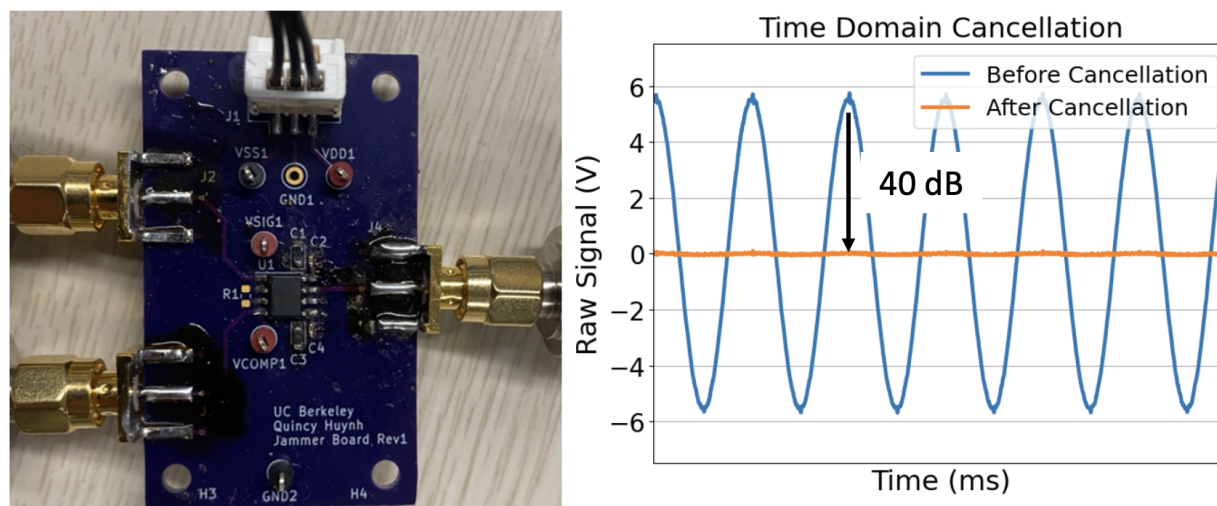


Figure 7.9: Constructed active cancellation board achieves 40 dB cancellation on the observed direct feedthrough generated by a custom-wound litz-wire transmit coil and power amplifier (AE7224, AE Techron, Elkhart, IN) from a 20 kHz 20 mT sinusoidal excitation waveform.

7.4.1 Evaluation with Commercial Nanoparticles

We evaluated the active cancellation board with a serial dilution of Ferucarbotran (VivoTrax™, Magnetic Insight Inc., Alameda, CA). First, before cancellation, we could only achieve a total receive gain of 1,000 with the use of the gradiometric cancellation coils. To enable cancellation and extra dynamic range, we added our active cancellation board and second gain stage SR560 at a gain of 10, achieving a total receive gain of 10,000, allowing us to robustly detect smaller mass samples. We calculated the point spread functions (Fig. 7.11) and the limit of detection (Fig. 7.10) to illustrate the 100-fold improvement in dynamic range with active cancellation. Note that adding extra active circuitry does add noise to the system - the AD8429 has $45 \text{ nV}/\sqrt{\text{Hz}}$ noise density, but due to it being past the first preamplifier stage with high gain, its noise contribution can be neglected.

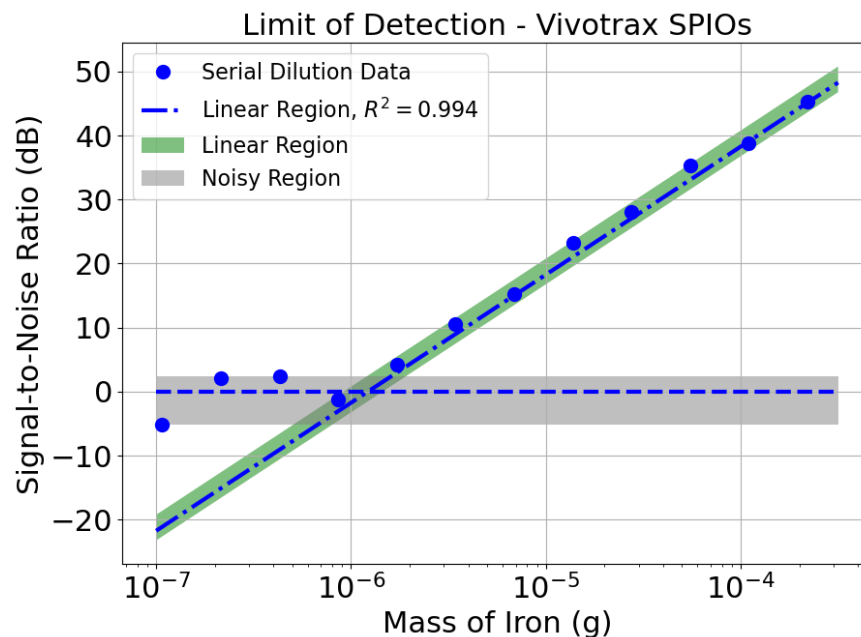


Figure 7.10: Samples of Vivotrax ($40 \mu\text{L}$, 5.5 mg/mL stock concentration) were serially diluted up to 2048x and analyzed with the AWR. The resulting limit of detection curve shows a linear dependence of the signal to mass of iron down to $1 \mu\text{g}$ for an acquisition time of 0.3 seconds (no averaging).

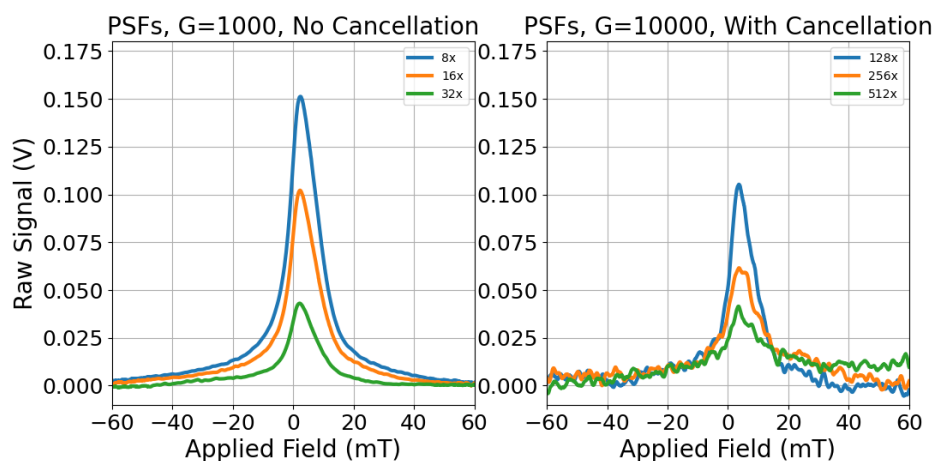


Figure 7.11: Point spread functions (PSFs) of diluted samples of Vivotrax ($40 \mu\text{L}$ of 5.5 mg/mL stock concentration). With active cancellation, we are able to detect 10-fold smaller masses of iron at the same signal level, showcasing an improved dynamic range. At lower amounts of iron, we start to see the thermal noise of the system, achieving thermal noise dominant LOD.

7.4.2 Evaluation with Labelled Cells

With the constructed active cancellation PCB, we measured the AWR signal of Vivotrax-labelled Raw264.7 macrophages at various cell counts (Fig. 7.12). The system can detect down to 10,000 cells without saturating due to direct feedthrough interference. With a broadband noise-matched preamplifier, we can expect this limit of detection to improve up to 10-fold [27]. To be clear, active feedthrough cancellation improves the ability to robustly detect the lower limit of detection - it does not improve the lower limit of detection itself without an improved low noise preamplifier.

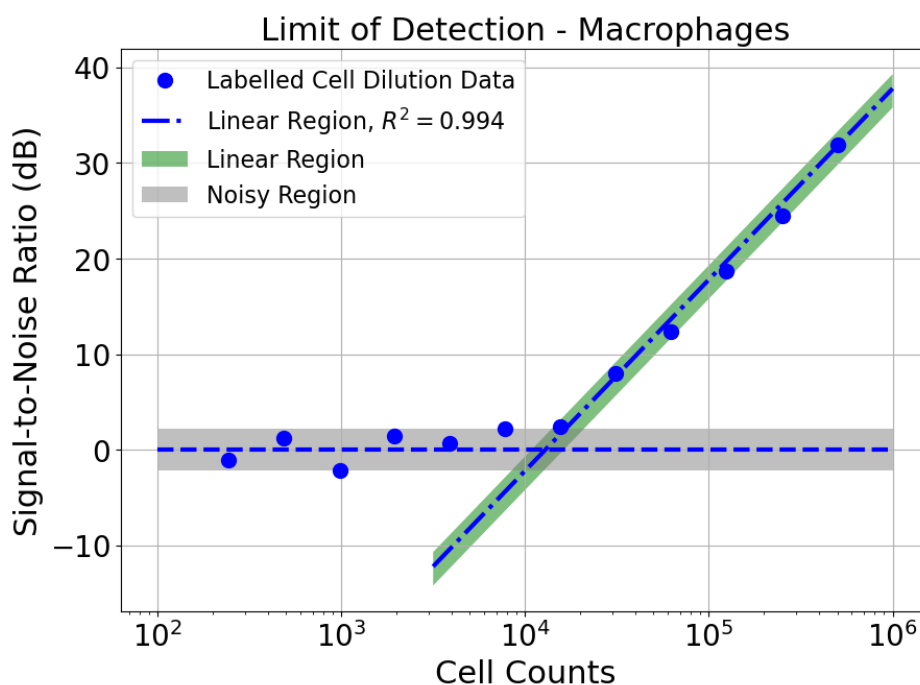


Figure 7.12: AWR signal of Vivotrax-labelled Raw264.7 macrophages were measured at various cell counts (Fig. 7.12). The system can detect down to 10,000 cells without saturating due to direct feedthrough interference for an acquisition time of 0.3 seconds (no averaging).

7.5 Conclusion

In this work, an instrumentation amplifier based active cancellation circuit was presented. This circuit enables acquisition of mass-limited magnetic particle samples down to hundreds of nanograms near full scale range. Some applications in magnetic particle sensing systems such as MPI, MPS, and MRX can benefit from this work: robust viscometry using Brownian relaxation dominant nanoparticles, and cell labelling efficiency validation of volume-limited

samples for stem cell and white blood cell tracking experiments, where sensing small amounts of iron with large dynamic range is required. This approach can also be combined with an improved low noise preamplifier to optimize the signal receive chain of magnetic particle sensing systems. Another big implication from this work is that magnetic particle sensing systems can reject feedthrough without the use of gradiometric cancellation coils or other complex coil geometries if the cancellation requirement is within the CMRR of the instrumentation amplifier used (≈ 70 dB).

7.6 Derivations

7.6.1 Effective Cancellation due to Non-idealities Derivation

There are a few non-idealities to consider when using an in-amp to cancel out a signal.

7.6.1.1 Finite Common Mode Rejection

The first is finite CMR of in-amps as mentioned before. Therefore there will always be residual common-mode in the output. CMRR is finite and frequency dependent. Consider the case where V_1 is just V_{ft} and $V_2 = V_{canc} = V_{ft}$.

$$V_{out}(t) = A_{dm}[V_{ft}(t) - V_{canc}(t)] + A_{cm}V_{ft}(t) \quad (7.6)$$

$$V_{out}(t) = A_{dm}[V_{ft}(t) - V_{ft}(t)] + A_{cm}V_{ft}(t) \quad (7.7)$$

$$V_{out}(t) = \frac{A_{dm}}{\text{CMR}}V_{ft}(t) \quad (7.8)$$

7.6.1.2 Quantization Error of the Cancellation Signal

The second is quantization error ϵ due to the DAC generating the cancellation signal V_{canc} . Quantization error is well modelled as a random uniform distribution

$$\epsilon_q(t) \in \mathcal{U}\left(-\frac{\text{LSB}}{2}, \frac{\text{LSB}}{2}\right) \quad (7.9)$$

where LSB is the least significant bit of the DAC, with a root-mean-squared (rms) voltage or standard deviation of

$$\sigma_{DAC} = \frac{\text{LSB}}{\sqrt{12}} = \frac{\text{FSR}/2^{n+1}}{\sqrt{12}} \quad (7.10)$$

where FSR is the full scale voltage range, and n is the resolution in number of bits of the DAC. The cancellation signal is now represented as $V_{canc} = V_{ft} + \epsilon_q(t)$.

$$V_{out}(t) = A_{dm}(V_{ft}(t) - V_{canc}(t)) + A_{cm}V_{ft}(t) \quad (7.11)$$

$$V_{out}(t) = A_{dm}\epsilon_q(t) + A_{cm}V_{ft}(t) \quad (7.12)$$

$$V_{out}(t) = A_{dm}\left(\frac{\epsilon_q(t)}{V_{ft}(t)} + \frac{1}{\text{CMR}}\right)V_{ft}(t) \quad (7.13)$$

Since $\epsilon_q(t)$ is a zero-mean random process, it may look like the effective common-mode rejection remains the same. However, we should be careful to note that this quantization error adds more noise to the system and degrades cancellation. Because we continuously excite the SPIOs with a periodic transmit waveform, we can generalize the feedthrough as a periodic waveform. Therefore, for a period T , we can represent (7.12) in rms

$$V_{out,rms} = \sqrt{\frac{1}{T} \int_0^T \left(A_{dm}\epsilon_q(t) + A_{cm}V_{ft}(t) \right)^2 dt} \quad (7.14)$$

$$V_{out,rms} = \sqrt{A_{dm}^2 \sigma_{DAC}^2 + A_{cm}^2 V_{ft,rms}^2} \quad (7.15)$$

$$V_{out,rms} = A_{dm} \sqrt{\frac{\sigma_{DAC}^2}{V_{ft,rms}^2} + \frac{1}{CMR^2}} V_{ft,rms} \quad (7.16)$$

(7.16) shows that quantization error creates an effective common-mode rejection CMR_{eff} of

$$CMR_{eff} = \sqrt{\frac{\sigma_{DAC}^2}{V_{ft,rms}^2} + \frac{1}{CMR^2}} \quad (7.17)$$

This quantization error creates a slight input differential signal that is amplified in the in-amp, degrading the effective common-mode rejection. The error is dependent on the DAC's least significant bit (LSB) and the relative error is dependent on the rms of the direct feedthrough $V_{ft,rms}$.

7.6.1.3 Phase Error of the Cancellation Signal

The final non-ideality is phase error between the feedthrough signal V_{ft} and the cancellation signal V_{canc} . Suppose there is some delay t_d in generating V_{canc} relative to V_{ft} due to digital timing signal differences, signal propagation path differences, and the finite time sampling of the DAC.

$$V_{out}(t) = A_{dm}(V_{ft}(t) - V_{ft}(t - t_d)) + A_{cm}V_{ft}(t) \quad (7.18)$$

Because the feedthrough is periodic, we can represent the voltages in (7.18) as analytic signals with amplitude V_{ft} and frequency ω to simplify analysis.

$$V_{ft}(t) = V_{ft} \cos(\omega t) \quad (7.19)$$

$$V_{canc}(t) = V_{ft} \cos(\omega t - \phi) \quad (7.20)$$

where $\phi = \omega t_d$ is the phase offset. The rms of the difference of the voltages is

$$V_{out,rms} = \sqrt{\int_0^T \left(V_{ft} \cos(\omega t) - V_{ft} \cos(\omega t - \phi) \right)^2 dt} \quad (7.21)$$

$$V_{out,rms} = \sqrt{1 - \cos(\phi)} \quad (7.22)$$

The phase error is dependent on the DAC's sampling rate, with a maximum resolvable error of a sampling period:

$$|\phi(\omega)_{max}| = \omega T_s = \frac{\omega}{f_s} \quad (7.23)$$

7.6.1.4 Combining all non-idealities.

Now considering phase error, quantization error, and finite CMR, we determine the effective cancellation due to all these non-idealities.

$$V_{out}(t) = A_{dm}[V_{ft} \cos(\omega t) - V_{ft} \cos(\omega t - \phi) - \epsilon_q(t)] + A_{cm} V_{ft} V_{ft} \cos(\omega t - \phi) \quad (7.24)$$

The rms voltage is then

$$\text{CMR}_{\text{eff}} = \sqrt{\frac{1}{\text{CMR}^2} + \frac{\epsilon^2}{V_{ft,rms}^2} + \frac{(2\text{CMR}^2 + 2)(1 - \cos \phi)}{\text{CMR}^2}} \quad (7.25)$$

7.6.2 Phase Error Detection and Correction Derivation

7.6.2.1 Phase Error Detection Procedure

We detect the phase error using a two-step process. For this procedure, $A_{dm} = 1$.

- First, acquire the direct feedthrough at V_1 with $V_2 = 0$.

$$V_{out,1}(t) = V_{ft}(t) \quad (7.26)$$

- Second, play back $V_{out,1}$ at V_2 with $V_1 = 0$.

$$V_{out,2}(t) = V_{ft}(t - t_d) \quad (7.27)$$

It is well known that cross-correlation can be used for time delay estimation (TDE). The cross-correlation function (CCF) of two signals $x(t)$ and $y(t)$ is defined as

$$r(t) = x(t) \star y(t) = x(t) * y(-t) \quad (7.28)$$

where \star is the convolution operator.

For a time-delayed signal $y(t) = x(t - t_d)$, $r(t)$ has a peak at $t = t_d$. This result is used to estimate the time-delay. With cross-correlation in the time domain we can only detect time delay differences of the ADC sampling period T_s . For our 10 MSPS ADC, this is 100 ns, which is not fine enough. However, performing cross-correlation in the frequency domain can lend us higher resolution. Since convolution in the time domain is multiplication in the frequency domain,

$$r(t) = x(t) * y(-t) \xleftrightarrow{\mathcal{F}} R(\omega) = X(\omega) \cdot Y^*(\omega) \quad (7.29)$$

For $y(t) = x(t - t_d)$,

$$R(\omega) = X(\omega) \cdot (X(\omega)e^{-j\omega t_d})^* \quad (7.30)$$

$$= X(\omega) \cdot X^*(\omega)e^{j\omega t_d} \quad (7.31)$$

$$= |X(\omega)|^2 e^{j\omega t_d} \quad (7.32)$$

Since $|X(\omega)|^2$ is purely real, we can determine t_d by taking the phase of $R(\omega)$.

$$t_d = \frac{\angle R(\omega)}{\omega} = \frac{X(\omega) \cdot Y^*(\omega)}{\omega} \quad (7.33)$$

However, we must threshold $X(\omega)$ and $Y(\omega)$ before taking any phase information since any small floating point errors will amplify the result of the arctangent operation used to calculate phase and create a noisy phase spectrum.

$$t_d = \frac{X_{th}(\omega) \cdot Y_{th}^*(\omega)}{\omega} \quad (7.34)$$

where $X_{th}(\omega)$ and $Y_{th}(\omega)$ are thresholded to half of the peak power of the dominant frequency component.

7.6.2.2 Phase Error Correction Procedure

Now that we have determined the phase error/time-delay offset, we correct for it. One way is to discretely shift samples in the time domain to align the signals.

$$y_{adj}(t) = y(t + nT_s) = x(t - t_d + nT_s) \quad (7.35)$$

where T_s is the sampling period of the DAC and $n = \text{round}(t_d/T_s)$. With this shifting method we can only resolve time delay differences of the DAC sampling period T_s . For our 2.5 MSPS DAC, this is 400 ns, which is not fine enough. Again, performing the time shift in the frequency domain will yield a more precise result.

$$y_{adj}(t) = y(t + t_d) \xleftrightarrow{\mathcal{F}} Y_{adj}(\omega) = Y(\omega)e^{j\omega t_d} \quad (7.36)$$

$$Y_{adj}(\omega) = Y(\omega)e^{j\omega t_d} \quad (7.37)$$

$$= (X(\omega)e^{-j\omega t_d})e^{j\omega t_d} \quad (7.38)$$

$$= X(\omega) \quad (7.39)$$

Chapter 8

Future Direction

8.1 Towards a Portable Particle Relaxometer for Non-Imaging Applications

During my PhD, I have explored advanced engineering techniques to reduce the cost of the AWR to provide an affordable and portable particle relaxometer for financially strapped researchers in academia. There are broad motivations for doing this. Reducing the cost of building a benchtop particle relaxometer provides materials scientists and chemists far greater accessibility to instruments that can analyze the magnetic properties of SPIOs — right at the bench. Our chemical colleagues must dedicate 1 day a week to drive to UC Berkeley to test an entire week’s worth of SPIOs. SPIOs also have a wide range of clinical applications outside of imaging. They can be used for temperature sensing, viscometry, reactive oxygen species detection, and binding contrast [9], [36]. Viscometry using Brownian relaxation dominant particles can be used for glucose monitoring and other clinically relevant biochemical markers [84]–[86]. For this kind of system to be clinically feasible, it must be reduced from a benchtop instrument to a portable medical device or wearable, which can only be achieved by reducing the cost and power requirements of a particle relaxometer. To achieve a table-top, portable AWR, I focused on a few strategies - innovations in coil design, RF electronics, and power amplifier design.

8.2 Transmit/Receive Coils

The sensor for a portable relaxometer should be tailored to the application. For particle analysis, microcoils would be appropriate for high SNR/volume. For clinical applications requiring subcutaneous sensing of biomarkers, a surface coil such as a spiral coil would be more appropriate. If vertical spacing is allowed, then a gradiometer designed using methods from Chapter 6 can be employed to reject feedthrough. If geometry is restricted, then an active cancellation circuit such as the one designed in Chapter 7 can be used.

8.3 Receive Frontend

The frontend can fortunately be designed using the same methodologies presented in this work and the circuitry can be built using affordable, off-the-shelf ICs from Analog Devices and other big IC manufacturers. If only square wave relaxation is needed, then a blanking switch similar to a T/R switch in MRI would be more appropriate than a combination of using both a gradiometer and active cancellation, which would only be needed for high dynamic range applications.

8.3.1 Data Acquisition Module

Choosing an affordable, lightweight DAQ for the portable relaxometer is critical. High-speed, high-resolution, and deep memory DAQs are expensive. The DAQ should also be appropriate for the application. For particle analysis exploring higher frequency excitation and detection of particles, using a NI-DAQ or something similar with > 5 MSPS and 14-bit ADC is appropriate. For applications using only square wave relaxation, the bandwidth requirement is lower and the bit-depth requirement is higher. This indicates a high-resolution, lower sampling rate DAQ as the most likely candidate. These often use a Sigma-Delta or Successive Approximation ADC.

8.4 Excitation Field Source

8.4.1 Power Amplifier Driving Coil

The transmit power supply and amp is the most expensive component of any table-top AWR system. I worked on a “cost-down” analysis of the power amplifier, which drives the excitation waveform to generate the applied magnetic field in the transmit coil. The power supply and amp can be crafted from off-the-shelf components. Power amplifier ICs (such as the Texas Instruments OPA541) provide ample power and bandwidth to excite SPIOs. At just \$25 per unit amplifier, these power opamps are nearly 300-fold more affordable than a 3-kW AE Techon 7228 linear audio power amplifier, which cost about \$7500. Paralleling them enables sufficient current driving capability to drive inductive loads.

Driving inductive coils has a few challenges. One is that the coil is typically low impedance and presents a heavy load to the power amplifier which will need to supply enough current (Figure 8.1). Another is that the frequency dependence of the coil’s impedance requires control of the current to create the desired field, since the field generated is directly proportional to the current. Hence, the amplifier should act as a voltage controlled current source. This can be achieved using negative feedback (Figure 8.2). However, the phase margin can be small in such a design, and so positive feedback oscillations must be carefully avoided.

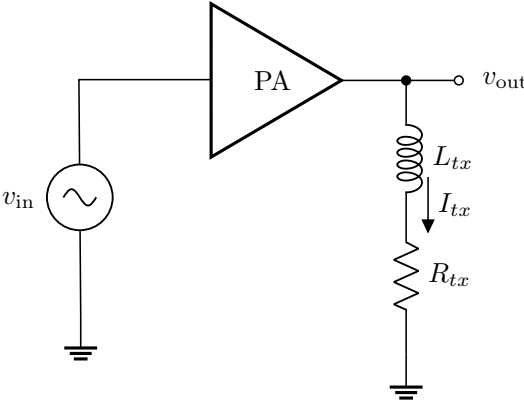


Figure 8.1: Power Amplifier driving transmit coil, which can be modelled as an inductive load with series resistance.

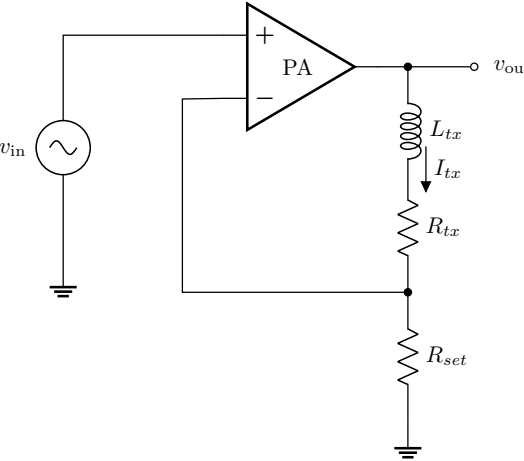


Figure 8.2: Power Amplifier driving transmit coil in feedback sets the current through the coil to be directly proportional to the input voltage, $I_{tx} = \frac{V_{in}}{R_{set}}$. Care must be taken in compensating the feedback network to prevent unwanted oscillations.

8.4.2 Mechanically Rotated Permanent Magnets

Mechanically moving permanent magnets can also generate an excitation field to saturate SPIOs with large field strengths, similar to VSM. However, the frequency of excitation is limited to the mechanically motion of the magnets.

Chapter 9

Conclusion

In this dissertation, I described the challenges in optimizing the receive frontend architecture of Magnetic Particle Imaging and other Magnetic Particle sensing systems.

In Part I, I covered the sensitivity and noise of MPI systems and demonstrate two ways to maximize signal-to-noise ratio. The first method to improve SNR is through optimal noise matching, in which I presented a design methodology for the optimal number of parallel amplifiers to improve noise factor. This resulted in an incredible 10-fold reduction in noise density while improving bandwidth 5-fold, allowing the robust detection of high resolution superferromagnetic iron oxide nanoparticles that is absolutely crucial in the clinical translation of MPI. The second method optimized the receiver coil geometry to improve sensitivity while reducing resistance and inductance that contribute to noise. From very promising simulation data, I showed that small magnetic particle relaxometers stand to quadratically gain in SNR per sample volume by reducing the radius of the receive coil, enabling higher throughput of analysis and characterization.

In Part II, I discussed the challenge of direct feedthrough interference and two ways to mitigate this interference. The first way is passive cancellation using gradiometric cancellation coils, which can be designed for easier shimmability using linear programming. This is crucial in developing mechanically robust systems where shimming the gradiometer coils is infrequent or cannot be done in the field. The second way is active cancellation using an adaptive feedforward scheme that cancels the interference using a pre-calibrated cancellation waveform. This method resulted in a 100-fold increase in dynamic range and enables a way to cancel feedthrough without the use of more complex coil geometries.

Overall these works provide a path forward in making clinical MPI possible with higher resolution and sensitivity; enable better particle relaxometers for iron oxide nanoparticle analysis and characterization for chemists and material scientists; and serve as a template for biosensing platforms that employ the clinically promising applications of SPIOs.

Bibliography

- [1] B. Gleich and J. Weizenecker, “Tomographic imaging using the nonlinear response of magnetic particles”, *Nature*, vol. 435, no. 7046, pp. 1214–1217, 2005. DOI: [10.1038/nature03808](https://doi.org/10.1038/nature03808).
- [2] E. Y. Yu, P. Chandrasekharan, R. Berzon, *et al.*, “Magnetic Particle Imaging for Highly Sensitive, Quantitative, and Safe in Vivo Gut Bleed Detection in a Murine Model”, *ACS Nano*, vol. 11, no. 12, pp. 12 067–12 076, Dec. 2017, ISSN: 1936-0851. DOI: [10.1021/acsnano.7b04844](https://doi.org/10.1021/acsnano.7b04844). [Online]. Available: <http://pubs.acs.org/doi/10.1021/acsnano.7b04844>.
- [3] X. Y. Zhou, K. E. Jeffris, E. Y. Yu, *et al.*, “First in vivo magnetic particle imaging of lung perfusion in rats”, *Physics in Medicine and Biology*, vol. 62, no. 9, pp. 3510–3522, May 2017, ISSN: 0031-9155. DOI: [10.1088/1361-6560/aa616c](https://doi.org/10.1088/1361-6560/aa616c). [Online]. Available: <https://iopscience.iop.org/article/10.1088/1361-6560/aa616c>.
- [4] P. Chandrasekharan, K. B. Fung, X. Y. Zhou, *et al.*, “Non-radioactive and sensitive tracking of neutrophils towards inflammation using antibody functionalized magnetic particle imaging tracers”, *Nanotheranostics*, vol. 5, no. 2, pp. 240–255, 2021, ISSN: 2206-7418. DOI: [10.7150/ntno.50721](https://doi.org/10.7150/ntno.50721). [Online]. Available: <https://www.ntno.org/v05p0240.htm>.
- [5] Z. W. Tay, S. Savliwala, D. W. Hensley, *et al.*, “Superferromagnetic nanoparticles enable order-of-magnitude resolution and sensitivity gain in magnetic particle imaging”, *Small Materials*, 2021.
- [6] W. F. Brown, “Thermal fluctuations of a single-domain particle”, *Physical Review*, vol. 130, pp. 1677–1686, 5 Jun. 1963, ISSN: 0031-899X. DOI: [10.1103/PhysRev.130.1677](https://doi.org/10.1103/PhysRev.130.1677).
- [7] L. Néel, “Théorie du traînage magnétique des ferromagnétiques en grains fins avec application aux terres cuites”, *Annales de géophysique*, vol. 5, pp. 99–136, 1949. [Online]. Available: <https://hal.science/hal-03070532>.
- [8] R. J. Deissler, Y. Wu, and M. A. Martens, “Dependence of brownian and néel relaxation times on magnetic field strength”, *Medical Physics*, vol. 41, p. 012 301, 1 Jan. 2014, ISSN: 0094-2405. DOI: [10.1118/1.4837216](https://doi.org/10.1118/1.4837216).

- [9] Y. Lu, A. Rivera-Rodriguez, Z. W. Tay, *et al.*, “Combining magnetic particle imaging and magnetic fluid hyperthermia for localized and image-guided treatment”, *International Journal of Hyperthermia*, vol. 37, pp. 141–154, 3 Dec. 2020, ISSN: 0265-6736. DOI: [10.1080/02656736.2020.1853252](https://doi.org/10.1080/02656736.2020.1853252).
- [10] Z. W. Tay, P. Chandrasekharan, A. Chiu-Lam, *et al.*, “Magnetic particle imaging-guided heating in vivo using gradient fields for arbitrary localization of magnetic hyperthermia therapy”, *ACS Nano*, vol. 12, pp. 3699–3713, 4 Apr. 2018, ISSN: 1936-0851. DOI: [10.1021/acsnano.8b00893](https://doi.org/10.1021/acsnano.8b00893).
- [11] H. A. Wheeler, “Simple inductance formulas for radio coils”, *Proceedings of the Institute of Radio Engineers*, vol. 16, no. 10, pp. 1398–1400, 1928. DOI: [10.1109/JRPROC.1928.221548](https://doi.org/10.1109/JRPROC.1928.221548).
- [12] H. A. Wheeler, “Formulas for the skin effect”, *Proceedings of the IRE*, vol. 30, no. 9, pp. 412–424, 1942. DOI: [10.1109/JRPROC.1942.232015](https://doi.org/10.1109/JRPROC.1942.232015).
- [13] F. E. Terman, *Radio Engineer’s Handbook*. New York, NY: McGraw-Hill, Dec. 1943.
- [14] G. Grandi, M. K. Kazimierczuk, A. Massarini, and U. Reggiani, “Stray capacitances of single-layer air-core inductors for high-frequency applications”, pp. 1384–1388, 1996. DOI: [10.1109/IAS.1996.559246](https://doi.org/10.1109/IAS.1996.559246).
- [15] D. Hault, “The principle of reciprocity in signal strength calculations—a mathematical guide”, *Concept Magn. Res.*, vol. 12, no. 4, pp. 173–187, 2000.
- [16] F. W. Sears, “Faraday’s law and ampere’s law”, *American Journal of Physics*, vol. 31, pp. 439–443, 1963.
- [17] A. Macovski, “Noise in mri”, *Magn. Reson. Med.*, vol. 36, pp. 494–497, 1996.
- [18] J. Johnson, “Thermal agitation of electricity in conductors”, *Phys. Rev.*, vol. 32, pp. 97–109, 1928.
- [19] H. T. Friis, “Noise figures of radio receivers”, *Proceedings of the IRE*, vol. 32, no. 7, pp. 419–422, 1944.
- [20] J. Rahmer, J. Weizenecker, B. Gleich, and J. Borgert, “Signal encoding in magnetic particle imaging: Properties of the system function”, *BMC Med. Imaging*, vol. 9, p. 4, Apr. 2009.
- [21] P. W. Goodwill and S. M. Conolly, “The x-space formulation of the magnetic particle imaging process: 1-d signal, resolution, bandwidth, snr, sar, and magnetostimulation”, *IEEE Transactions on Medical Imaging*, vol. 29, no. 11, pp. 1851–1859, 2010. DOI: [10.1109/TMI.2010.2052284](https://doi.org/10.1109/TMI.2010.2052284).
- [22] P. Goodwill, G. Scott, P. Stang, and S. Conolly, “Narrowband Magnetic Particle Imaging”, *IEEE Transactions on Medical Imaging*, vol. 28, no. 8, pp. 1231–1237, Aug. 2009, ISSN: 0278-0062. DOI: [10.1109/TMI.2009.2013849](https://doi.org/10.1109/TMI.2009.2013849). [Online]. Available: <http://ieeexplore.ieee.org/document/4781562/>.

- [23] P. W. Goodwill, J. J. Konkle, B. Zheng, E. U. Saritas, and S. T. Conolly, “Projection x-space magnetic particle imaging”, *IEEE Trans. Med. Imaging*, vol. 31, no. 5, pp. 1076–1085, May 2012.
- [24] E. E. Mason, C. Z. Cooley, S. F. Cauley, M. A. Griswold, S. M. Conolly, and L. L. Wald, “Design analysis of an mpi human functional brain scanner”, *Int. J. Magn. Part. imaging*, vol. 3, no. 1, 2017.
- [25] M. Graeser *et al.*, “Human-sized magnetic particle imaging for brain applications”, *Nat. Commun.*, vol. 10, no. 1, pp. 1–9, Apr. 2019.
- [26] G. Bringout and T. M. Buzug, “Coil design for magnetic particle imaging: Application for a preclinical scanner”, *IEEE Transactions on Magnetics*, vol. 51, pp. 1–8, 2 Feb. 2015, ISSN: 0018-9464. DOI: [10.1109/TMAG.2014.2344917](https://doi.org/10.1109/TMAG.2014.2344917).
- [27] B. Zheng, P. W. Goodwill, N. Dixit, *et al.*, “Optimal broadband noise matching to inductive sensors: Application to magnetic particle imaging”, *IEEE transactions on biomedical circuits and systems*, Oct. 2017. [Online]. Available: <https://www.ncbi.nlm.nih.gov/pmc/articles/PMC5741315/>.
- [28] M. Graeser, A. von Gladiss, M. Weber, and T. M. Buzug, “Two dimensional magnetic particle spectrometry”, *Physics in Medicine & Biology*, vol. 62, no. 9, 2017. DOI: [10.1088/1361-6560/aa5bcd](https://doi.org/10.1088/1361-6560/aa5bcd).
- [29] D. Pantke, N. Holle, A. Mogarkar, M. Straub, and V. Schulz, “Multifrequency magnetic particle imaging enabled by a combined passive and active drive field feed-through compensation approach”, *Medical Physics*, vol. 46, no. 9, pp. 4077–4086, 2019. DOI: <https://doi.org/10.1002/mp.13650>.
- [30] X. L. C. Wu *et al.*, “A review of magnetic particle imaging and perspectives on neuroimaging”, *AJNR Am. J. Neuroradiol.*, vol. 40, no. 2, p. 206, Feb. 2019.
- [31] B. Zheng, T. Vazin, P. W. Goodwill, *et al.*, “Magnetic particle imaging tracks the long-term fate of in vivo neural cell implants with high image contrast”, *Nature News*, Sep. 2015. [Online]. Available: <https://www.nature.com/articles/srep14055/>.
- [32] B. Zheng, M. P. von See, E. Yu, *et al.*, “Quantitative Magnetic Particle Imaging Monitors the Transplantation, Biodistribution, and Clearance of Stem Cells In Vivo”, *Theranostics*, vol. 6, no. 3, pp. 291–301, 2016, ISSN: 1838-7640. DOI: [10.7150/thno.13728](https://doi.org/10.7150/thno.13728). [Online]. Available: <http://www.thno.org/v06p0291.htm>.
- [33] E. Y. Yu, M. Bishop, B. Zheng, *et al.*, “Magnetic particle imaging: A novel in vivo imaging platform for cancer detection”, *Nano Letters*, vol. 17, pp. 1648–1654, 3 Mar. 2017, ISSN: 1530-6984. DOI: [10.1021/acs.nanolett.6b04865](https://doi.org/10.1021/acs.nanolett.6b04865). [Online]. Available: <http://pubs.acs.org/doi/abs/10.1021/acs.nanolett.6b04865>.

- [34] Z. W. Tay, P. W. Goodwill, D. W. Hensley, L. A. Taylor, B. Zheng, and S. M. Conolly, “A High-Throughput, Arbitrary-Waveform, MPI Spectrometer and Relaxometer for Comprehensive Magnetic Particle Optimization and Characterization”, *Scientific Reports*, vol. 6, no. 1, p. 34180, Dec. 2016, ISSN: 2045-2322. DOI: [10.1038/srep34180](https://doi.org/10.1038/srep34180). [Online]. Available: <http://www.nature.com/articles/srep34180>.
- [35] B. Tasdelen, E. Yagiz, M. Utkur, *et al.*, “Vector modulator based active compensation of direct feedthrough”, *International Journal on Magnetic Particle Imaging*, 2020.
- [36] T. Q. Bui, W. L. Tew, and S. I. Woods, “Ac magnetometry with active stabilization and harmonic suppression for magnetic nanoparticle spectroscopy and thermometry”, *NIST*, Jan. 2021.
- [37] Q. Huynh, B. Fung, C. Saayujya, I. Rodrigo, and S. Conolly, “Design of a more easily shimmable gradiometric coil using linear programming”, *International Journal on Magnetic Particle Imaging*, 2022.
- [38] H. Radermacher, F. Schrank, D. Pantke, F. Mueller, M. Peters, and V. Schulz, “Highly flexible gradiometer coil arrangement offering improved passive compensation for multi-frequency mpi”, *International Journal on Magnetic Particle Imaging IJMPI*, 2023. DOI: [10.18416/IJMPI.2023.2303030](https://doi.org/10.18416/IJMPI.2023.2303030). [Online]. Available: <http://dx.doi.org/10.18416/IJMPI.2023.2303030>.
- [39] O. C. Sehl and P. J. Foster, “The sensitivity of magnetic particle imaging and fluorine-19 magnetic resonance imaging for cell tracking”, *Nature News*, Nov. 2021. [Online]. Available: <https://www.nature.com/articles/s41598-021-01642-3>.
- [40] S. G. M. Y. L. H. X. M. Z. J; “Janus iron oxides @ semiconducting polymer nanoparticle tracer for cell tracking by magnetic particle imaging”, *Nano letters*, 2018. [Online]. Available: <https://pubmed.ncbi.nlm.nih.gov/29232142/>.
- [41] C. Fink, J. J. Gevaert, J. W. Barrett, J. D. Dikeakos, P. J. Foster, and G. A. Dekaban, “In vivo tracking of adenoviral-transduced iron oxide-labeled bone marrow-derived dendritic cells using magnetic particle imaging - european radiology experimental”, *SpringerOpen*, Aug. 2023. [Online]. Available: <https://eurradiolexp.springeropen.com/articles/10.1186/s41747-023-00359-4>.
- [42] S. O. A. A. PJ; “Trimodal cell tracking in vivo: Combining iron- and fluorine-based magnetic resonance imaging with magnetic particle imaging to monitor the delivery of mesenchymal stem cells and the ensuing inflammation”, *Tomography (Ann Arbor, Mich.)*, 2019. [Online]. Available: <https://pubmed.ncbi.nlm.nih.gov/31893235/>.
- [43] R.-R. A.-M. L.-L. A. N.-M. L. D.-R. CM; “Tracking adoptive t cell immunotherapy using magnetic particle imaging”, *Nanotheranostics*, 2021. [Online]. Available: <https://pubmed.ncbi.nlm.nih.gov/33972919/>.

- [44] A. Remmo, N. Löwa, O. Kosch, *et al.*, “Cell tracking by magnetic particle imaging: Methodology for labeling thp-1 monocytes with magnetic nanoparticles for cellular imaging”, *MDPI*, Sep. 2022. [Online]. Available: <https://www.mdpi.com/2073-4409/11/18/2892>.
- [45] H. Nejadnik, P. Pandit, O. Lenkov, A. P. Lahiji, K. Yerneni, and H. E. Daldrup-Link, “Ferumoxytol can be used for quantitative magnetic particle imaging of transplanted stem cells - molecular imaging and biology”, *SpringerLink*, Sep. 2018. [Online]. Available: <https://link.springer.com/article/10.1007/s11307-018-1276-x>.
- [46] V. Suryadevara, M. J. Hajipour, L. C. Adams, *et al.*, “Megapro, a clinically translatable nanoparticle for in vivo tracking of stem cell implants in pig cartilage defects”, *Theranostics*, Apr. 2023. [Online]. Available: <https://www.thno.org/v13p2710>.
- [47] O. C. Sehl, J. J. Gevaert, K. P. Melo, N. N. Knier, and P. J. Foster, “A perspective on cell tracking with magnetic particle imaging”, *Tomography*, vol. 6, no. 4, pp. 315–324, 2020. DOI: [10.18383/j.tom.2020.00043](https://doi.org/10.18383/j.tom.2020.00043).
- [48] Z. W. Tay, D. W. Hensley, E. C. Vreeland, B. Zheng, and S. M. Conolly, “The relaxation wall: experimental limits to improving MPI spatial resolution by increasing nanoparticle core size”, *Biomedical Physics & Engineering Express*, vol. 3, no. 3, p. 035 003, May 2017, ISSN: 2057-1976. DOI: [10.1088/2057-1976/aa6ab6](https://doi.org/10.1088/2057-1976/aa6ab6). [Online]. Available: <http://stacks.iop.org/2057-1976/3/i=3/a=035003?key=crossref.f7c5f5ec147f70fa39518fe4f40e104c>.
- [49] A. Van Der Ziel and E. Chenette, “Noise in Solid State Devices”, in 1978, pp. 313–383. DOI: [10.1016/S0065-2539\(08\)60414-X](https://doi.org/10.1016/S0065-2539(08)60414-X). [Online]. Available: <https://linkinghub.elsevier.com/retrieve/pii/S006525390860414X>.
- [50] KiCad, [Online]. Available: <https://www.kicad.org/>.
- [51] D. White, “The noise bandwidth of sampled data systems”, *IEEE Transactions on Instrumentation and Measurement*, vol. 38, no. 6, pp. 1036–1043, 1989. DOI: [10.1109/19.46397](https://doi.org/10.1109/19.46397).
- [52] P. W. Goodwill, K. Lu, B. Zheng, and S. M. Conolly, “An x-space magnetic particle imaging scanner”, *Review of Scientific Instruments*, vol. 83, 3 Mar. 2012, ISSN: 0034-6748. DOI: [10.1063/1.3694534](https://doi.org/10.1063/1.3694534).
- [53] A. Webb, “Radiofrequency microcoils for magnetic resonance imaging and spectroscopy”, *Journal of Magnetic Resonance*, vol. 229, pp. 55–66, Apr. 2013, ISSN: 10907807. DOI: [10.1016/j.jmr.2012.10.004](https://doi.org/10.1016/j.jmr.2012.10.004).
- [54] T. Peck, R. Magin, and P. Lauterbur, “Design and analysis of microcoils for nmr microscopy”, *Journal of Magnetic Resonance, Series B*, vol. 108, pp. 114–124, 2 Aug. 1995, ISSN: 10641866. DOI: [10.1006/jmrb.1995.1112](https://doi.org/10.1006/jmrb.1995.1112).

- [55] D. L. Olson, T. L. Peck, A. G. Webb, R. L. Magin, and J. V. Sweedler, “High-resolution microcoil 1 h-nmr for mass-limited, nanoliter-volume samples”, *Science*, vol. 270, pp. 1967–1970, 5244 Dec. 1995, ISSN: 0036-8075. DOI: [10.1126/science.270.5244.1967](https://doi.org/10.1126/science.270.5244.1967).
- [56] D. L. Olson, M. E. Lacey, and J. V. Sweedler, “High-resolution microcoil nmr for analysis of mass-limited, nanoliter samples”, *Analytical Chemistry*, vol. 70, pp. 645–650, 3 Feb. 1998, ISSN: 0003-2700. DOI: [10.1021/ac970972y](https://doi.org/10.1021/ac970972y).
- [57] F. E. Neumann, *Allgemeine Gesetze der inducirten elektrischen Ströme*, Jan. 1846. DOI: [10.1002/andp.18461430103](https://doi.org/10.1002/andp.18461430103). [Online]. Available: <https://doi.org/10.1002/andp.18461430103>.
- [58] C. B. Top, “An arbitrary waveform magnetic nanoparticle relaxometer with an asymmetrical three-section gradiometric receive coil”, *Turkish Journal of Electrical Engineering and Computer Science*, vol. 28, pp. 1344–1354, 2020, ISSN: 1300-0632. DOI: [10.3906/elk-1907-201](https://doi.org/10.3906/elk-1907-201).
- [59] A. Cagil, B. Tasdelen, and E. Saritas, “Design of a doubly tunable gradiometer coil”, *International Journal on Magnetic Particle Imaging*, vol. 6, no. 2, pp. 1–3, 2020, cited By 0. DOI: [10.18416/IJMPI.2020.2009064](https://doi.org/10.18416/IJMPI.2020.2009064). [Online]. Available: <https://www.scopus.com/inward/record.uri?eid=2-s2.0-85090183797&doi=10.18416%2fIJMPI.2020.2009064&partnerID=40&md5=9485da5ea8270c7ed5121456ce32076f>.
- [60] H. Xu, S. Conolly, G. Scott, and A. Macovski, “Homogeneous magnet design using linear programming”, *IEEE Transactions on Magnetics*, vol. 36, no. 2, pp. 476–483, 2000. DOI: [10.1109/20.825817](https://doi.org/10.1109/20.825817).
- [61] S. E. Ungersma, H. Xu, B. A. Chronik, G. C. Scott, A. Macovski, and S. M. Conolly, “Shim design using a linear programming algorithm”, *Magnetic Resonance in Medicine*, vol. 52, no. 3, pp. 619–627, 2004. DOI: <https://doi.org/10.1002/mrm.20176>. eprint: <https://onlinelibrary.wiley.com/doi/pdf/10.1002/mrm.20176>. [Online]. Available: <https://onlinelibrary.wiley.com/doi/abs/10.1002/mrm.20176>.
- [62] A. Schrijver, *Theory of linear and integer programming* (Wiley Series in Discrete Mathematics & Optimization), en. Chichester, England: John Wiley & Sons, Apr. 1998.
- [63] M. E. Rudd and J. R. Craig, “Optimum spacing of square and circular coil pairs”, *Review of Scientific Instruments*, vol. 39, pp. 1372–1374, 9 Sep. 1968, ISSN: 0034-6748. DOI: [10.1063/1.1683678](https://doi.org/10.1063/1.1683678).
- [64] Q. Huynh, O. Doyle, K. Guo, *et al.*, *Broadband untuned active cancellation and phase correction of direct feedthrough interference enables 100-fold improved magnetic particle imaging detection*, Oct. 2023. [Online]. Available: <https://doi.org/10.36227/techrxiv.24309607.v2>.

- [65] D. D. Stueber, J. Villanova, I. Aponte, Z. Xiao, and V. L. Colvin, “Magnetic nanoparticles in biology and medicine: Past, present, and future trends”, *Pharmaceutics*, vol. 13, p. 943, 7 2021, ISSN: 1999-4923. DOI: [10.3390/pharmaceutics13070943](https://doi.org/10.3390/pharmaceutics13070943). [Online]. Available: <http://dx.doi.org/10.3390/pharmaceutics13070943%20https://www.ncbi.nlm.nih.gov/pubmed/34202604%20https://www.ncbi.nlm.nih.gov/pmc/articles/PMC8309177>.
- [66] M. T. Rietberg, S. Waanders, M. M. H.-v. de Loosdrecht, R. R. Wildeboer, B. T. Haken, and L. Alic, “Modelling of dynamic behaviour in magnetic nanoparticles”, *Nanomaterials (Basel)*, vol. 11, p. 3396, 12 2021, ISSN: 2079-4991. DOI: [10.3390/nano11123396](https://doi.org/10.3390/nano11123396). [Online]. Available: <http://dx.doi.org/10.3390/nano11123396%20https://www.ncbi.nlm.nih.gov/pubmed/34947745%20https://www.ncbi.nlm.nih.gov/pmc/articles/PMC8708731>.
- [67] S. Waanders, “Differential magnetometry: Selective magnetometry for in vivo use”, Jul. 2023. DOI: [10.3990/1.9789036556934](https://doi.org/10.3990/1.9789036556934).
- [68] M. Utkur and E. U. Saritas, “Simultaneous temperature and viscosity estimation capability via magnetic nanoparticle relaxation”, *Medical Physics*, vol. 49, no. 4, pp. 2590–2601, 2022. DOI: [10.1002/mp.15509](https://doi.org/10.1002/mp.15509).
- [69] N. Garraud, R. Dhavalikar, L. Maldonado-Camargo, D. P. Arnold, and C. Rinaldi, “Design and validation of magnetic particle spectrometer for characterization of magnetic nanoparticle relaxation dynamics”, *AIP Advances*, vol. 7, no. 5, 2017. DOI: [10.1063/1.4978003](https://doi.org/10.1063/1.4978003).
- [70] A. Malhotra, A. von Gladiss, A. Behrends, *et al.*, “Tracking the growth of superparamagnetic nanoparticles with an in-situ magnetic particle spectrometer (inspect)”, *Sci Rep*, vol. 9, 2019. DOI: [10.1038/s41598-019-46882-6](https://doi.org/10.1038/s41598-019-46882-6).
- [71] A. Jaufenthaler, V. Schultze, T. Scholtes, *et al.*, “Opm magnetorelaxometry in the presence of a dc bias field”, *EPJ Quantum Technol.*, vol. 7, 1 2020, ISSN: 2196-0763. DOI: [10.1140/epjqt/s40507-020-00087-3](https://doi.org/10.1140/epjqt/s40507-020-00087-3). [Online]. Available: <http://dx.doi.org/10.1140/epjqt/s40507-020-00087-3>.
- [72] K. Wu, V. K. Chugh, A. di Girolamo, *et al.*, “A portable magnetic particle spectrometer for future rapid and wash-free bioassays”, *ACS Appl. Mater. Interfaces*, vol. 13, pp. 7966–7976, 7 2021, ISSN: 1944-8244. DOI: [10.1021/acsami.0c21040](https://doi.org/10.1021/acsami.0c21040). [Online]. Available: <http://dx.doi.org/10.1021/acsami.0c21040%20https://www.ncbi.nlm.nih.gov/pubmed/33566573%20https://www.ncbi.nlm.nih.gov/pmc/articles/PMC9053107>.
- [73] P. Vogel, M. A. Rückert, B. Friedrich, *et al.*, “Critical offset magnetic particle spectroscopy for rapid and highly sensitive medical point-of-care diagnostics”, *Nature Communications*, vol. 13, p. 7230, 1 Nov. 2022, ISSN: 2041-1723. DOI: [10.1038/s41467-022-34941-y](https://doi.org/10.1038/s41467-022-34941-y).

- [74] D. Jyoti, S. W. Gordon-Wylie, D. B. Reeves, K. D. Paulsen, and J. B. Weaver, “Distinguishing nanoparticle aggregation from viscosity changes in mps/msb detection of biomarkers”, *Sensors (Basel)*, vol. 22, p. 6690, 17 2022, ISSN: 1424-8220. DOI: [10.3390/s22176690](https://doi.org/10.3390/s22176690). [Online]. Available: <http://dx.doi.org/10.3390/s22176690%20https://www.ncbi.nlm.nih.gov/pubmed/36081147%20https://www.ncbi.nlm.nih.gov/pmc/articles/PMC9459920>.
- [75] P. Yari, B. Rezaei, C. Dey, *et al.*, “Magnetic particle spectroscopy for point-of-care: A review on recent advances”, *Sensors (Basel)*, vol. 23, 9 2023, ISSN: 1424-8220. DOI: [10.3390/s23094411](https://doi.org/10.3390/s23094411). [Online]. Available: <http://dx.doi.org/10.3390/s23094411%20https://www.ncbi.nlm.nih.gov/pubmed/37177614%20https://www.ncbi.nlm.nih.gov/pmc/articles/PMC10181768>.
- [76] M. Irfan, N. Dogan, T. Sapmaz, and A. Bingolbali, “Development of mpi relaxometer for characterization of superparamagnetic nanoparticles”, *Journal of Magnetism and Magnetic Materials*, vol. 536, 2021. DOI: [10.1016/j.jmmm.2021.168082](https://doi.org/10.1016/j.jmmm.2021.168082).
- [77] P. W. Goodwill, A. Tamrazian, L. R. Croft, *et al.*, “Ferrohydrodynamic relaxometry for magnetic particle imaging”, *Applied Physics Letters*, vol. 98, 26 Jun. 2011, ISSN: 0003-6951. DOI: [10.1063/1.3604009](https://doi.org/10.1063/1.3604009).
- [78] L. R. Croft, P. W. Goodwill, and S. M. Conolly, “Relaxation in X-Space Magnetic Particle Imaging”, *IEEE Transactions on Medical Imaging*, vol. 31, no. 12, pp. 2335–2342, Dec. 2012. DOI: [10.1109/TMI.2012.2217979](https://doi.org/10.1109/TMI.2012.2217979). arXiv: [NIHMS150003](https://arxiv.org/abs/150003). [Online]. Available: <http://ieeexplore.ieee.org/document/6297476/>.
- [79] M. M. van de Loosdrecht, S. Draack, S. Waanders, *et al.*, “A novel characterization technique for superparamagnetic iron oxide nanoparticles: The superparamagnetic quantifier, compared with magnetic particle spectroscopy”, *Rev. Sci. Instrum.*, vol. 90, p. 024 101, 2 2019, ISSN: 0034-6748. DOI: [10.1063/1.5039150](https://doi.org/10.1063/1.5039150). [Online]. Available: <http://dx.doi.org/10.1063/1.5039150%20https://www.ncbi.nlm.nih.gov/pubmed/30831678>.
- [80] X. Chen, M. Graeser, A. Behrends, A. von Gladiss, and T. M. Buzug, “First measurement and snr results of a 3d magnetic particle spectrometer”, *International Journal on Magnetic Particle Imaging*, vol. 4, no. 1, 2018. DOI: [10.18416/IJMPI.2018.1810001](https://doi.org/10.18416/IJMPI.2018.1810001).
- [81] S. Biederer, T. Knopp, T. F. Sattel, *et al.*, “Magnetic response spectroscopy of superparamagnetic nanoparticles for magnetic particle imaging”, *Journal of Physics D: Applied Physics*, vol. 42, 2009. DOI: [10.1088/0022-3727/42/20/205007](https://doi.org/10.1088/0022-3727/42/20/205007).
- [82] T. Wawrzik, F. Ludwig, and M. Schilling, “Multivariate magnetic particle spectroscopy for magnetic nanoparticle characterization”, in *Magnetic Nanoparticles: Particle Science, Imaging Technology, and Clinical Applications*, 2010, pp. 86–91. DOI: [10.1063/1.3530024](https://doi.org/10.1063/1.3530024).

- [83] T. Wawrzik, F. Ludwig, and M. Schilling, “Perspectives of magnetic particle spectroscopy for magnetic nanoparticle characterization”, in *Magnetic Particle Imaging: A Novel SPIO Nanoparticle Imaging Technique*, vol. 140, 2012, pp. 41–45. DOI: [10.1007/978-3-642-24133-8_7](https://doi.org/10.1007/978-3-642-24133-8_7).
- [84] M. Utkur, Y. Muslu, and E. U. Saritas, “Relaxation-based viscosity mapping for magnetic particle imaging”, *Physics in Medicine and Biology*, vol. 62, pp. 3422–3439, 9 May 2017, ISSN: 0031-9155. DOI: [10.1088/1361-6560/62/9/3422](https://doi.org/10.1088/1361-6560/62/9/3422).
- [85] M. Mushtaq, M. A. Mateen, and U.-H. Kim, “Hyperglycemia associated blood viscosity can be a nexus stimuli”, *Clinical Hemorheology and Microcirculation*, vol. 71, pp. 103–112, 1 Feb. 2019, ISSN: 13860291. DOI: [10.3233/CH-180426](https://doi.org/10.3233/CH-180426).
- [86] Y. Çinar, “Blood viscosity and blood pressure: Role of temperature and hyperglycemia”, *American Journal of Hypertension*, vol. 14, pp. 433–438, 5 May 2001, ISSN: 08957061. DOI: [10.1016/S0895-7061\(00\)01260-7](https://doi.org/10.1016/S0895-7061(00)01260-7).